Master's thesis

2019

Celine Ness Wiehe

**NTNU**
Norwegian University of
Science and Technology
Faculty of Engineering
Department of Marine Technology

Master's thesis

Celine Ness Wiehe

# Ice Loading on Ship Hulls

## Accidental Impacts with Bergy Bits

July 2019

NTNU
Norwegian University of
Science and Technology

NTNU
Norwegian University of
Science and Technology

NTNU

Norwegian University of
Science and Technology

# Ice Loading on Ship Hulls

Accidental Impacts with Bergy Bits

Celine Ness Wiehe

Marine Technology
Submission date: July 2019
Supervisor: Bernt Johan Leira

Norwegian University of Science and Technology
Department of Marine Technology

# Abstract

The increased melting of the ice in the Arctic makes shipping routes through the polar region more accessible. These routes can be shorter than the main routes used today. Ice will still be an obstacle in the polar regions and ships must meet requirements set by regulations and standards. Bergy bits and growlers are smaller glacial ice features that are difficult to detect and accidental impacts between ships and these ice features can therefore be difficult to avoid. The loads these ice features can exert on a ship and the damage they can cause are important to understand. Increased activity in the Arctic is expected and more ice related impacts will happen as a consequence.

Ice is a complex material and experiments on its mechanical properties show scattered results. During crushing, the pressure from the ice on the structure will consist of pressures from intact ice and crushed ice being expelled from the contact region. These pressures are often simplified for analyses and in the regulations. Numerical models have been proposed for more realistic impact simulations.

Two stiffened plate models of different strengths were created. The stiffened plate was assumed part of the bow of a ship. The stronger plate was dimensioned based on classification PC 7 of the International Association of Classification Societies. The weak plate could not support the static design ice load and showed large rotations of the stiffener webs before failure. The strong plate showed some small plastic strains for the same load. Two different static bergy bit loads were also applied to the plates. One of the bergy bit loads showed large displacement and concerning strains for the weak plate. The stronger plate had relatively small displacements and strains for the bergy bit loads. These results indicate that the requirements for PC 7 classification may be sufficient for resisting the bergy bit loads. However, bergy bit loads can be larger than the ones taken from the impact trial and are dependent on mass and sea state.

An impact between the strong plate and a bergy bit was attempted using ANSYS Explicit Dynamics. Problems in modelling the ice feature as a crushable foam resulted in inconclusive results. The response of the plate was similar in magnitude to that of the larger bergy bit static load. No critical failure of the plate was

detected.

# Sammendrag

Isen i Arktis smelter i økende grad og dette gir tilgang til skipsleder gjennom polområdene. Disse skipsledene kan være kortere enn hovedledene som brukes i dag. Isen er til hindring i polområdene og skip må møte krav til standarder og regelverk. "Bergy bits" og "growlers" er mindre ismasser fra isfjell og isbreer. Disse er vanskelige å oppdage og utilsiktede kollisjoner med disse ismassen kan være vanskelig å unngå. Det er viktig å forstå lastene og skadene disse ismassene kan påføre skip. Det er forventet økt aktivitet i Arktis og en følge av dette vil være flere isrelaterte kollisjoner.

Is er et komplekst materiale og forsøk viser store variasjoner på isens mekaniske egenskaper. Under knusing vil trykket fra isen bestå av trykk fra intakt is og trykk fra knust is som blir presset ut fra kontaktområdet. Disse trykkene er ofte forenklet i analyser og regelverk. Det har blitt foreslått numeriske modeller av is som kan brukes i mer realistiske kollisjonssimuleringer.

To avstivede plater ble modellert med forskjellig styrke. Den avstivede platen er en del av baugen på et skip. Den sterke platen ble dimensjonert basert på klassifikasjonen PC 7 til International Association of Classification Societies. Den svake platen tålte ikke den statiske designlasten av is og hadde store rotasjoner i stiversteget før den sviktet. Den sterke platen hadde noe plastiske tøyninger under den samme lasten. Platene ble også påført to forskjellige statiske "bergy bit" laster. En av disse lastene ga store deformasjoner og tøyninger av den svake platen. Den sterke platen hadde relative små deformasjoner og tøyninger under "bergy bit" lastene. Disse reultatene kan indikere at kravene satt for klassifikasjon PC 7 er tilstrekkelige for å motstå "bergy bit" lastene, men det må også nevnes at "bergy bit" laster kan være større enn de hentet fra et eksperiment og avhenger av vekt og sjøtilstand.

Det ble forsøkt å simulere en kollisjon mellom den sterke platen og en "bergy bit" i programmet ANSYS Explicit Dynamics. Problemer i modelleringen av ismassen førte til uklare resultater. Platens respons liknet på resultatene fra den statiske lasten fra den store "bergy bit". Platen hadde ikke kritisk svikt.

# Preface

This report is a Master Thesis in the field of marine structural engineering. The thesis was written during the spring semester of 2019 at the Department of Marine Technology under the Norwegian University of Science and Technology.

Theory from several courses taken as a student have been used in this thesis and it has been interesting to learn about ice loads as this was a new field for me last autumn. The subject has been a self study for the most part and the curriculum of a course by Professor Knut Vilhelm Høyland has been of great help. The programming and modelling in ANSYS was time consuming. A great deal has been learnt about using the ANSYS GUI and ANSYS Explicit Dynamics through this work.

I would like to thank my supervisor, Professor Bernt Johan Leira, who have guided and supported me through this thesis. He has provided relevant literature and encouraging feedback.

Celine Ness Wiehe

Celine Ness Wiehe
Trondheim, July 25th 2019

# Contents

# List of Figures

# List of Tables

# Abbreviations

| | |
|---|---|
| FSICR | Finnish-Swedish Ice Class Rules |
| HPZ | High pressure zone |
| IACS | International Association of Classification Societies |
| IMO | International Maritime Organization |
| ISO | International Organization for Standardization |
| LPZ | Low pressure zone |
| NSR | Northern Sea Route |
| ULS | Ultimate Limit State |
| WMO | World Meteorological Organization |

# Chapter 1

# Introduction

The ice in the Arctic is melting and this opens up to more commercial traffic through the polar region. The arctic routes can be shorter than the routes mainly used today for commercial shipping. The Northeast Passage is a shipping route connecting the Atlantic and the Pacific ocean north of Norway and Russia. This route can be significantly shorter than the route through the Suez canal when travelling between Asia and Europe.

The arctic sea routes are shorter, but the arctic environment cause higher risk to shipping and operations. Cold weather, ice and limited search and rescue capabilities are some of the main factors limiting operations in the Arctic. The Northern Sea Route, which is part of the Northeast Passage, is available for traffic for about three months of the year depending on ice coverage.

Ships operating in the polar regions must be designed to withstand ice loads and are required to follow certain design regulations. Larger ice floes and icebergs can be tracked and are often avoided. Smaller pieces of ice may however cause accidental impacts. They can be difficult to detect, especially in rough weather. These ice features originate from larger features of arctic sea ice or icebergs breaking up. Impacts with smaller ice features can be difficult to avoid when travelling in the Arctic and therefore the vessel speed should possibly be lowered. This could lead to the travel time of the Arctic routes being longer even though the routes are shorter.

Glaciers in the polar regions are melting at an increased rate due to climate change. This may lead to more icebergs, and combined with increased operations in the Arctic, the probability of impacts between structures and glacial ice features increases. The consequences of such impacts could be serious and should be understood.

Ice is a complex material and failure of ice has been studied with considerable scattered results. Several methods have been proposed for numerical modelling of

ice that can be used to determine accidental impacts with ice features. A single finite method used to determine these loads has not been agreed upon.

## 1.1 Objective and Outline of Thesis

The main objective of this thesis is to analyse local structural response from accidental impacts between ships and smaller glacial ice features such as growlers and bergy bits. The following chapters have been included in this thesis.

- Chapter 1 - Introduction.
- Chapter 2 - Background Theory. Relevant theory regarding steel material, ice and interaction between structure and ice is presented.
- Chapter 3 - Numerical Ice Models. Some numerical ice models used in structure-ice interactions are presented.
- Chapter 4 - Regulations. Minimum requirements for ships operating in the Arctic is presented.
- Chapter 5 - Finite Element Method. An overview of the finite element method is presented. The chapter includes nonlinear effects and solution techniques for static and dynamic loading.
- Chapter 6 - Previous Work. A full scale bergy bit impact trial and a model experiment compared to numerical simulation is presented.
- Chapter 7 - Modelling Ship-Ice Impact. The method used in a static and a dynamic simulation of bergy bit impacts are presented.
- Chapter 8 - Results of Static Loading. The results from the static analyses are presented.
- Chapter 9 - Results of Dynamic Loading. The results from an integrated simulation of ship-ice impact are presented.
- Chapter 10 - Discussion. The results from both the static and the dynamic simulations are discussed
- Chapter 11 - Conclusion.
- Chapter 12 - Further Work. Recommended further work is presented.

## 1.2 Limitations

The focus of the thesis is accidental impacts between ships and smaller features of glacier ice. The presented theory is limited to what was deemed important for understanding the simulated impacts. There are several standards and regulations

regarding ice interaction. The requirements set by the International Association of Classification Societies for classification PC 7 gives the minimum requirements for ships operating in the Arctic and is therefore the focus of this section. Only impacts in the bow region were assessed. Global loads from ice are not discussed in this thesis.

# Chapter 2

# Background Theory

## 2.1 Material Properties of Steel

The material behaviour is important when assessing structural strength. Some of the important material properties for a collision are the stress-strain relationship, strain-rate effects, and the strain-state dependence of fracture.

### 2.1.1 Material strength and quality

Steel materials are classified into strength groups and material quality. The yield stress defines the strength group and the choice of material strength is based on the cost and weight. In general, the price of steel increases for increased yield stress. Using higher strength steels will reduce the structural weight. This is beneficial as it increases the loading capacity and can increase the stability. IACS has four main strength groups with minimum requirements to yield strength. Normal strength steels has a minimum yield strength of 235 MPa. For the higher strength steel groups this value is 315 MPa, 355 MPa and 390 MPa. (IACS, 2018)

The material quality sets requirements to some material properties. The properties depends on the chemical composition of the material and the manufacturing process. An important factor of the material quality is the material resistance against brittle fracture. (Leira, 2014) A material has a lower likelihood of brittle fracture when it has a long critical crack length. Materials with long critical crack lengths are considered as of higher quality.

The material quality must be selected based on material class and plate thickness. Material classes are assigned to different structural components by regulations. Failure of different components and regions can have different consequences. A crack in the deck may not be as severe as a crack in the hull below the waterline. It

is also important to prevent crack propagation. High quality material are applied to sections where the consequences of failure are large. Ductile fractures are more controlled and can be detected. Brittle fractures can be dangerous. A crack in the hull of a ship could mean that water would pour in and this could be catastrophic. The likelihood of brittle failure increase as the thickness increase. Therefore, the required material quality increases for increased thickness.

The danger of brittle fracture increases for low temperatures, rapid change of stress level and three-dimensional stress conditions. All of which are part of an impact in the Arctic. Standards can require the steel to avoid brittle failure modes, meaning that the material should operate in the ductile regime. The ductile to brittle transition temperature should be below the design temperature. The majority of steel used in ship and offshore construction is mild steel. Mild steel is prone to brittle failure in low temperatures. (Bridges et al., 2018) The steel grades are described by Charpy testing at different temperatures. The test temperature does not necessarily reflect the ductile to brittle transition temperature or the minimum operating temperature.

### 2.1.2 Plastic behaviour

Steel materials are linear elastic for low stresses and strains. The stresses and strains are linearly dependent. A load will cause a small deflection to the structure, but the structure will displace back to its original form when the load is removed. The material is elastic if it follows the same curve for loading and unloading.

For larger stresses and strains, the material will have a non-linear and plastic behaviour. The material will have a linear behaviour up the proportionality limit, $\sigma_p$, and will have plastic deformations for stresses above the yield stress, $\sigma_y$. Plastic deformations means that the structure will not displace back to its original from when the load is removed. When the stress starts to decrease, the strain will decrease linearly as shown by the dashed line in Figure 2.1. This dashed line is parallel to the initial linear stress-strain relationship, and a plastic strain will be left even though there is no stress in the structure.

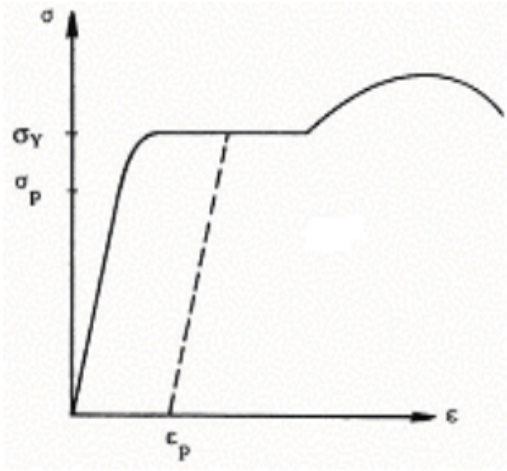


Figure 2.1: Nonlinear stress-strain curve for mild steel in a uniaxial tension test. (Moan, 2003)

When the stress reach the yield stress there is a yield plateau without significant hardening. Then plastic hardening occurs. The structure is capable of taking higher stresses until it reaches the ultimate stress and the strength decreases.

High strength steels have higher yield stresses. The ratio of the fracture stress to the yield stress is lower for higher yield stresses. This means that the remaining strength after yield is less for higher strength materials than for normal strength materials.

A material already exposed to plastic flow will have a changed yield criterion. A hardening rule describes how the yield condition is modified due to strain hardening. The choice of hardening rule is important for models with cyclic and reversed loading. If the structure is unloaded as shown in Figure 2.1, and then reloaded, the stress-strain curve will follow the dashed line until yield when it reaches the original stress-strain curve in black. Then the material will follow the original stress-strain curve until failure. If the structure had been reloaded in the opposite direction, the stress-strain curve would change as illustrated in Figure 2.2. If the new yield point is at $|\sigma| = \sigma_B$, the hardening is isotropic. It has been observed for common metals that the yield point is lower for reversed loading. The total elastic range of $2\sigma_Y$ is preserved in the unloading. This is called the kinematic hardening rule.

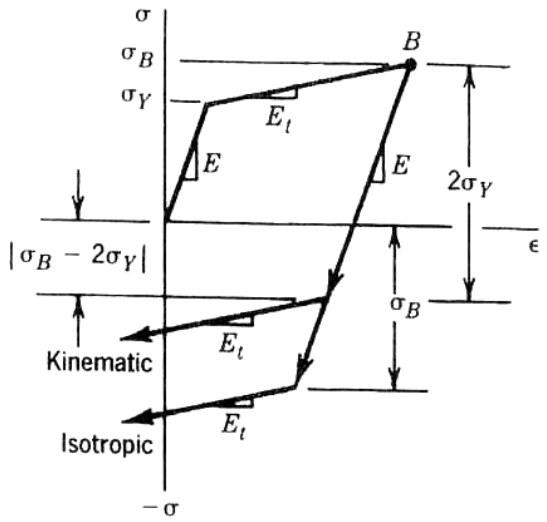


Figure 2.2: Kinematic and isotropic hardening rules. (Moan, 2003)

The modified yield surface for two-dimensional stress is shown in Figure 2.3.

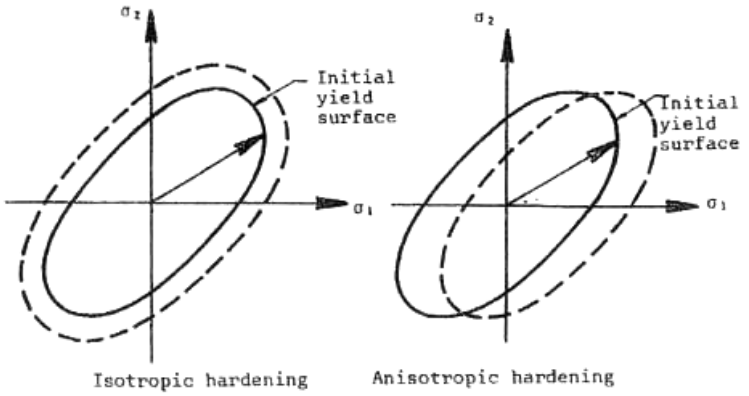


Figure 2.3: Yield surface for isotropic and anisotropic hardening rules for two dimensional model. (Moan, 2003)

The tangent modulus $E_t$ is constant in Figure 2.2. This is an idealisation. A flow rule describes the relation between stress increments $d\sigma$ and strain increments $d\varepsilon$. This relationship does not need to be linear.

### 2.1.3 Calculating stresses and strains

The von Mises stress or equivalent stress is calculated based on the principal stresses as seen in equation 2.1. A three dimensional stress state can be represented as a single positive stress value using the von Mises stress.

$$\sigma_e = \left[\frac{(\sigma_1 - \sigma_2)^2 + (\sigma_2 - \sigma_3)^2 + (\sigma_3 - \sigma_1)^2}{2}\right]^{1/2} \tag{2.1}$$

The von Mises or equivalent strain is calculated using equation 2.2.

$$\varepsilon_e = \frac{1}{1+\nu'}\left(\frac{1}{2}\left[(\varepsilon_1 - \varepsilon_2)^2 + (\varepsilon_2 - \varepsilon_3)^2 + (\varepsilon_3 - \varepsilon_2)^2\right]\right)^{1/2} \tag{2.2}$$

$\nu'$ is the effective Poisson's ratio. It is set to the defined material Poisson's ratio for elastic strains and equals 0.5 for plastic strains in ANSYS. (ANSYS, 2019a) The equivalent plastic strain gives a measure of the amount of permanent strain in the body. The equivalent total strain is the sum of elastic and plastic strain.

## 2.2 Properties of Ice

### 2.2.1 Definitions

The World Meteorological Organization has set a standard defining different properties and classifications of sea ice. (WMO, 2014) Glacier ice is of land origin. It comes from a glacier and can be on land or floating on the sea as icebergs, bergy bits or growlers. A bergy bit is floating glacier ice that is showing between 1 m and 5 m above sea-level. It has an area between 100 and 300 $m^2$. Growlers are smaller than bergy bits and floats less than 1 m above the sea surface. In normally has an area of about 20 $m^2$. Growlers can be difficult to detect especially when it is surrounded by sea ice or in high sea states.

### 2.2.2 Mechanical Properties

The presence of ice is a hindering factor when operating in the Arctic and other ice covered areas. To understand the limitations of an operation it is essential to understand the sea ice. The physical and mechanical properties of sea ice determines the ice loads a ship or offshore structure may encounter in these regions. To better understand these loads, the physical and mechanical properties must be understood. There have been several test conducted on ice, but mostly on first-year ice. The properties of old sea ice is important, especially when considering operations in the Arctic. Old sea ice cause the highest ice loads and the most damage to vessels and offshore structures. Measurements of old sea ice are however costly

and more difficult to obtain. An important difference between sea ice and glacier ice is that the sea ice has a salinity that will affect many of its properties. The salt will be expelled from the ice over time. The properties of old sea ice is closer to the properties of glacial ice. A presentation of sea ice properties can be found in the review paper by Timco and Weeks (2010). Some of the properties presented are generally well understood while others are not. Ice is formed under natural conditions and will have different properties to ice formed in the lab. Natural ice has many pores, flaws, cracks and weaknesses. It is affected by stresses caused by thermal changes, waves and other environmental forces during its formation and after. Icebergs are also changing over time. The environmental forces acting on them cause them to calve, roll and break up. (Jordaan, 2001)

## 2.3 Structure-Ice Interaction

There are three different scenarios that can occur when an ice feature and a structure collide. The first scenario is that the ice fails. The second is that the structure fails, and the third that the structure or ice moves. Failure of ice and the loads the ice may exert on a structure is described in the following sections.

### 2.3.1 Ice Failure Modes

An interaction between an ice feature and a structure give rise to ice forces. There are three defined limiting mechanisms for ice forces. Each of the three mechanisms gives one limiting load. The mechanism giving the lowest limiting load will control how the ice fails and what load the structure will be subjected to. (Frederking and Shkhinek, 2014)

The limit energy is one of these mechanisms. The ice feature is then assumed to fail against the structure and come to a complete stop. It is the momentum or kinetic energy of the ice feature that decides the outcome. This limiting mechanism is most common for ice features of small fetch.

The limit force is found when the ice fails a distance from the structure. The driving forces from winds, currents and surrounding pack ice makes the ice fail in a ridging event.

The mechanism that generally results in the highest ice force is the limit stress. The ice will then fail at the contact points with the structure. The way the ice fails can be described by the failure mode. The failure mode depends on the structure type and shape, the ice velocity, thickness, temperature and strength. The magnitude of the ice force is related to the failure mode.

Some failure modes for an ice floe moving towards a fixed structure with vertical sides can be seen in Figure 2.4. When the velocity of the ice feature is slow, it may deform in creep as seen Figure 2.4a. The ice deforms at low strain rates, typically $10^{-5}$ or lower. The ice then has little or no micro-cracking and no large fractures. If the ice sheet has a small thickness, it may buckle as in Figure 2.4b. Buckling occurs more readily if the ice sheet also is exposed to some other load. The ice sheet may fail in bending and fracture after buckling has occurred. Another failure mode is splitting. Then tensile components of the stress state at the contact region causes vertical macro-fractures. Spalling is seen in Figure 2.4e. Here planar cracks runs from the interface between the structure and the ice feature out to a free surface. The crack may propagate to the top or the bottom of the ice cover. This process can remove large parts of the contact area between the structure and the ice. This will result in a drop in the ice force. The failure modes crushing and bending are described below.

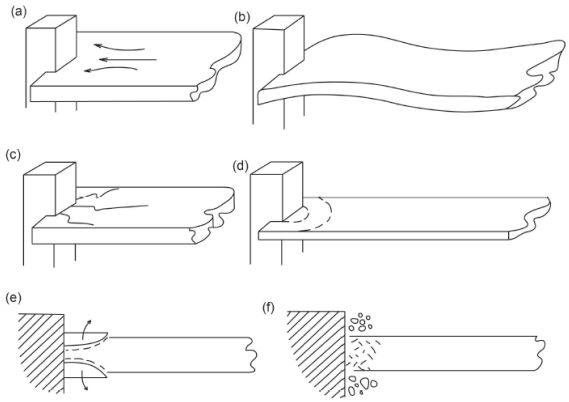


Figure 2.4: Failure modes of ice in contact with vertical structures. a) creep, b) buckling, c) radial cracking, d) circumferential cracking, e) spalling and f) crushing. (Høyland, n.d.)

The geometry of the structure affects the interaction scenario. If the structure is narrow, the surrounding ice will confine the ice and create a three dimensional stress state in front of the structure. (Frederking and Shkhinek, 2014) This will result in high pressures. Bending and buckling modes are more common for wider structures. The effective ice pressure will be lower. If a vertical structure is wide, ice may pile up in front of it, while it will move more easily around narrow structures. Using multiple legs on a structure can reduce the area exposed to ice loading. However, if multiple legs are in close proximity to each other, ice may freeze and jam between the legs and thus increase the area exposed to ice loading.

The pressure-area relationship for ice loads on a structure will depend on the size of the structure. Structures with larger contact areas is exposed to higher nominal

pressure than structures with smaller contact areas. Ice is not a homogeneous material and the chance of weak region of the ice failing increases with contact area. Boundary conditions are also of import to the failure mode.

The outcome of an interaction event depends on many parameters and require considerable knowledge of ice properties, ice conditions and environmental factors.

### 2.3.2 Crushing of Ice

Crushing is usually assumed for vertical sided structures during design. The compressive interaction between a structure and an ice feature can be seen in Figure 2.5a. The compressive forces from the structure are transmitted to the ice through the nominal interaction area. The pressures within these areas fluctuate in space and time. Jordaan (2001) defines three areas of pressure that can be seen in Figure 2.5b. The spalled area, where the pressure is zero for edge spalls, is shown in white. The area where crushed ice is extruded has a moderate pressure and is shown in shaded grey. The areas of high pressure zones are shown as dark grey/black areas.

Most of the force is concentrated and transmitted through the high pressure zones. The centre of the high pressure zones has higher pressures than near the edges of the high pressure zones. The number and position of the high pressure zones are constantly changing. The high pressure zones are usually located in the most confined regions. The stress is triaxial in these zones and there are regions of intense shear stresses. These forces results in microstructural changes. Both microfracturing and recrystallisation can occur during the impact. Spalling of the ice occurs during compressive forces, and pieces of ice break off. New spalls are formed frequently near the high pressure zones. Fractures comes from weaknesses in the ice combined with stress conditions. The failure process of ice in compression is rather complex.

Ice indentation and fracture are time-dependent effect and are affected by the interaction velocity. The total force from the ice is however not clearly dependent on the interaction velocity except for very low interaction speeds. A high loading rate causes a much higher stress concentration near the high pressure zones. This increases the likelihood of spalling.

The average pressure decreases as the contact area increase. The maximum force an ice feature will produce has a high degree of randomness connected to it. If the ice feature has fewer flaws than average, it can exert larger loads on a structure.

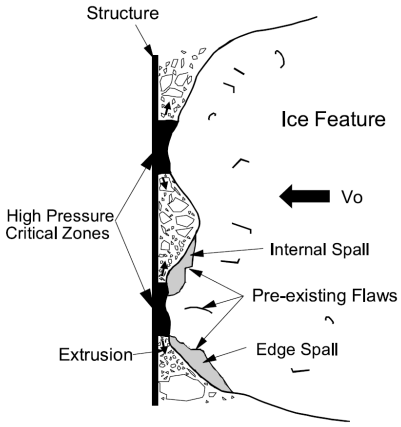


(a) Compressive interaction between a structure and an ice feature. The areas within the nominal interaction area can be seen from the side.

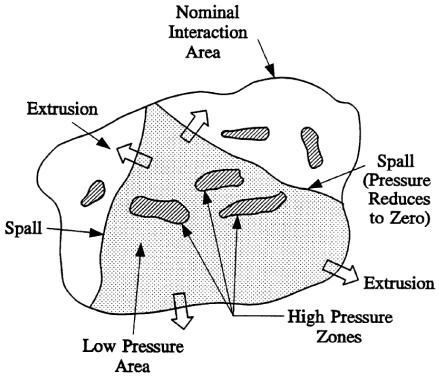


(b) The areas within the nominal interaction area. Spalled area at the edges are white, the low pressure zone in light grey and the high pressure zones in dark grey.

Figure 2.5: Compressive interaction between a structure and an ice feature, showing different defined areas depending on ice structure and pressure exerted on structure. (Jordaan, 2001)

### 2.3.3 Bending of Ice

It generally takes less energy for ice to fail in bending rather than crushing. (Frederking and Shkhinek, 2014) Sloping structures usually cause out of plane deformations on the ice sheet. This eventually produces bending, or flexural, failure. The breaking length depends on the ice thickness and may be a few times the ice thickness. The method for calculating ice forces on a sloping structure can be found in ISO (2010).

For higher incoming ice velocities, the sloping structure will experience higher loads. The broken off ice piece is exposed to friction drag, rotational inertia forces and hydrodynamic forces from the added mass. The forces acts on the piece of ice and forces it to shrink. This may result in the piece of ice failing by shear, inducing higher loads. (Frederking and Shkhinek, 2014) The ice thickness, structure width, slope angle and surface roughness all influence the effect increasing velocity will have on the resulting loads. For high velocities the ice may fail in crushing rather than bending. (Høyland, n.d.)

Sloping structures can be offshore installations, bridge columns or quays. A disadvantage of building a sloping structure is that the waterline area is larger which will lead to higher wave forces. Sloping structures can also be more difficult and expensive to build as well as difficult to access by ship. Ice may also accumulate

as rubble as shown in Figure 2.6.

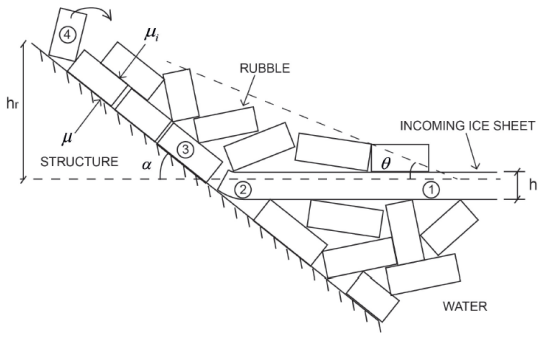


Figure 2.6: Incoming level ice against a sloping structure. Flexural failure causes the ice to break into rubble. (Høyland, n.d.)

Ice breaking ships are often designed to fail the ice by bending. Icebreakers are a type of ship that is specifically designed to break the ice in bending by pushing the ship up over the ice and using its weight to fail the ice by crushing and bending.

As the ship hits the ice, the ice is crushed at the contact region. The contact area increases as the ship moves forward into the ice. The force acting on the ice can be decomposed into a vertical and a horizontal component. As the contact area increases, so does the vertical force acting on the ice. This creates bending stresses in the ice cover and when the flexural strength of the ice is reached, the ice will fail in bending some distance ahead. This process is illustrated in Figure 2.7. The pressure needed to fail the ice in bending is part of the requirements when designing the hull of a ship intended for such use. The broken off pieces will continue to interact with the ship as the ice rotate and slide along the hull. The total ice load acting on the ship will therefore consist of the forces needed for breaking the ice and the forces needed for clearing the ice.

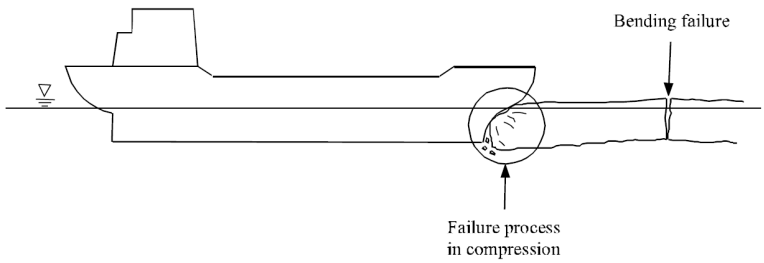


Figure 2.7: Ship ramming an ice floe. The ice is crushed at the interface between the structure and the ice until the vertical force from the vessel cause bending failure a distance ahead. (Jordaan, 2001)

### 2.3.4 Determining Design Loads

The global and local ice forces should be determined using probabilistic methods when designing for ice load resistance. This is done to ensure adequate reliability of the vessel. Through field or experimental tests of impacts, a statistical distribution can be developed from the impact loads. This can be used to determine the maximum annual loads and design loadings for other return periods. (Jordaan, 2001) The design load on a vessel should be based on extremes such as in ULS design.

For floating systems measures can often be taken to avoid icebergs. The areal density of icebergs and measures for detection and avoidance as a function of sea state should also be considered. The ice class of a vessel determines the ice conditions it can have access and thereby be exposed to. Bergy bits and growlers are broken off from larger icebergs and they have a higher probability of occurrence. Larger icebergs can be detected visually and using radar. This makes the probability of impacts with larger iceberg and ships small. However, the consequence of an impact between a ship and an iceberg could be catastrophic.

The peak global loads are strongly dependant on the vessel size when travelling through ice. The mass and velocity of the iceberg is important when assessing the loads on an offshore structure. The velocity and mass determines the kinetic energy of the iceberg. Added masses and the shape of the hull and iceberg will also affect the load level during the impact. (Ritch et al., 2008) The local shape of the iceberg will affect how the forces and energy are transferred to and in the hull.

Loads on the structure can be determined from pressure-area curves given by experiments, rules and standards. Standards may provide a design patch load and size such as in ISO (2010), FSICR (2017b) and DNV GL (2018). The loads and response of a structure-ice impact can also be modelled as an integrated finite element method simulation. The impact between an ice mass and structure is then simulated and more realistic results can be obtained. Numerical models representing ice intended for such purpose have been proposed and some are presented in Chapter 3.

As has been described above, the contact between a structure and ice will vary in shape, size and pressure. A simplified rectangular patch with uniform pressure can be used to represent the local ice loads on a vessel. When representing level ice, the load patch will have a small vertical extent and a large horizontal extent. The ice thickness is not equal to the patch height. The actual load height has been found to be less than the ice thickness as illustrated in Figure 2.8. (Riska and Bridges, 2019) This is due to local failing of the ice such as spalling and crushing before the ice fails in bending. For high speed vessels and cold ice, this load height can be very narrow and the contact pressure can be very high.

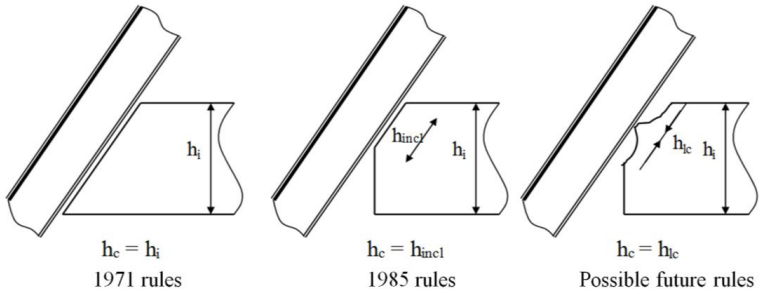


Figure 2.8: Concept of load height on a ship frame. Based on different rule sets of the Finnish-Swedish Ice Class Rules. (Riska and Bridges, 2019)

### 2.3.5 Vessel Resistance

Using conventional ULS design would mean designing for the load with a 100-year return period. This is not the general practice when designing ships for the lower ice classes. The design loads are low for these low classes and damage is expected during the vessels service life. Additional reinforcements could be cost beneficial to the owner depending on how much of the vessel's service life is spent in ice covered waters. The ice classes generally allow for some plastic deformation as the design limit states. Small local dents do not necessarily pose a risk for cracks and water ingress. (Kujala and Ehlers, 2013)

Some special structural considerations needs to be taken for vessels operating in ice infested waters. Icebreakers are designed for breaking through large ice floes and pressure ridges. The conventional bow shape of icebreakers is rounded and smooth. (Canadian Coast Guard, 2019) The icebreaker is shaped to push the ice down and clear the resulting ice pieces. For larger ice features such as large pressure ridges, the ice may take a larger force before failing. The bow of the icebreaker will be pushed upwards over the ice and use its weight to break the ice. If the ice feature does not break, the shape allows the bow to slide back down. This sets additional requirements to the loads the icebreaker must be constructed to withstand. The hull girder section modulus is therefore higher for icebreakers. Ships of lower ice classes are not expected to experience ramming of this magnitude and do not necessarily require a higher section modulus than open water ships. The global bending stresses from heavy seas exceed those of normal operation in ice. (Canadian Coast Guard, 2019)

The midbody of a vessel can have vertical sides making them exposed to crushing forces if caught in ice under compression. The midbody can also be exposed to ice loads if the cleared path is not wide enough, when smaller ice features moves along the side or during manoeuvring. This must be taken into account when designing ships for ice-infested waters. The sides are often strengthened and can be angled

at the waterline. The bottom plating can also experience ice loads if ice is forced underneath the ship, by design or unintentionally as a result of trimming.

There are several failure modes that the local structure must resist, such as bending, shearing, buckling and tripping. The shell plating of icebreakers are supported by main frames, stringers, web frames and bulkheads. The main frames support the local loads and are often designed so that the initial failure is bending collapse of the main frames. There are however many ways of weighing shell plate strength and stiffener strength.

# Chapter 3

# Numerical Ice Models

Several methods have been proposed to model ice. Some of the methods are presented in the following sections. Ice is a less understood material and one single numerical model that describes its mechanical properties has not been agreed upon. Material tests of ice have given scattered results and determining suitable properties are difficult. A comparison of different methods was made in the doctoral thesis of Storheim (2016). Storheim (2016) found that the model by Liu, Amdahl, and Løset (2011) was more aligned with the pressure-area curve from ISO (2010) than the models in Gagnon (2007) and Gagnon (2011).

## 3.1 Crushable Foam Model

Gagnon (2007) simulated collisions between an impact plate and free-floating growlers using a crushable foam material model for the ice. The impact plate could be used to represent part of a ship bow. The software LS-Dyna was used for the simulations and the material type hard crushable foam was taken from its library of materials. The material model was then adjusted to fit results from previous experiments through trial and error.

The material behaves according to the stress-volumetric strain curve shown in Figure 3.1. The impacted elements will exhibit constant non-recoverable deformation as the pressure reaches 0.1 MPa. The deformation will continue up to a fractional volumetric strain of 0.065. The material hardens as pressure increases with the deformation. The curve is shaped so that the centre of the contact region for a blunt iceberg will experience high pressure. This is done to simulate the high pressure zones. The surrounding contact area will experience lower pressure similar to the low pressure zones. The density of the material is set to $\rho = 900$ kg/m$^3$. The elastic modulus used is $E = 9$ GPa. The Poisson's ratio is set to very low and can be taken as $\upsilon = 0$.

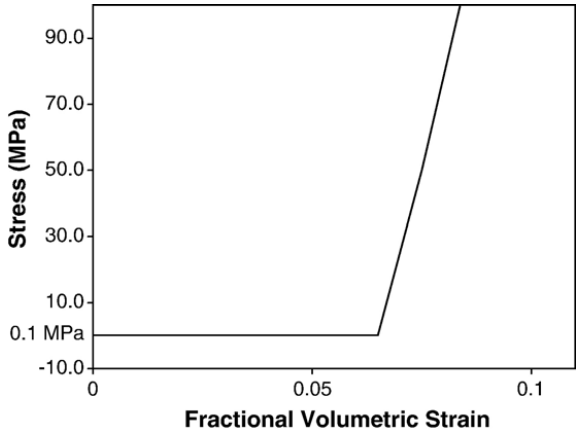


Figure 3.1: Crushable foam material model of ice. The curve defines the relationship between stress and volumetric strain. (Gagnon, 2007)

The material model in Gagnon (2007) resulted in a pressure-area plot that had a fairly stable nominal pressure of around 0.9 MPa. The nominal pressure showed little dependency on nominal contact area. This is in contrast to commonly assumed pressure-area curves for crushing of ice.

The crushable foam model was further developed to account for spalling in Gagnon (2011). Ice crushing against a structure will often produce spalls. A large portion of the ice in the contact region is then expelled and the load is reduced until the intact ice behind the crushed ice comes into contact with the structure. This produces a sawtooth load pattern.

The ice model was constructed to make spall events occur as a function of depth penetration into the ice. The region of the ice that will experience spalling is modelled as a stack of spall layers. There are two sets of distinct and overlapping layers. The layers occupy the same space. One layer has properties for representing intact ice and is denoted M1. The other layer has properties for representing crushed ice and is denoted M2. Each layer is divided into smaller facets. During the impact simulation, the layers exert stress on the structure. The facets representing intact ice is deactivated when spalling occurs. The structure will then be exposed to the forces from the facet representing crushed ice until the next layer of intact ice is reached by the structure. The stress-volumetric strain curve for this model is shown in Figure 3.2. The maximum allowed stress for the ice elements in the M1 facets are 50 MPa and 10 MPa in the M2 facets.

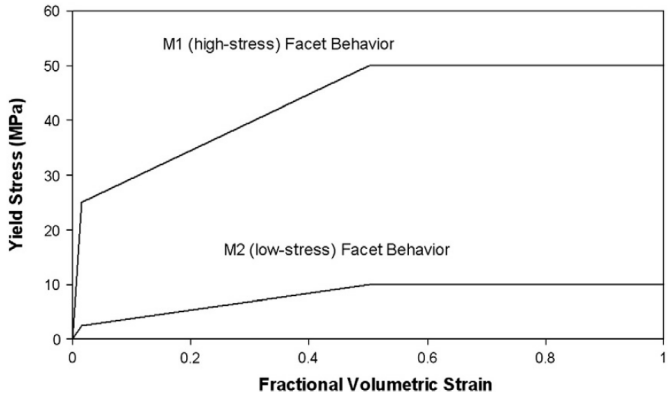


Figure 3.2: Crushable foam material model of ice. The curve defines the relationship between stress and volumetric strain. M1 represents the virgin ice and M2 represents the crushed ice. (Gagnon, 2011)

Any later refinement of the model is not included in this thesis. Liu, Amdahl, and Løset (2011) points out that the crushable foam model suffers from a lack of physical explanation. The crushable foam model was made to match the pressure results from the trials. There is little to no physical explanation of the material and it does not consider cracks and damage to the ice.

## 3.2 Plasticity Based Material Model

Liu, Amdahl, and Løset (2011) propose an elastic perfectly plastic model for iceberg impact scenarios. The model is based on data from triaxial experiments. The iceberg material is considered as isotropic. The stress-strain relationship of ice is strain-rate and temperature dependent.

Confinement of the centre ice particles in the contact area means that the confined ice particles are in a state of triaxial stress. The yield surface is based on the results from triaxial experiments. An elliptical yield surface based on the Tsai-Wu yield surface is used to describe the iceberg behaviour.

$$f(p, J_2) = J_2 - (a_0 + a_1 p + a_2 p^2) = 0 \tag{3.1}$$

$p$ is the hydrostatic pressure. $J_2$ is the second invariant of the deviatoric stress tensor. The Von Mises stress is equal to $\sqrt{3J_2}$. More on the second invariant of the deviatoric stress tensor can be found in the appendix in the article by Liu, Amdahl, and Løset (2011). $a_0$, $a_1$ and $a_2$ are constants that can be determined by fitting to triaxial experimental data. A comparison of yield surfaces based on various data sources can be seen in Figure 3.3. Due to temperature gradients in the iceberg the

strength varies. To account for this, the constants $a_0$, $a_1$ and $a_2$ can be expressed as functions of temperature in equation 3.1.

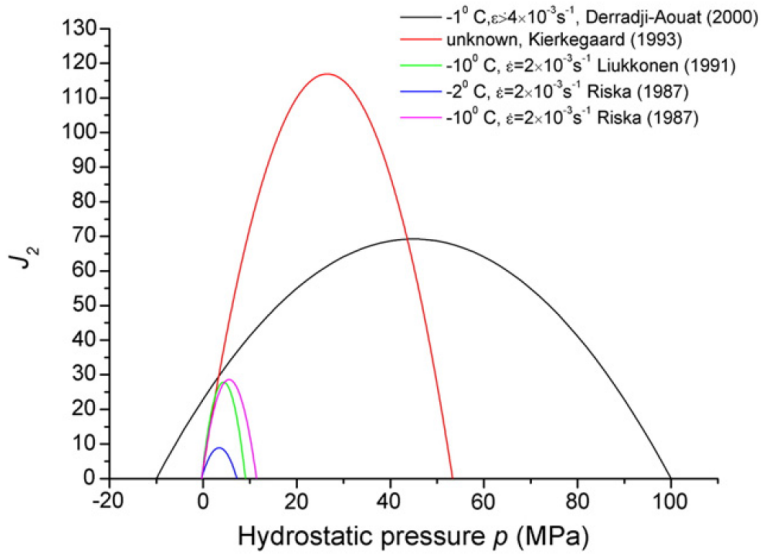


Figure 3.3: Illustration of Tsai-Wu yield surface in $p - J_2$ space. The different yield surfaces are based on various data sources. (Liu, Amdahl, and Løset, 2011)

The strength of ice depends on the strain rate, but lack of experimental data makes it impractical to include this dependency in the model. The yield envelope representative of high strain rates is used instead. An empirical element failure criterion based on effective plastic strain and hydrostatic pressure is included in the model. A failure curve is described in equation 3.2. If the equivalent plastic strain reaches the failure curve, the element will erode.

$$\varepsilon_f = \varepsilon_0 + \left(\frac{p}{p_2} - 0.5\right)^2 \tag{3.2}$$

$\varepsilon_0$ is the initial failure strain. This value should be determined from experimental data. $p_2$ is the larger root of the yield function in equation 3.1. There is also a cut-off pressure $p_{cut}$ that is the maximum tension pressure allowed. The failure curve and cut-off pressure is shown in Figure 3.4.

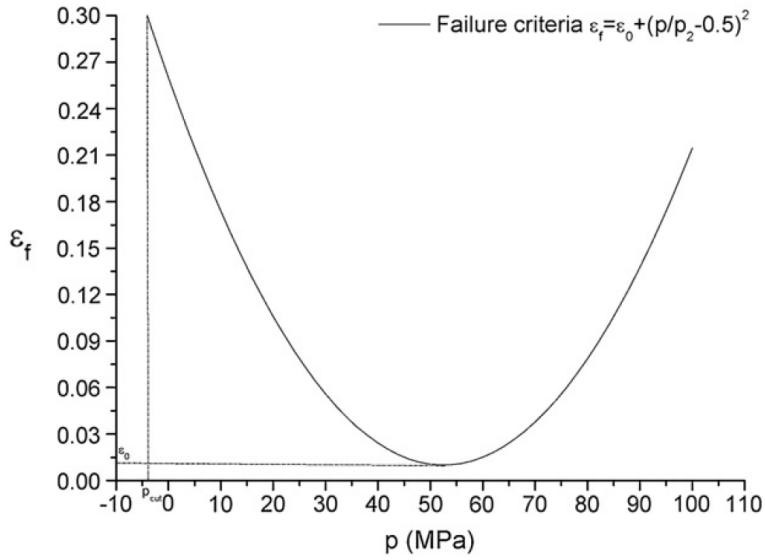


Figure 3.4: Failure criteria curve for $p_2 = 100$ MPa. (Liu, Amdahl, and Løset, 2011)

Elements that violate the failure criterion are deleted. This is called the erosion technique. Using the erosion technique on elastic materials with brittle failures cause stress waves. To avoid this, the material is assumed elastic-perfect plastic.

Liu, Amdahl, and Løset (2011) sets the density of the ice material to $\rho = 900$ kg/m$^3$, the Poisson's ratio is $\upsilon = 0.3$, the elastic modulus is $E = 9.5$ GPa, the cut-off pressure is $p_{cut} = -2$ MPa, the initial failure strain is $\varepsilon_0 = 0.01$. The constants in equation 3.1 are given for some data sets in the article. When considering local deformation of a ship structure during iceberg impacts, the constants recommended are as follows, $a_0 = 22.93$, $a_1 = 2.06$ and $a_2 = -0.023$.

# Chapter 4

# Regulations

The International Maritime Organization (IMO) has a mandatory set of rules for ships sailing in the Arctic and Antarctic regions. The Polar Code aims to provide rules for safe ship operations and environmental protection. (Polar Code, 2015) The Polar Code states that a ship must be assigned a Polar Class for travelling in the polar areas. This Polar Class should be based on IACS Unified Requirements to operate in the Arctic and Antarctic regions.

Before a ship is allowed to navigate the Northern Sea Route (NSR), an application must be submitted to the NSR Administration. The NSR Administration is a Russian federal government institution that must grant permission to the ship before entering the water area of the NSR. Criteria regarding ice class and icebreaker assistance depends on the ice conditions, location along the route and time of year. The Polar Ship Certificate in accordance with the Polar Code must also be presented to the NSR Administration. (NSRA, 2017)

## 4.1 IACS Polar Class

The International Association of Classification Societies (IACS) is an organisation of classification societies. IACS establish minimum technical standards and requirements addressing maritime safety and environmental protection. Members of IACS may have additional rules and standards but must comply with IACS's rules. The regulations for the bow region of a ship with the lowest polar class, PC 7, are presented here. (IACS, 2016) According to FSICR (2017a), the IA ice class of the Finnish-Swedish Ice Class Rules (FSICR, 2017b) is equivalent to IACS PC 7 class.

## 4.2 Design Ice Load

A design scenario is used to determine the necessary scantlings. The design scenario for polar class ships is a glancing impact on the bow. The design load is represented as an average pressure uniformly distributed over a rectangular load patch.

The design ice load depends on several factors. The region of the ship, the shape of the hull, the polar class, the ship displacement,

### 4.2.1 Ice Load Characteristics for Vertical Bow Sides

The region considered should be divided into sub-regions. The waterline length of the bow region is generally divided into four sub-regions of equal length. The ice load characteristics should then be calculated for each sub-region with respect to the mid-length position of each sub-region. The maximum sub-region force, line load and pressure are then used to calculate the ice load parameters. The regulations in this section is applicable to ships with bow forms with vertical sides. The normal frame angle $\beta'$, as seen in Figure 4.1, must be between 0 and 10 degrees.

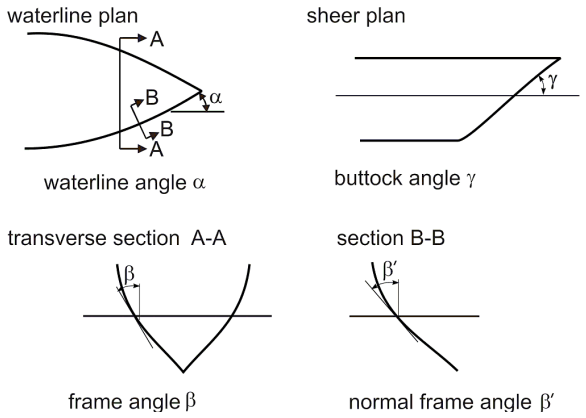


Figure 4.1: Definition of hull angles. (IACS, 2016)

The influence of the hull angles are captured through the shape coefficient $fa_i$ defined in equation 4.1.

$$fa_i = \alpha_i/30 \tag{4.1}$$

The force in MN is given by equation 4.2.

$$F_i = fa_i \cdot CF_{CV} \cdot D^{0.47} \tag{4.2}$$

The line load in MN/m is given by equation 4.3.

$$Q_i = F_i^{0.22} \cdot CF_{QV} \tag{4.3}$$

The pressure in MPa is given by equation 4.4.

$$P_i = F^{0.56} \cdot CF_{PV} \tag{4.4}$$

The notation $i$ indicates which sub-region is being considered. $\alpha$ is the waterline angle in degrees shown in Figure 4.1. $D$ is the ship displacement in ktonnes and is not to be taken less than 5 ktonnes. Class factors depends on the polar class. For PC 7 the class factors are give as follows; Crushing failure class factor $CF_{CV} = 2.60$, Line load class factor $CF_{QV} = 2.33$ and Pressure class factor $CF_{PV} = 0.65$.

### 4.2.2 Ice Load Parameters

The design load patch dimensions can now be found. Each maximum of force, $F$, line load, $Q$, and pressure, $P$, found using equations 4.2, 4.3 and 4.4 shall be used when calculating the ice load parameters.

The ice load patch has a width in m defined by equation 4.5.

$$w = F/Q \tag{4.5}$$

The ice load patch has a height in m defined by equation 4.6.

$$b = Q/P \tag{4.6}$$

The average pressure in the design load patch is given by equation 4.7 in MPa.

$$P_{avg} = F/(b \cdot w) \tag{4.7}$$

## 4.3 Structural Requirements

### 4.3.1 Shell Plate Requirements

The required minimum shell plate thickness, $t$, is given by equation 4.8. The required minimum shell plate thickness is a sum of the thickness required to resist the ice loads on the structure, $t_{net}$, and the thickness to account for corrosion and abrasion, $t_s$. All thicknesses are given in mm.

$$t = t_{net} + t_s \tag{4.8}$$

The required net thickness, $t_{net}$, depends on the orientation of the framing. For transversely framed plating in the bow region the required net thickness is given by equation 4.9 in mm.

$$t_{net} = 500 \cdot s \cdot ((AF \cdot PPF_p \cdot P_{avg})/\sigma_y)^{0.5}/(1 + s/(2 \cdot b)) \tag{4.9}$$

$s$ is the transverse frame spacing in m. $AF$ is the hull area factor. This factor reflects the relative magnitude of the load expected in the area. $AF$ for the bow region of a vessel classified as PC7 is equal to 1.00. $PPF_p$ is the peak pressure factor for the plating and is used to account for pressure concentrations which exist within the load patch. The peak pressure factor is given as $PPF_p = (1.8 - s) \geq 1.2$ for transversely framed plating. The average patch pressure, $P_{avg}$, is defined in equation 4.7. $\sigma_y$ is the minimum upper yield stress of the material in N/mm$^2$. $b$ is the height of the design load patch in m given by equation 4.6. Additionally, $b$ is not to be greater than $l - s/4$, where $l$ is the distance between the frame supports.

The shell plate thickness must have additional thickness to account for corrosion and abrasion. Assuming effective protection of the hull, the additional thickness for a PC7 ship is given as $t_s = 2.0$ mm.

### 4.3.2 Framing

The overall requirement to the framing members of Polar Class ships is that they are to be designed to withstand the design ice load defined in Section 4.2.2. The combined effects of shear and bending are not to exceed the plastic strength of the framing member, i.e. no development of a plastic collapse mechanism.

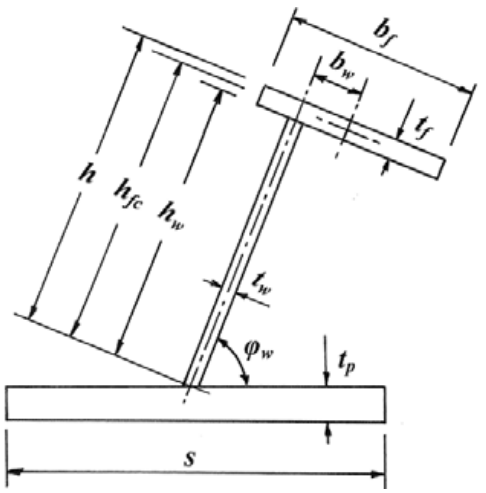


Figure 4.2: Stiffener geometry. (IACS, 2016)

The stiffener geometry can be seen in Figure 4.2. Note that the figure shows the as built dimensions, meaning including additional thickness for corrosion and abrasion. Stiffener webs and flanges within the ice-strengthened hull areas of Polar Class ships are to have a minimum corrosion and abrasion thickness of $t_s = 1.0$

mm. The net thicknesses are used when calculating the shear area and section modulus of the frame members.

### Calculating effective shear area and effective plastic section modulus

The actual net effective shear area, $A_w$, of a local frame is given by equation 4.10 in $\text{cm}^2$.

$$A_w = h \cdot t_{wn} \cdot \sin\varphi_w / 100 \tag{4.10}$$

$h$ is the height of the stiffener in mm. $t_{wn}$ is the net web thickness in mm. $\varphi_w$ is defined as the smallest angle between the midspan of the stiffener web and the shell plate in degrees.

The actual net effective plastic section modulus, $Z_p$, is given in $\text{cm}^3$ by equation 4.11.

$$Z_p = A_{pn} \cdot t_{pn}/20 + \frac{h_w^2 \cdot t_{wn} \cdot \sin\varphi_w}{2000} + A_{fn}(h_{fc} \cdot \sin\varphi_w - b_w \cdot \cos\varphi_w)/10 \tag{4.11}$$

The net cross sectional area of the local frame, $A_{pn}$, is given in $\text{cm}^2$. $t_{pn}$ is the fitted net shell plate thickness in mm. This thickness must not be lower than the required net thickness, $t_{net}$, given in equation 4.9. The height of the local frame web, $h_w$, the height measured to the centre of the flange area, $h_{fc}$, and the distance from mid thickness plane of local frame web to the centre of the flange area, $b_w$, are all in mm and can be seen in Figure 4.2. $A_{fn}$ is the net cross-sectional area of the local frame flange in $\text{cm}^2$. If the cross-sectional area of the local frame is greater than the cross-sectional area of the attached plate flange, the shift of the plastic neutral axis needs to be taken into account.

### Required effective shear area and effective plastic section modulus

The following requirements apply to transverse local frames in side structures. The minimum requirement to the net effective shear area in $\text{cm}^2$ is defined in equation 4.12. $A_w$ from equation 4.10 must be greater than $A_t$.

$$A_t = 100^2 \cdot 0.5 \cdot LL \cdot s \cdot (AF \cdot PPF \cdot P_{avg})/(0.577 \cdot \sigma_y) \tag{4.12}$$

$LL$ is the length of the loaded portion of the span in m. It is taken as the lesser of the local frame span ($a$) and the height of the design ice load patch ($b$). The peak pressure factor, $PPF$, for transverse frames with load distributing stringers is defined as $PPF_t = (1.6 - s) \geq 1.0$. If no load distributing stringers are fitted, then $PPF_t = (1.8 - s) \geq 1.2$.

The minimum requirement to the net effective plastic section modulus in $\text{cm}^3$ is defined in equation 4.13. $Z_p$ from equation 4.11 must be greater than $Z_{pt}$. Note that

$Z_{pt}$ is dependent on $Z_p$, and adjusting the frame scantlings will therefore change $Z_{pt}$.

$$Z_{pt} = 100^3 \cdot LL \cdot Y \cdot s \cdot (AF \cdot PPF \cdot P_{avg}) \cdot a \cdot A_1/(4 \cdot \sigma_y) \tag{4.13}$$

$Z_{pt}$ is to be calculated based on two load conditions. The greater $Z_{pt}$ from the two load conditions is the minimum requirement. The first load condition is the ice load acting at the midspan of the local frame. The second load condition is the ice load acting near a support. The factor $A_1$ reflects these two load conditions.

$A_1$ is to be taken as the maximum of the following equations.

$$\begin{aligned} A_{1A} &= 1/(1 + j/2 + k_w \cdot j/2 \cdot [(1 - a_1^2)^{0.5} - 1]) \\ A_{1B} &= (1 - 1/(2 \cdot a_1 \cdot Y))/(0.275 + 1.44 \cdot k_z^{0.7}) \end{aligned} \tag{4.14}$$

$j$ = 1 for a local frame with one simple support outside the ice-strengthened areas
= 2 for a local frame without any simple supports
$a_1$ = $A_t/A_w$
$k_w$ = $1/(1 + 2 \cdot A_{fn}/A_w)$
$k_z$ = $z_p/Z_p$ in general
=0.0 when the frame is arranged with end bracket
$z_p$ = sum of individual plastic section moduli of flange and shell plate as fitted in cm$^3$
= $(b_f \cdot t_{fn}^2/4 + b_{eff} \cdot t_{pn}^2/4)/100$
$b_f$ = flange breadth in mm
$t_{fn}$ = net flange thickness in mm
= $t_f - t_c$
$t_f$ = as-built flange thickness in mm
$t_{pn}$ = fitted net shell plate thickness in mm
$b_{eff}$ = effective width of shell plate flange in mm
= $500 \cdot s$
$Z_p$ = net effective plastic section modulus of the local frame in cm$^3$
The factor $Y$ is defined as $Y = 1 - 0.5 \cdot (LL/a)$

**Structural stability requirements**

There are requirements to the ratio of web height to net web thickness for any framing member of the structure. The requirements given by equations 4.15 and 4.16 are to prevent local buckling of the frame web. Equation 4.15 applies to bulb, tee and angle sections of framing members. If this requirement is impracticable, then the webs can be stiffened to ensure structural stability.

$$\frac{h_w}{t_{tw}} \leq \frac{805}{\sqrt{\sigma_y}} \tag{4.15}$$

$$t_{wn} \geq 0.35 \cdot t_{pn} \sqrt{\frac{\sigma_y}{235}} \tag{4.16}$$

There are also requirements set to prevent local flange buckling. These requirements are given in equations 4.17 and 4.18.

$$b_f \geq 5 \cdot t_{wn} \tag{4.17}$$

$$\frac{b_{out}}{t_{fn}} \leq \frac{155}{\sqrt{\sigma_y}} \tag{4.18}$$

The flange outstand, $b_{out}$, is given in mm.

# Chapter 5

# Finite Element Method

Physical phenomena can often be described in terms of partial differential equations. Solving the system using analytical methods can be too complicated and almost impossible. An approximate solution to these partial differential equations can be found using the finite element method. The error can be reduced by solving more equations and the approximate solution can then be used for engineering purposes. Problems such as stress analysis, heat transfer and fluid flow can be solved using the finite element method. This chapter is mainly based on the compendium by Moan (2003).

## 5.1 General Finite Element Method

The structure in question is divided, or discretisized, into finite elements. The finite elements are connected by nodes. The body is substituted by the elements and this is called a mesh. The elements are of simple geometry which makes it easier to analyse than the structure as a whole. The mesh influences the accuracy of the results. A finer mesh, meaning a higher number of elements, will generally produce more accurate results than a course mesh.

There are many elements defined for different purposes. There are elements designed for beams, trusses, tubes, plane structures, solid structures and fluids to name some. Each node has degrees of freedom (d.o.f.) depending on what solutions are sought. For structural analysis this may be three displacement d.o.f.s and three rotational d.o.f.s. The displacements of the element nodes are calculated. The element must comply with equilibrium, meaning that the external forces acting on the element will be equal to the internal forces. Continuity of the material when the material is deformed must be satisfied. There should be no cracks or overlaps of the elements. The stress-strain relationships are needed to maintain the compatibility.

The element stiffness relationship is determined, $\mathbf{S} = \mathbf{kv}$. The displacements within the element are calculated based on shape functions and the displacement of the corresponding nodes of the element. The stresses at the edges of the element are represented as nodal forces. This leads to the relationship between nodal point displacements and forces as seen in equation 5.1.

$$\mathbf{S} = \mathbf{kv} + \mathbf{S^0} \tag{5.1}$$

$\mathbf{S}$ is the generalised nodal point forces of the element. $\mathbf{k}$ is the element stiffness matrix and $\mathbf{v}$ is the nodal point displacements. Any applied external load is added as nodal point forces in $\mathbf{S^0}$.

The system is analysed by taking contributions from all elements based on topology. The stiffness matrix for the system, $\mathbf{K}$, is assembled by adding the stiffness from every element stiffness matrix, $\mathbf{k}$, corresponding to the place in the stiffness matrix, $\mathbf{K}$. The load vector, $\mathbf{R}$, is established in a similar manner from the external loads on the elements, $\mathbf{S^0}$. The system stiffness relationship is shown in equation 5.2. $\mathbf{r}$ is the global nodal displacements. Boundary conditions are included in the model as known global nodal displacements or additional stiffness in the stiffness matrix.

$$\mathbf{R} = \mathbf{Kr} + \mathbf{R^0} \tag{5.2}$$

The set of linear equations in equation 5.2 can be solved for the global displacements as shown by equation 5.3.

$$\mathbf{r} = \mathbf{K^{-1}}(\mathbf{R} - \mathbf{R^0}) \tag{5.3}$$

The displacement functions within the element gives the stains. Combined with Hooke's law, the stresses can be calculated.

## 5.2 Nonlinearities

The relationship between load and displacement is not linear when nonlinearities are accounted for. There are three aspects of nonlinearities that will be described below. They are geometrical nonlinear behaviour, material nonlinear behaviour and nonlinear boundary conditions.

### 5.2.1 Nonlinear Geometry

Nonlinear geometry effects are not needed for analyses with small deflections and small strains. Then it is assumed that the displacements are so small that the stiffness will not be significantly affected. Nonlinear geometrical effects should be included for larger displacements such as in an ultimate strength assessment of a structure.

Large displacement of a structure may change its stiffness and the way the load is applied. The stiffness of the system is therefore a function of the displacement, $\mathbf{K}(\mathbf{r})$. This is denoted the secant stiffness. The force-displacements relationship is now nonlinear as seen in equation 5.4.

$$\mathbf{R} = \mathbf{K}(\mathbf{r}) \cdot \mathbf{r} \tag{5.4}$$

The nonlinear stiffness will be the initial linear stiffness corrected for nonlinear geometrical effect. The external load $\mathbf{R}$ and the internal load $\mathbf{K}(\mathbf{r})\mathbf{r}$ have to be equal to satisfy equilibrium. This is done using iterative methods. Some solution methods for solving the nonlinear equation is described in section 5.3. Equation 5.4 expressed on differential form is shown in equation 5.5.

$$d\mathbf{R} = \frac{d}{dr}(\mathbf{K}(\mathbf{r})\mathbf{r})d\mathbf{r} = \mathbf{K_I}d\mathbf{r} \tag{5.5}$$

$\mathbf{K_I}(\mathbf{r})$ is denoted the tangent stiffness or incremental stiffness. It can be written as a combination of the linear stiffness from the initial condition and the change in incremental stiffness due to geometrical changes. This is shown in equation 5.6.

$$\mathbf{K_I}(\mathbf{r}) = \mathbf{K_0} + \mathbf{K_G}(\mathbf{r}) \tag{5.6}$$

The correlation of the different stiffnesses mentioned has been illustrated in Figure 5.1.

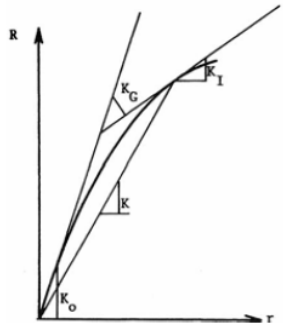


$K_o$- linear (initial) stiffness
K - secant stiffness
$K_I$ - incremental (tangent) stiffness
$K_G$-geometrical stiffness (negative in the fig.)

Figure 5.1: Stiffness definitions and their interdependence at a stable point. (Moan, 2003)

In order to solve equation 5.5 using incremental or iterative methods, the equation is written on a finite incremental form as shown in equation 5.7.

$$\mathbf{K_I}\Delta\mathbf{r} = \Delta\mathbf{R} \tag{5.7}$$

Increments of load and the corresponding increment of displacements are represented by $\Delta\mathbf{R}$ and $\Delta\mathbf{r}$ respectively. The stiffness can be found for a condition of displacement and load, and then the incremental displacement can be calculated from the stiffness and incremental load.

### 5.2.2 Nonlinear Material

For high stresses, the relationship between stress and strain for a steel material becomes nonlinear. This quality has been described in section 2.1.2. There are three categories of material nonlinearities. When a structure is loaded past the materials yield point and a elastic-plastic behavior is developed such as described in section 2.1.2 is called time-independent behaviour. There are also time-dependent behaviour such as creep of material at high temperatures. Then the effect time has on the relationship between stress and strain are of interest. The third category is viscoelastic/viscoplastic behaviour. The stress is then dependent on the strain rate and the effects of creep and plasticity are exhibited.

### 5.2.3 Nonlinear Boundary Conditions

Large displacements of a structure may lead to contact with other components or structures. Two surfaces coming into or out of contact often leads to nonlinear boundary conditions. The size of the contact area can change and may not be proportional to the applied load. The displacements are therefore not linearly dependent on the applied loads any more. An example of a nonlinear boundary condition is shown in Figure 5.2. The load on the structure causes displacements. The structure comes into contact with a rigid surface. The resulting load-displacement curve of the scenario is shown to the right. The relationship is clearly nonlinear. If the ball in the figure was not rigid, but undergoes a deformation, the load-displacement curve would be different, but it would still be nonlinear.

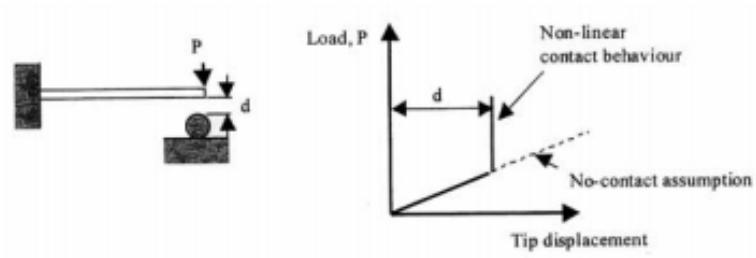


Figure 5.2: Tip of a cantilever comes into contact with a rigid surface. The load-displacement relationship becomes nonlinear. (Moan, 2003)

## 5.3 Nonlinear Solution Techniques

There are several methods for solving nonlinear problems. An incremental and an iterative solution technique will be presented in this section. The solution techniques uses different methods to solve the nonlinear equation presented in equation 5.4. The choice of solution method depends on the structural problem

and the efficiency and accuracy required. Combining methods can increase the solution efficiency and accuracy.

### 5.3.1 Euler-Cachy Method

The external load is applied stepwise when using an incremental method. The Euler-Cauchy method is described in Moan (2003) and illustrated in Figure 5.3. The procedure is described by equation 5.8. The initial displacement,$\mathbf{r_0}$, is assumed zero. The incremental load, $\mathbf{\Delta R}$, is calculated as the difference between the load of the next step and the current. The displacement increment, $\mathbf{\Delta r}$, is calculated for each step based on the incremental stiffness of the current step and the incremental load. The accumulated displacement is then calculated by adding the displacement increment to the current increment. The total displacement is found when the total load has been applied.

$$\begin{aligned} \Delta\mathbf{R}_{m+1} &= \mathbf{R}_{m+1} - \mathbf{R}_m \\ \Delta\mathbf{r}_{m+1} &= \mathbf{K_I}(\mathbf{r}_m)^{-1}\Delta\mathbf{R}_{m+1} \\ \mathbf{r}_{m+1} &= \mathbf{r}_m + \Delta\mathbf{r}_{m+1} \\ \mathbf{r}_0 &= \mathbf{0} \end{aligned} \tag{5.8}$$

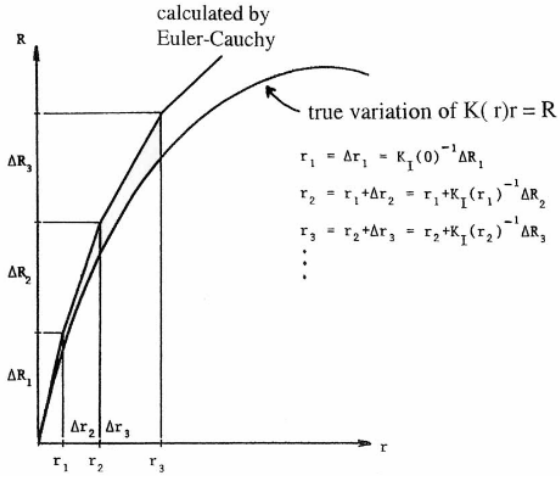


Figure 5.3: Illustration of the Euler-Cauchy method for a single degree of freedom. (Moan, 2003)

There is no correction for equilibrium using this method. This results in a difference between the external load and the true internal load in the system. This can be seen in Figure 5.3 by the deviation of the two graphs. The deviation can be decreased

by using smaller load increments. There are methods that improve on the Euler-Cauchy method. The equilibrium can be corrected for, but this requires additional computational effort.

### 5.3.2 Newton-Raphson Method

The Newton-Raphson method is an iterative method for solving non-linear structural problems. The method is described in Moan (2003) and ANSYS (2019a). **R** is the load applied to the structure. The internal load, **Ri**, for a defined displacement vector, $\mathbf{r_n}$, is calculated. The difference in applied load and internal load gives the residual load. This is a force imbalance in the structure. The iteration method is carried out until this force imbalance is smaller than a given criteria. Then the approximate solution has been found. The convergence criteria can also be set to a small change of displacement from one iteration to the next. Figure 5.4 illustrates the method.

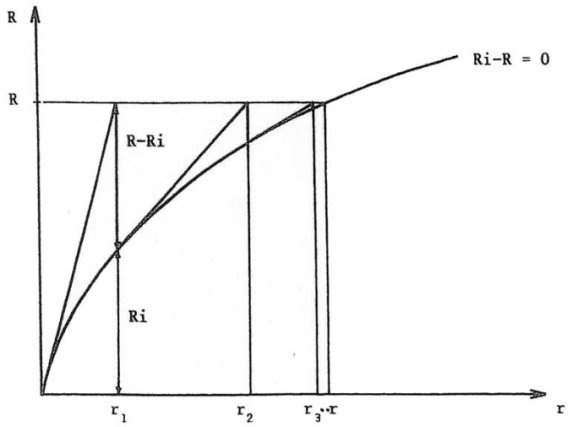


Figure 5.4: Newton-Raphson iteration for a single degree of freedom. The solution for the iterations converges toward the equilibrium state with load R and displacement r. $K_I$ is updated for each iteration. (Moan, 2003)

The method begins with assuming the unknown d.o.f. values of $\mathbf{r_0}$. The assumed values should be equal to zero for the first iteration, or equal to the converged solution of the previous substep or load step. The updated tangent stiffness, $\mathbf{K_I}$, is then computed. The restoring force vector, **Ri**, is calculated from the element stresses for this configuration of $\mathbf{r_n}$. $\mathbf{\Delta r_n}$ is calculated based on the current stiffness and residual load. $\mathbf{\Delta r_n}$ is added to the current displacements $\mathbf{r_n}$ to obtain the next approximation of displacements, $\mathbf{r_{n+1}}$. This procedure is shown in equation 5.9.

$$\begin{aligned} \mathbf{\Delta r_n} &= \mathbf{K_I^{-1}}(\mathbf{r_n}) \cdot (\mathbf{R} - \mathbf{R_i}) \\ \mathbf{r_{n+1}} &= \mathbf{r_n} + \mathbf{\Delta r_n} \end{aligned} \tag{5.9}$$

The method described above is the full Newton-Raphson procedure and requires the tangent stiffness to be updated for each iteration. This is time consuming and methods for updating the tangent stiffness less frequently has been developed. This will result in more iterations needed to obtain a converged solution, but each iteration will take less time. This could be beneficial and these modified Newton-Raphson iterations are often used. The full Newton-Raphson method is the default for plasticity, contact and large strain nonlinearities in ANSYS. (ANSYS, 2019a)

If path-dependent nonlinearities are included, the load must be applied in increments. In order to account for plasticity, this modified procedure is needed. $\mathbf{r_n}$ must be near the exact solution before the applied load $\mathbf{R}$ can be increased. This combination of incremental and iterative methods are shown in Figure 5.5.

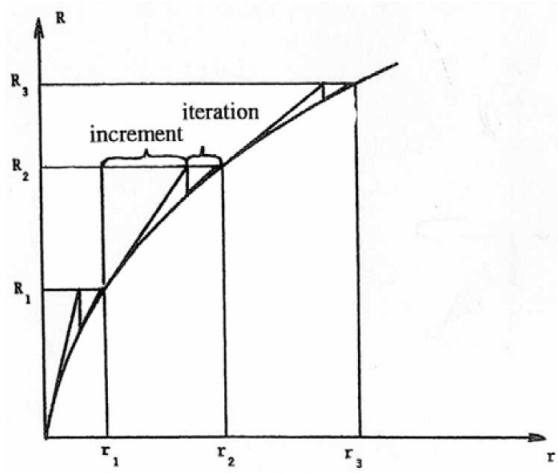


Figure 5.5: Combination of incremental and iterative solution procedures. (Moan, 2003)

In ANSYS, several load steps can be defined. The load in each load step can be applied gradually to the structure using substeps. The full value of the load has been applied at the end of the load step. This is called ramped loading and an illustration can be seen in Figure 5.6.

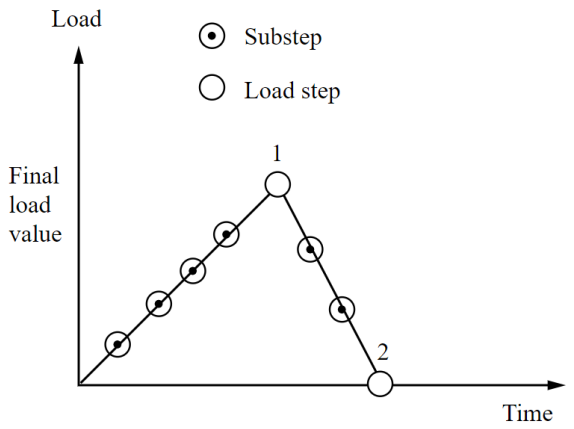


Figure 5.6: Ramped loads with two load steps. The load for each load step is applied gradually. (ANSYS, 2019b)

If the solution did not converge or the analysis was aborted, there are residual restoring forces in the system. The residual restoring forces can indicate where the model is not satisfying equilibrium.

## 5.4 Dynamic Loading

The dynamic equation of motion is given in equation 5.10.

$$\mathbf{M}\ddot{\mathbf{r}}(t) + \mathbf{C}\dot{\mathbf{r}}(t) + \mathbf{K}\mathbf{r}(t) = \mathbf{R}(t) \tag{5.10}$$

The inertia force is a function of the mass matrix, $\mathbf{M}$, and accelerations, $\ddot{\mathbf{r}}$. The damping force is a function of the damping matrix, $\mathbf{C}$, and the velocities, $\dot{\mathbf{r}}$. The restoring force is dependant on the stiffness matrix, $\mathbf{K}$, and the displacements of the nodes, $\mathbf{r}$. $\mathbf{R}$ is the external load.

The eigenfrequencies and eigenvectors or modal shapes can be found by setting the stiffness matrix and applied load equal to zero. The eigenvectors are linearly independent. Any displacement of the structure can be expressed as a linear combination of the eigenvectors.

For deterministic loading, the solution of the dynamic equation of motion can be found as a function of time. For arbitrary loading, the response can be calculated as a function of frequency. The frequency domain solution is suited for stochastic loading. (Langen and Sigbjörnsson, 1979)

### 5.4.1 Impulsive loads

Dynamic loads varies over time. They require a time dependent solution and introduce inertia loads throughout the structure. The external load can be of short duration. If the external load is of same order of magnitude or shorter than the natural period of the system, it is often denoted an impulsive load. (Larsen, 2014) These types of loads can occur for explosions, falling objects, slamming and collisions.

The response calculation can be divided into two phases for such loads. The first phase is the time the system is exposed to the load, and the second phase when the system is not exposed to the load and oscillates. This is illustrated in Figure 5.7. The effect of damping of the system shown, is assumed to assert itself after several response oscillation periods. The maximum response will occur either in the first or the second phase.

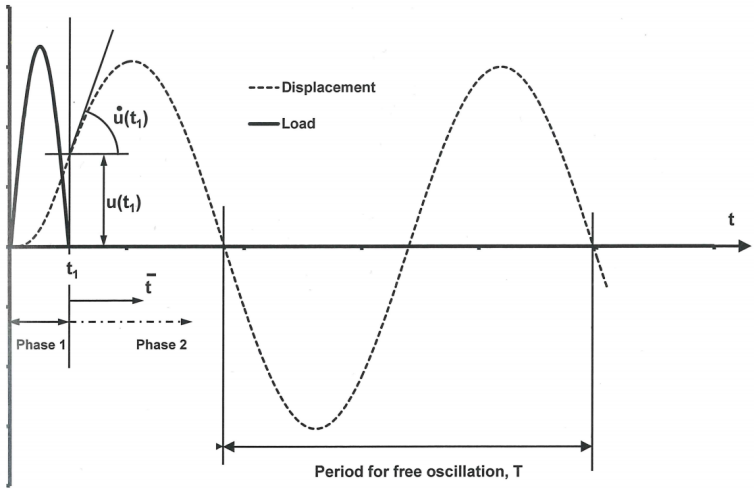


Figure 5.7: Response of lightly damped system to impulsive load. The load and response history are represented by solid and dotted lines respectively. (Larsen, 2014)

### 5.4.2 Explicit Dynamics Analysis

Explicit methods defines the displacements of the next time step based on displacements, velocities and accelerations of the previous time steps. Implicit methods defines the displacements of the next time step based on velocities and accelerations at the new time step in addition to historical information at previous time steps. The implicit method solves equation 5.10 for $\mathbf{r}$ while the explicit methods aim to solve for $\ddot{\mathbf{r}}$. The implicit method is generally a more time consuming process as it

requires the calculation of the inverse of the stiffness matrix.

An explicit dynamics analysis can determine the dynamic response of a structure for events of short time scales. The dynamic response is due to stress wave propagation, impact or rapidly changing time-dependent loads. In an impact, momentum exchange between bodies and inertial effects are usually important aspects of the analysis. Nonlinearities as mentioned in Section 5.2 are included. This section is based on the theory used in the analysis software ANSYS Explicit STR using the AUTODYN solver. (ANSYS, 2019c)

The Explicit Dynamics system in ANSYS can simulate nonlinear structural mechanics. The simulation can include one or more of the following; impact from low (1 m/s) to very high velocity (5000 m/s), stress wave propagation, high frequency dynamic response, large deformations and geometric nonlinearities, complex contact conditions, complex material behaviour including material damage and failure, nonlinear structural response including buckling and snapthrough, failure of bonds/welds/fasteners, shock wave propagation through solids and liquids, rigid and flexible bodies. (ANSYS, 2019c)

The solution process is illustrated in Figure 5.8. The motion of the nodes gives the deformation of the elements. This deformation changes the volume and density of the elements. The material strain rates are found using the rate of deformation. The material stresses are then found from the material strain rates and transformed into nodal forces. Any external load is then applied as nodal forces. The nodal accelerations are found by dividing the nodal forces by the nodal mass. The nodal velocities and nodal displacements are found through explicit integration of the nodal accelerations.

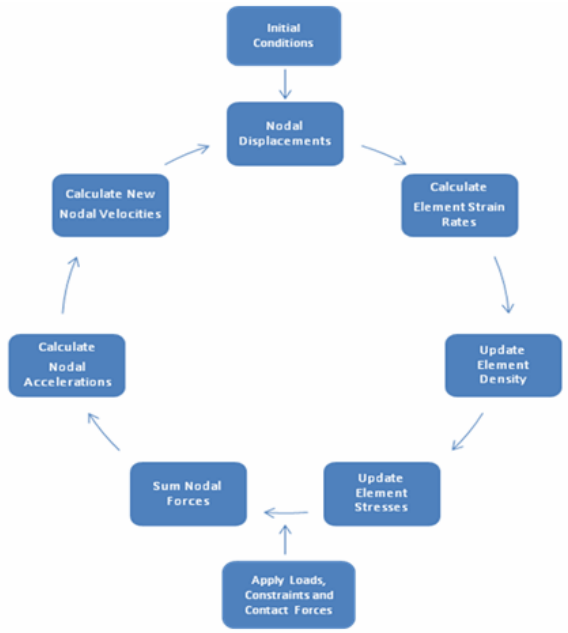


Figure 5.8: The solution process of the Explicit Dynamics analysis. (ANSYS, 2019c)

Conservation of mass, momentum and energy are calculated for each element based on input values at the end of the previous time step. The results from the previous time step is used to predict results for the next point in time. The explicit method does not enforce the dynamic equilibrium throughout the analysis. To ensure stability and accuracy, small time increments are used.

The solver uses a central difference time integration scheme. This is also known as the Leapfrog method. A more detailed explanation can be found in Moan (2003). The nodal accelerations are calculated using equation 5.11.

$$\ddot{r}_i = \frac{R_i}{M} + b_i \tag{5.11}$$

$\ddot{r}_i$ are the components of nodal acceleration where $i = 1, 2, 3$. $R_i$ are the forces acting on the nodal points. The forces, $R_i$, are divided by the the mass attributed to the node, $m$. $b_i$ are the components of body acceleration and are included in the nodal acceleration. This gives the acceleration at time $n$.

The velocities at time $n + 1/2$ are found using equation 5.12 where $\Delta t$ is the time step.

$$\dot{r}_i^{n+1/2} = \dot{r}_i^{n-1/2} + \ddot{r}_i^n \Delta t^n \tag{5.12}$$

The nodal positions at time $n+1$ are then found by integrating the nodal velocities.

This is done using equation 5.13.

$$r_i^{n+1} = r_i^n + \dot{r}_i^{n+1/2} \Delta t^{n+1/2} \tag{5.13}$$

These equations can be solved directly and no inversion of the stiffness matrix is needed. Stability and accuracy of the solution depends on a small time step. The size of the time step is limited by the Courant-Friedrichs-Lewy (CFL) condition. In a single time step, a disturbance or stress wave can not travel farther than the smallest characteristic element dimension in the mesh. This gives the criteria in equation 5.14.

$$\Delta t \leq f \cdot \left[\frac{h}{c}\right]_{min} \tag{5.14}$$

A stability time step factor, $f$, is included. This factor is set equal to 0.9 by default in ANSYS Explicit Dynamics. $h$ is the characteristic dimension of an element. $h$ is different for different types of elements. For quad shell elements, $h$ is equal to the square root of the shell area. $c$ is the local material sound speed in an element. The element in the model that gives the smallest value of $h/c$ is used to calculate the time step. It is important, with respect to time, to be aware that the smallest element will dictate the time step for the whole analysis.

# Chapter 6

# Previous Work

## 6.1 Bergy Bit Impact Trials on CCGS Terry Fox

Transportation of crude oil off the coast of Canada is affected by the presence of glacial ice and bergy bits can be difficult to detect using marine radar under certain sea states. Full scale bergy bit impact trials were carried out on the CCGS Terry Fox in June 2001 to get a better understanding of the loads from impacts with bergy bits. The ship impacted ice masses of various sizes at various speeds. The impact trials were described in Gagnon et al. (2008) and its accompanying papers.

The CCGS Terry Fox is part of the Canadian Coast Guard's icebreaking fleet and was equipped with instruments as shown in Figure 6.1. There were three measurement systems on the ship to determine the impact loads. The strain gauge panel was an area of the bow equipped with 120 strain gauges. The IMD panel was a panel construction that would deflect during an impact. The outer steel panel was painted on the inside and separated from a slab of transparent acrylic. During an impact the painted panel would make contact with the acrylic and the contact area was measured using cameras. The third measuring system was the MOTAN inertial measurement system. A MOTAN sensor consisted of three accelerometers and three angular rate sensors. This sensor system could then determine the ice-induced global forces on the ship. The vessel could aim for an impact on the strain gauge panel or the IMD panel.

A supporting vessel and its auxiliary boat accompanied the CCGS Terry Fox in the trials. This supporting vessel carried out profiling of the bergy bits, temperature gradients, stereo photographs, ice samples and towing of bergy bits to more suitable locations for impacts with the CCGS Terry Fox. The impacted icebergs ranged from 21 tonnes to 22 000 tonnes. Impacts between vessels and icebergs or bergy bits are often below the waterline. The underwater shape is therefore

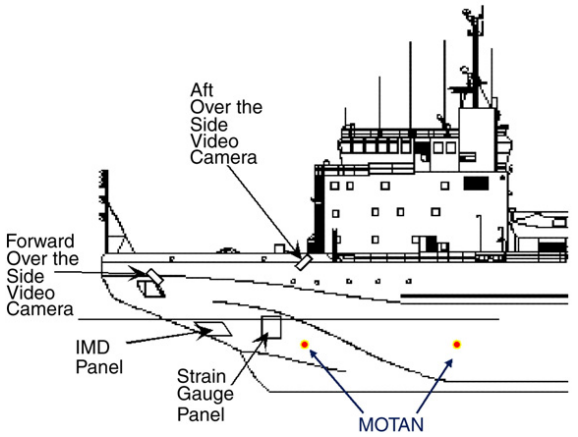


Figure 6.1: Instrument locations on CCGS Terry Fox. (Gagnon et al., 2008)

important to the location of contact and the development of contact area during impact. A multibeam sonar unit was mounted to the supporting vessel. The vessel moved around the ice mass to create a three dimensional surface of the ice. The setup can be seen in Figure 6.2. Ice samples from the contact zone was collected for microstructural analyses.

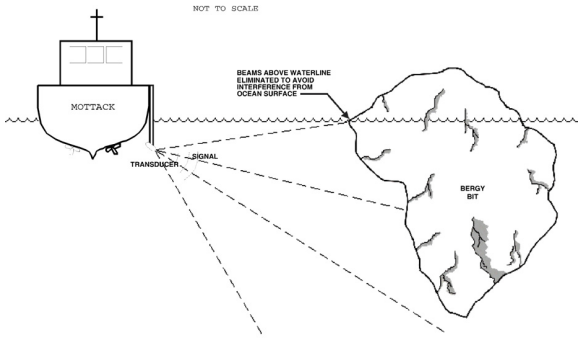


Figure 6.2: Sonar mounting configuration. (Ralph, McKenna, and Gagnon, 2008)

The ice temperature affects the pressure exerted on structures during a collision. A temperature probe was used to record iceberg temperature profiles. The outer layer of the icebergs were warmer than the cool inner core. The outer layer of an iceberg is exposed to air and waves. Over time this will affect the temperature profile. Collisions with the outer layer is expected to produce lower forces than collisions with colder and more competent ice of the core. This was not verified during the impact trials as hitting the iceberg at the same area proved too difficult. The temperature profiles were steep due to it being summer and the ice was rapidly

melting at that time. (Ralph, McKenna, and Gagnon, 2008)

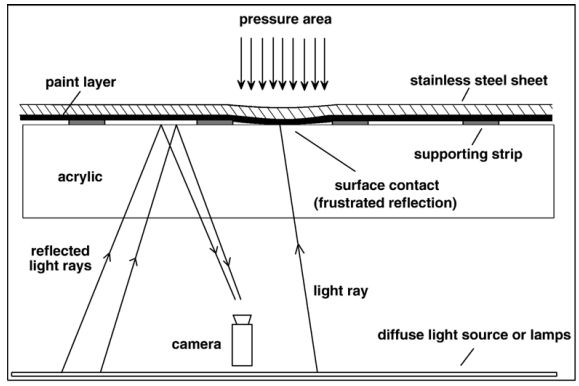


Figure 6.3: The operating principle of the IMD panel.

### 6.1.1 Strain Gauge Panel

An area on the port bow of the CCGS Terry Fox was equipped with strain gauges to measure shear strain in 60 locations. The stain gauge panel as seen in Figure 6.1 contained 120 strain gauges. The measurement area was 5.4 $m^2$. The set up and use of the strain gauge panel is described in the article by Ritch et al. (2008).

The area was divided into 34 individual cells. A uniform load was then applied to each cell and the responses at the gauge locations were determined. These loads and responses were used to form an influence matrix. A finite element model of the bow area was developed. The response of the gauges, when subjected to a known load, was used to adjust and validate the finite element model. The measured strains were converted to pressures and forces on the hull of the finite element model. The measured strain from an ice impact could then be converted to uniform pressures at the cells. This method proved to overestimate the pressure load for some load cases.

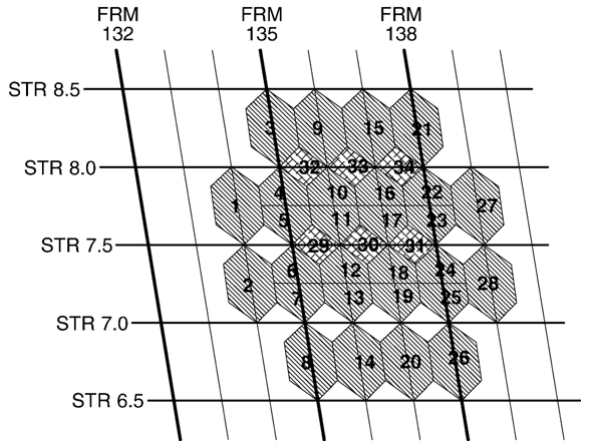


Figure 6.4: Assumed load patch areas, or cells, for the strain gauge panel. (Ritch et al., 2008)

Ritch et al. (2008) concludes that mass of the bergy bit had a clear effect on the impact pressure, but the influence of vessel impact speed was less clear. It did however "show a general trend of higher pressures for higher velocities."

## 6.2 Fluid-Structure-Interaction analysis of an Ice Block-Structure Collision

Song, Kim, and Amdahl (2015) analysed the response of colliding bodies considering the surrounding seawater (FSI) and included an experiment in tank and simulation using LS-DYNA.

Smaller ice masses pose a significant risk to operations in the Arctic. The structural response of high energy encounters with bergy bits or growlers is therefore studied.

In Lee and Nguyen (2011) the waves made by the ship affected the motions of the iceberg. The water layer entrapped between the ice and ship gave a squeezing pressure that also affected the relative drift velocity between the bodies.

The experiment was done in a tank with a 1000 kg ice block towed using ropes hitting a target panel (stiffened plate) bolted to a floater at 1 m/s and 2 m/s. 18 impact tests were done and test no. 11 was a central impact and used as an analysis object assuming an ice block of 850 kg at 2 m/s.

The modelling techniques used by Gagnon and Derradji-Aouat (2006) with mi-

nor changes. Spherical ice block radius of 0.61 m. Included water and air. They used rigid bodies as this speeds up the calculation. Test no. 11 crushed the ice with no permanent deformation to the plate. Therefore floater simulated as rigid body. The back half of the ice mass was also modelled using rigid bricks. The front part of the ice model had rigid body properties before impact, but was deformable at impact.

Some of the results are presented below.

Table 6.1: Results of impact no. 11.

| | Experiment | Simulation |
|---|---|---|
| Panel deflection: | 0 | |
| Peak load force (kN): | 222 | 203 |
| Velocity of ice before impact: | 1.8 | 1.82 |
| Velocity of floater before impact: | 0.1 | 0.15 |
| Velocity after impact common*: | 0.2 | 0.35 |
| Max sway acceleration floater: | 21 | 23 |

*0.3 from collision mechanics

Added mass in simulation was 0.31, but 0.4 is commonly used in traditional approach to collision between two ships. The added mass will depend on the duration of the collision and the relation between the collision force and the deformation.

# Chapter 7

# Modelling Ship-Ice Impact

Two plates of different strength were modelled. The plates are assumed part of the hull on the bow of a vessel intended for ice-infested waters. The two plates were exposed to three static loads. One load was the design load from IACS and the two other loads were taken from a field experiment that measured impact loads between a ship and bergy bits. The impact between an ice mass and the two plates were also simulated using explicit dynamics.

When modelling impacts on a ship hull, the loads and material chosen should be conservative. The damage to the vessel should not be underestimated when modelling an impact scenario, meaning that the real expected damage to a structure and its consequence should be less than for the model.

## 7.1 Plate Model

The plates dimensions are based on IACS polar class PC 7. This is the weakest polar class approved for polar operations. The IACS regulations sets a minimum standard for its members. The member classification societies can have even stricter regulations set for their classes. The design dimensions and load for PC 7 are described in Section 4.1.

The plate is part of the hull of the vessel. It is located in the bow region on the port side and in the waterline. The height of the plate is 3 m and the width is 5 m. Larger transverse frames and stringers are assumed to be placed along the edges of the plate, providing stiffness to the boundaries of the plate model. The edges of the plate and stiffeners was assumed to have fixed boundary conditions.

### 7.1.1 Geometry

Two geometries were established. The simple setup of a plate with one type of stiffeners was decided upon for easier use and comparison to the IACS regulations. This means that the larger grillage system of a realistic ship and potential web stiffeners was excluded. Given the size of the plate this simplification may have been unrealistic. The first geometry was a stiffened plate with 15 relatively weak stiffeners and small shell thickness. The second plate had dimensions according to ice class PC 7 of the IACS regulations.

The first geometry used stiffener dimensions based on stiffener scantlings from the master thesis by Mork (2016). His values were provided by DNV GL and was based on a ship with displacement of 5000 tonnes. It is unsure what type of vessel this model is based on, and the accuracy of the values. The flange thickness and flange width of the original values have been changed from bulb to T profile by keeping the total area of the flange the same. The shell plate thickness was taken as the minimum shell plate thickness required by IACS for PC 7 ships. The resulting dimensions for the first plate can be seen in Table 7.1. This geometry was selected because it could give insight to the failure of the structure.

Table 7.1: First geometry data

| Parameter | Value | |
|---|---|---|
| Shell plate thickness | 19 | mm |
| Number of transverse frames | 15 | |
| Stiffener spacing | 313 | mm |
| Web height | 260 | mm |
| Web thickness | 10 | mm |
| Flange width | 70 | mm |
| Flange thickness | 18 | mm |
| Net effective shear area | 27.80 | $cm^2$ |
| Net effective plastic section modulus | 733.35 | $cm^3$ |

The dimensions of the second plate were decided upon by comparison to the IACS regulations for PC 7 class vessels. This plate included because it would should show how a plate in accordance with the regulations would respond to bergy bit loads. Some assumptions for the vessel was needed when calculating the structural strength requirements and design load according to IACS Polar Class regulations. The polar class of the vessel is assumed PC 7 which is the lowest polar class. The ship is assumed to have a bow form with close to vertical sides and not a bulbous bow. The ship is assumed to have a waterline angle of 30 degrees, and a displacement of 34.882 ktonnes. These features are loosely based on the ship Venta Maersk which was the first conventional container ship to travel through the NSR. (World Maritime News, 2018) A code was written using Matlab to check if the scantlings provided were in agreement with the regulations given by IACS. The regulations

can be seen in Chapter 4.

The values given in Table 7.1 did not provide the structure with sufficient shear area and plastic section modulus. The net effective shear area was 45 % of the requirement, while the net effective plastic section modulus was only 10 % of the requirement. It is worth noting that the required net effective shear area and net effective plastic section modulus is not a given constant, but a function of the input dimensions. Meeting the requirements is therefore an iterative process.

Some scaling and adjusting of the first geometry gives the second geometry as described in Table 7.2. According to the Matlab code, these values will give a structure in agreement with the polar class regulations for PC 7 ships. The dimensions given here are the as-built thicknesses. An addition thickness is added for construction which account for corrosion and abrasion. The two plates are shown side by side in Figure 7.1. The two geometries have the same width and height and the same number of stiffeners. The second geometry has larger stiffeners and thicknesses than the first geometry.

Table 7.2: Second geometry data

| Parameter | Value | |
|---|---|---|
| Shell plate thickness | 30 | mm |
| Number of transverse frames | 15 | |
| Stiffener spacing | 313 | mm |
| Web height | 410 | mm |
| Web thickness | 16 | mm |
| Flange width | 110 | mm |
| Flange thickness | 30 | mm |
| Net effective shear area | 70.40 | $cm^2$ |
| Net effective plastic section modulus | 2884.2 | $cm^3$ |

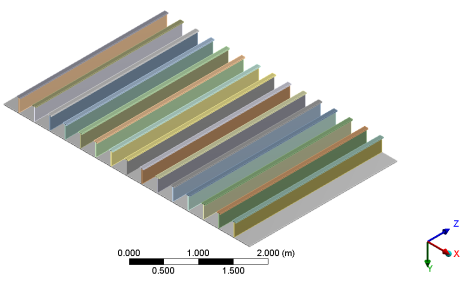


(a) First geometry based on another model.

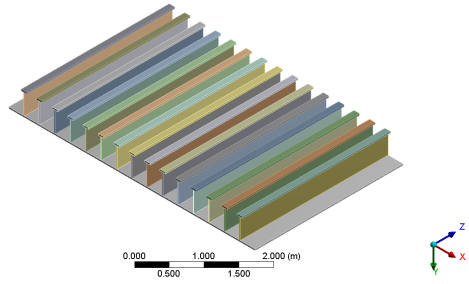


(b) Second geometry in accordance with IACS PC 7 regulations.

Figure 7.1: The two geometries used in the analyses.

### 7.1.2 Material

For simplicity only one steel grade and strength is chosen for the model. IACS defines steel grades for different material qualities. Minimum steel grades for polar regions are defined based on polar class, material class of structural members and the as-built thickness. The class of the vessel is PC7. The shell plating is categorised as the highest material class out of all the structural members included in the model, material class II. The shell thickness is the largest, so this is used to determine a conservative required steel grade. The resulting required steel grade for the model is D. (IACS, 2016)

Based on the location of the plate model, the strength is taken as normal strength steel. According to IACS, normal strength steels have a yield strength of 235 MPa. The maximum strain was set to 22 %. (IACS, 2018) The maximum strain was not included in the static analyses. DNV (2013) proposed a non-linear material curve for S235 steels. The proposed values have been plotted in Figure 7.2. The yield plateau starts at 226 MPa. The difference between the yield point and the proportional limit is usually small. ANSYS therefore assumes that the proportional limit is the yield limit in the analyses. (ANSYS, 2019a) The weight is set to 7850 kg/m$^3$, the same as the weight proposed in DNV (2013).

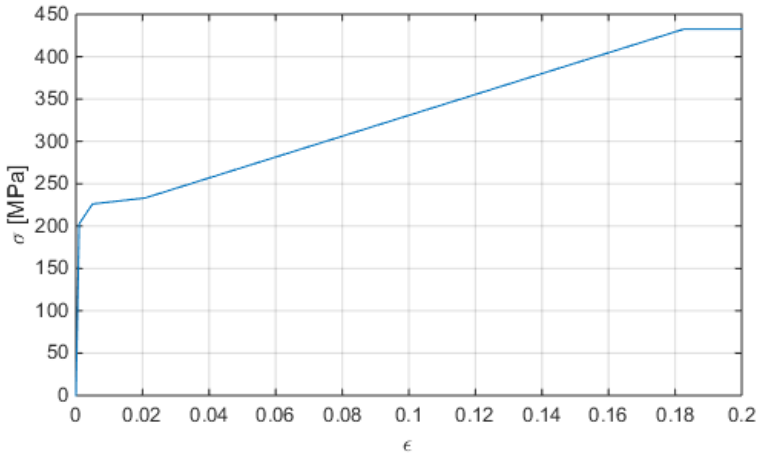


Figure 7.2: True stress-strain curve for S235 steel based on values from DNV (2013).

## 7.2 Static Loading of Plate

A selection of loading conditions were applied to the two plates. The first load is the design load patch from the IACS regulations. The bergy bit impact trials described in Section 6.1 produced load data of bergy bit impacts. Two of these impact loads have been applied to the geometries as static pressure.

### 7.2.1 IACS Design Loading

The procedure for calculating the design ice load is described in Section 4.2. The design ice load is a function of the polar class, location of the area, shape of hull and displacement of the vessel. The design load is a load patch with uniform pressure and can be seen in Figure 7.3. The size of the load patch and the magnitude of pressure can be seen in Table 7.3. The load patch is placed at the centre of the plate.

Table 7.3: Design load patch from IACS regulations.

| Parameter | Value | |
|---|---|---|
| Width | 3.325 | m |
| Height | 1.468 | m |
| Pressure | 2.827 | MPa |

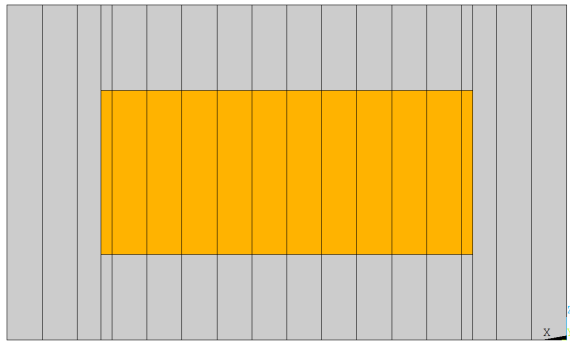

Figure 7.3: The IACS design load from Table 7.3 is applied to the orange area on the outer side of the plate.

### 7.2.2 Bergy Bit Loading B14

The loads measured on the strain gauge panel is described in one of the articles from the impact trials. (Ritch et al., 2008) One impact event in particular has been highlighted. One of the impacts with bergy bit B14 was a direct hit on the panel

and produced the highest single cell pressure and the maximum total load of all the impacts on the panel. B14 had an estimated mass of 1911 tonnes. The applied load patch is taken as the total area subjected to pressure at the time of maximum total force during the impact. The loaded area has been simplified and is taken as quadratic as seen in Figure 7.4. The pressure applied to the load patch is the average pressure on the loaded area as given in Ritch et al. (2008). The values used to apply the load can be seen in Table 7.4 and the area is illustrated in Figure 7.4.

Table 7.4: Bergy bit B14 load.

| Parameter | Value | |
|---|---|---|
| Width | 1.549 | m |
| Height | 1.549 | m |
| Pressure | 2.1 | MPa |

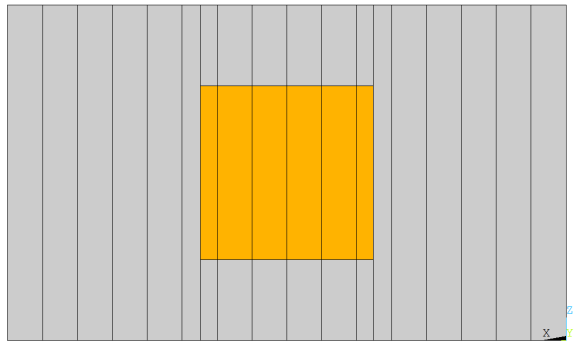

Figure 7.4: The load from bergy bit B14 described in Table 7.4 is applied to the orange area.

### 7.2.3 Bergy Bit Loading B09

The article describing data from the external impact panel highlighted an impact with bergy bit B09. (Gagnon, 2008) Bergy bit B09 had an estimated weight of 243 tonnes and the vessel had a speed of 6 knots at impact. The data for this impact was divided into crushed ice contact and hard ice contact. The load applied to this model was based on the data at peak load of the impact. The load patch was divided into a low pressure zone (LPZ) representing loads from the crushed ice, and a high pressure zone (HPZ) representing loads from the hard ice. The values used to apply this load to the plate can be seen in Table 7.5. Figure 7.5 shows the LPZ and the HPZ.

Table 7.5: Bergy bit B09 load.

| Parameter | Value | |
|---|---|---|
| Width | 0.2471 | m |
| Height | 0.2471 | m |
| Area of LPZ | 0.0448 | $m^2$ |
| Area of HPZ | 0.0164 | $m^2$ |
| Pressure at LPZ | 2.5 | MPa |
| Pressure at HPZ | 10.8 | MPa |

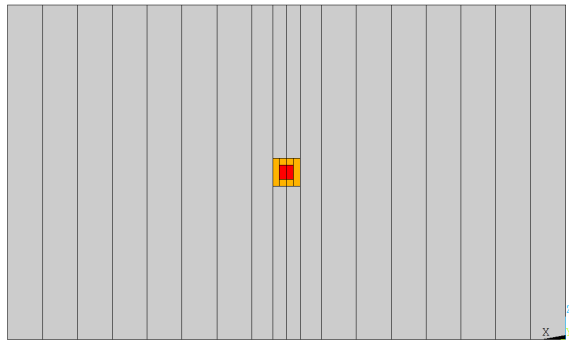

Figure 7.5: The load from bergy bit B09, described in Table 7.5, is applied to the plate. The orange area is the LPZ and the red area is the HPZ.

## 7.3 Dynamic Loading of Plate

Impact between the plates and an ice feature was simulated using ANSYS Explicit Dynamics version 19.2. The same geometries, material and boundary conditions were used for the plates as described in sections 7.1.1 and 7.1.2. The second geometry was exposed to the ice feature first as this stiffened plate would result in small deformations. This would allow for easier examination of the behaviour of the ice model. The results of this simulation showed that the ice feature had not been modelled appropriately. Analysing the ice feature impacting the first geometry was therefore not done as the results would be highly questionable.

The plates were meshed as shown in Figure 7.6. The impact region had a finer mesh to better simulate the forces and response during the impact. The maximum allowed element size was set to the default of about 122 mm. The edges inside the contact region was set to 50 mm along the top and bottom of the plate. The mesh was then finer close to the vertical centre of the plate. Using a bias factor of 3 on the mesh vertically, the middle elements had a maximum size of 17 mm. The stiffeners had a maximum allowed element size of 50 mm.

The maximum allowed element size was larger than the selected mesh size from the mesh convergence tests of the static analyses. The finer mesh in the contact region ensured that a finer mesh was used at the potential contact region. Nodes 1,2,3 and 5 from Figure A.1 were in this area. Compared with the mesh convergence tests this is seen as a fine enough mesh at this area. The maximum mesh size for elements connected to Node 4,6 and 7 is between 17 mm and 50 mm. Compared to the graph for Node 7 in Figure A.11b this may not be optimal. The value had not converged for a mesh size of 50 mm. The mesh could have been finer for the region around Node 7, especially because this is a area associated with large rotational deformation.

The mesh consisted of quad shaped linear shell elements of various size. The elements used are linear because quadratic elements are not recommended for dynamic analysis with wave propagation. This is because the mass is not uniformly distributed in quadratic elements with midside-nodes.

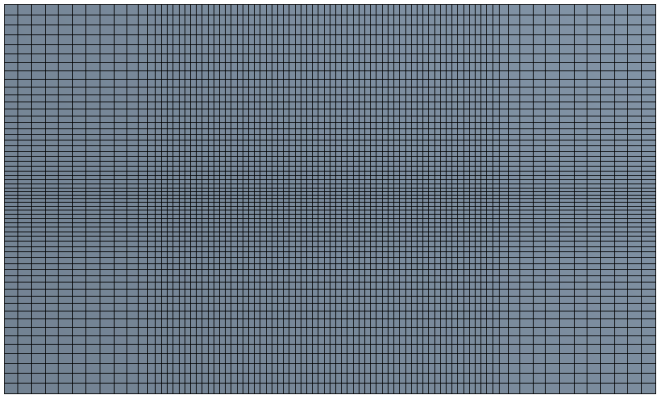

(a) The mesh of second geometry plate. The mesh is finer for the contact region.

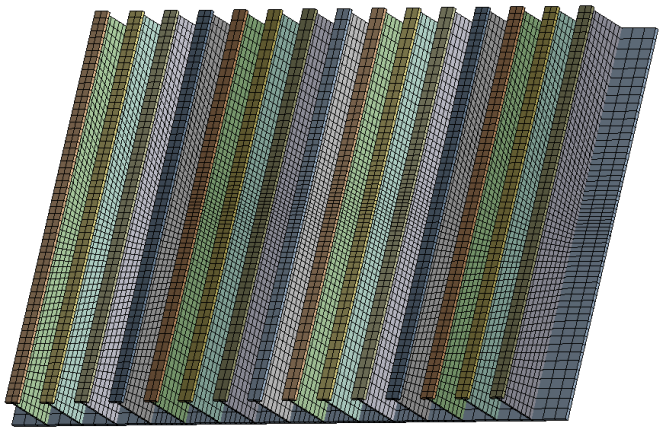

(b) The mesh of second geometry stiffeners. The mesh is finer close to the contact region.

Figure 7.6: Mesh used for the plates. The figures show meshing of the second geometry.

The ice feature was divided into three regions, two deformable regions of ice material and one rigid disk region used to represent the weight of the ice feature not included. The regions will be referred to as the ice region and the disk. The front of the ice feature, meaning the part that would hit the plate first, was modelled as a hemisphere with a radius 1 m. To allow for an indentation in the ice of more than 1 m, and see the behaviour through the ice material, the ice material region was extended with a cylinder shape with a height of 1 m. An alternative could have been to make a larger hemisphere, but the cylinder shape ensured that the contact region would not extend the plate boundaries. The back region of the ice feature was a small disk that would represent the additional weight of the ice fea-

ture. The weight of the disk was 1906 tonnes. The total weight of the ice feature was 1911 tonnes, the same as bergy bit B14 used in the static analysis. This weight was selected so the response from the static analysis could be compared to this one.

The ice shape was meshed using a Cartesian mesh fitted to the geometry. This provided good control of the size of the elements. Other automated mesh methods used in the program resulted in some very small elements. The time step for the analysis depends on the smallest mesh size of the system, and control of the element sizes was therefore important with respect to the total calculation time for the simulation. The maximum allowed element size was set to 122 mm. The mesh consisted of HEX elements. The same mesh technique was used for the disk. The resulting mesh can be seen in Figure 7.7.

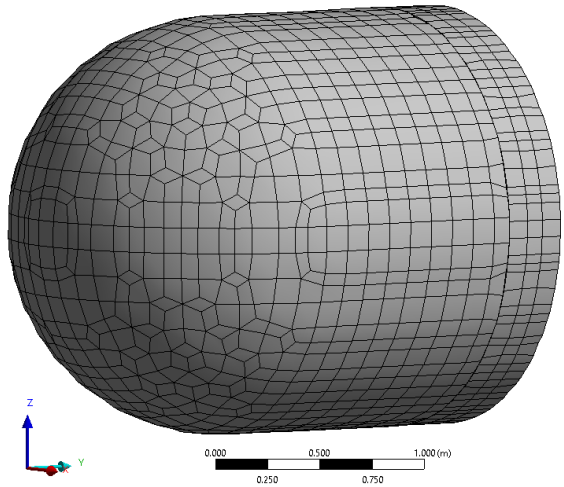


Figure 7.7: Mesh of ice feature. The ice material region and the disk have been meshed separately.

The modelling of the ice material was based on the crushable foam model for intact ice by Gagnon (2011) described in section 3.1. The curve for M1 in Figure 3.2 was included in the model. An additional parameter of maximum tensile stress was required and was set to 1 MPa. This maximum tensile stress was taken from Timco and Weeks (2010). The other properties given to the material was a density of $\rho = 900$ kg/m$^3$, elastic modulus of $E = 9$ GPa and Poisson's ratio of $\upsilon = 0$ as described in Gagnon (2011).

Contacts between the bodies were also defined. For the ice feature, the contact between the ice region and the disk was defined as bonded. This means that no sliding or separation are allowed between the faces. The surfaces are in a way glued together. The contact region between the plate and the ice feature was defined as frictional with a friction coefficient of 0.25 and dynamic friction coefficient of 0.04.

The friction coefficients were taken from Timco and Weeks (2010). Timco and Weeks (2010) notes that there is significant variation in the friction coefficients from measurements. The model proposed by Gagnon (2011) may have assumed frictionless contact as this was not stated in the paper.

The velocity was taken as 3 m/s normal to the plate surface. For a ship travelling in a straight line, as is mostly the case for larger cargo ships, this impact direction is not realistic. The plate was assumed to be placed where the water line angle is 30 degrees. If the ship were to hit the ice feature directly, this would mean that the hit would be oblique, not normal to the surface of the hull. A velocity of 3 m/s, or 5.8 knots, is a low speed for ships in transit. A more realistic simulation would therefore be an impact direction with an angle to the hull and a higher initial velocity. According to Ritch et al. (2008) the effect of velocity on the pressure is not very clear. The speed range for impacts with bergy bit B14 was 1.3 m/ to 3.3 m/s. The impact was simplified by using a velocity of 3 m/s normal to the plate surface.

The end time of the simulation was set to 0.1 s. By this time, the plate would presumably have significant damage or the ice would have been partly crushed. The time step size was automatically set by the program based on equation 5.14 with a time step safety factor of 0.9.

The erosion technique was used for elements with material failure. If all elements connected to a node had been eroded, the inertia of the free node was retained. Retaining the inertia loads for eroded elements may not have been in accordance with the proposed model by Gagnon (2011). In the article, the facets did not interact with any other body after failure and could pass through the other object without interfering with them. The free nodes of this simulation could be involved in impact events and transfer momentum.

The number of shell sublayers was set to five. This was done to achieve better resolution of through thickness plastic deformation. Some other analysis settings was kept as default. The solver used a central difference time integration scheme as described in section 5.4.2. Wave propagation were included in the analysis.

The simulation did not include water. The effect of ship generated waves on the iceberg motion was therefore not accounted for. The squeezing pressure from the entrapped water between the bodies and the added mass of the ice feature was also not accounted for. This would have had an effect on the loads on the hull and the motion of the iceberg. This has been included in previous works (e.g. Lee and Nguyen (2011) and Song, Kim, and Amdahl (2015)).

# Chapter 8

# Results of Static Loading

The results from the different pressure patches applied to the two geometries are presented in this chapter. The displacement and von Mises stresses have been plotted and are placed in a way that makes the response of the two geometries to the same load easier to compare. Additional results are found in the appendices.

## 8.1 IACS Design Loading

The geometries were loaded with the pressure patch given in Table 7.3. The response was then calculated for different mesh sizes. Some of the results are shown in this chapter and some are found in the appendix.

### 8.1.1 First Geometry

No stable solution was found for the first geometry. The magnitude of the load was applied gradually using substeps. The full pressure was applied at time=1. The magnitude of pressure applied at any given time can be found by multiplying full magnitude of pressure and time. Figure 8.1a shows the deflection at the centre of the plate over time for the analysis. The last response was found for time=0.82 which corresponds to a pressure of 2.3 MPa. The plate had a deflection of more than 140 mm at this time. Figure 8.1b shows the residual Newton-Raphson forces. The force imbalance is calculated as the square root of the sum of the squares of the residual component forces FX,FY and FZ. More results in appendix A.1.

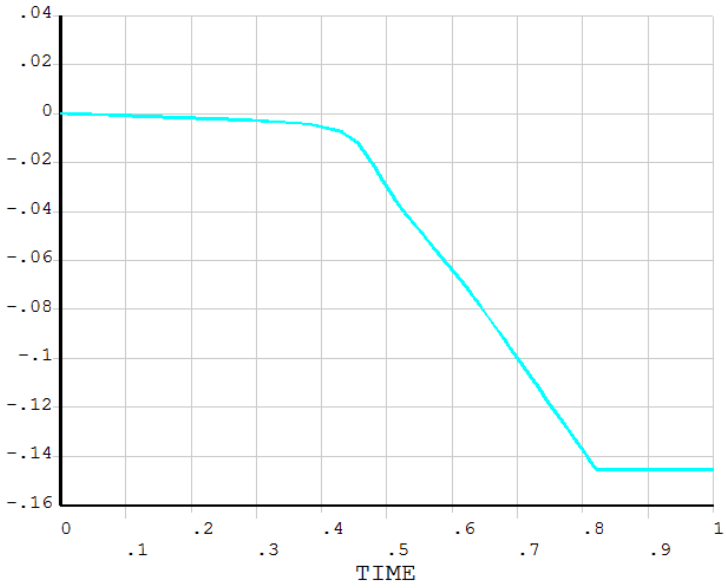


(a) Displacement in m in y-direction at centre of plate over time. Mesh size of 15 mm.

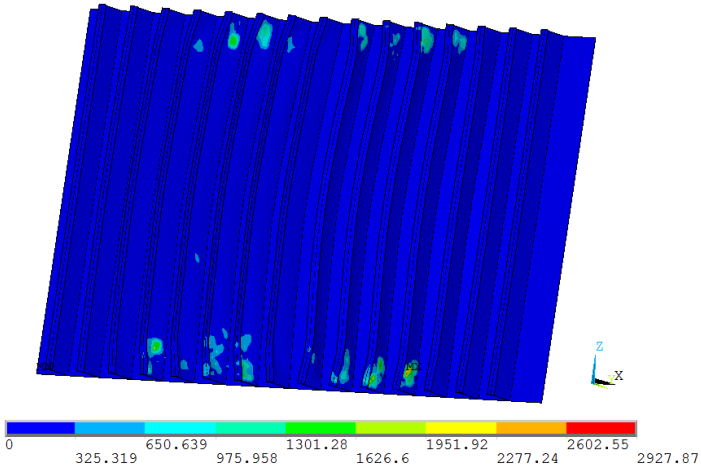


(b) Newton-Raphson residuals. Force imbalance. Taken from analysis using a mesh size of 50 mm. Last computed iteration for the last computed substep.

Figure 8.1: IACS design loading applied to the first geometry.

### 8.1.2 Second Geometry

Convergence and more results in appendix A.2. The maximum displacement of the plate was 2.64 mm and maximum von Mises stress was 213 MPa located close to the stiffener ends.

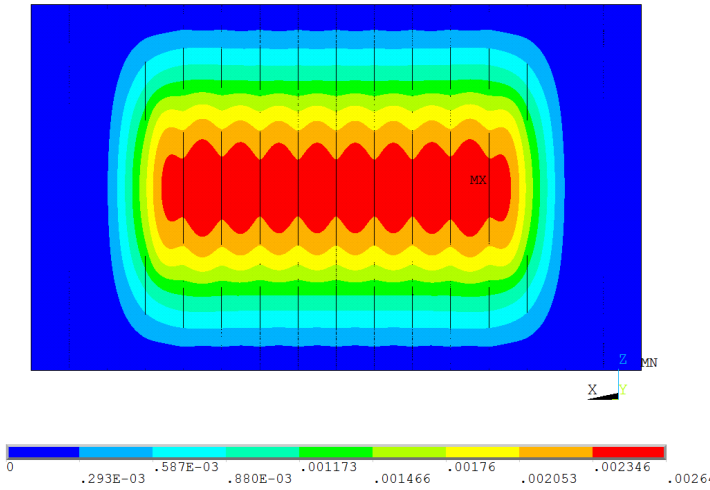


(a) Displacement vector sum in m.

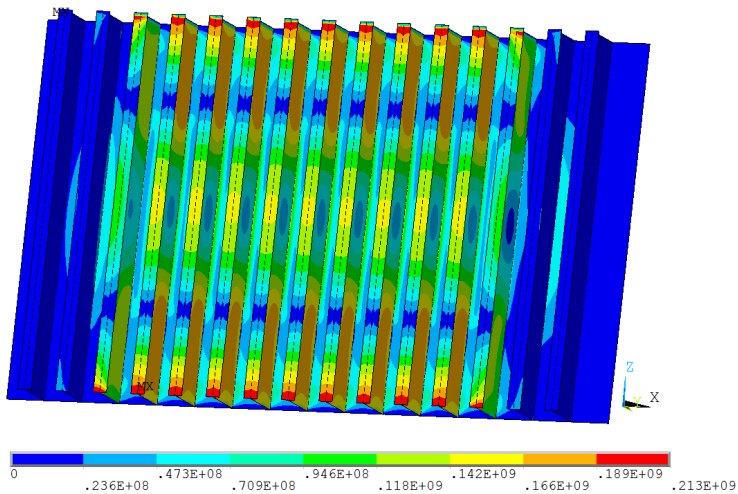


(b) Von Mises stress in Pa.

Figure 8.2: Design loading applied to the second geometry with a mesh size of 15 mm.

## 8.2 Bergy Bit Loading B14

### 8.2.1 First Geometry

Convergence and more results can be found in appendix A.3.

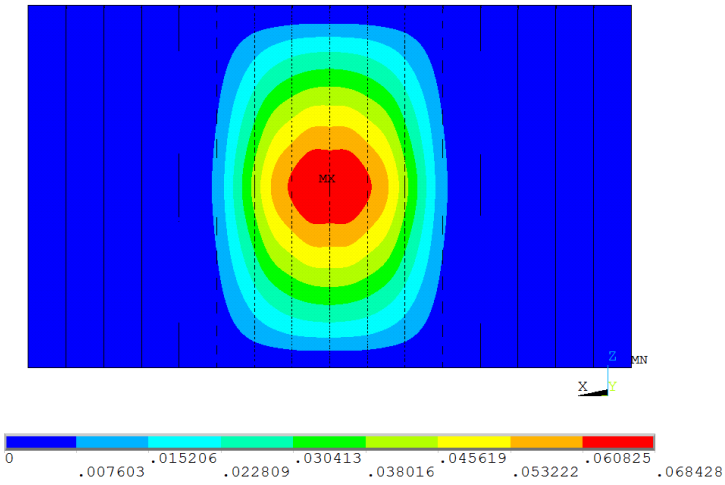


(a) Displacement vector sum in m.

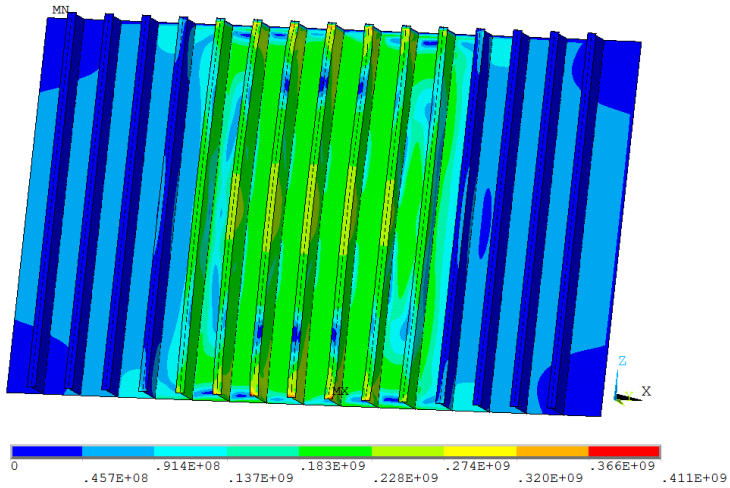


(b) Von Mises stress in Pa.

Figure 8.3: Bergy bit B14 loading applied to the first geometry with a mesh size of 15 mm.

### 8.2.2 Second Geometry

Convergence and more results can be found in appendix A.4.

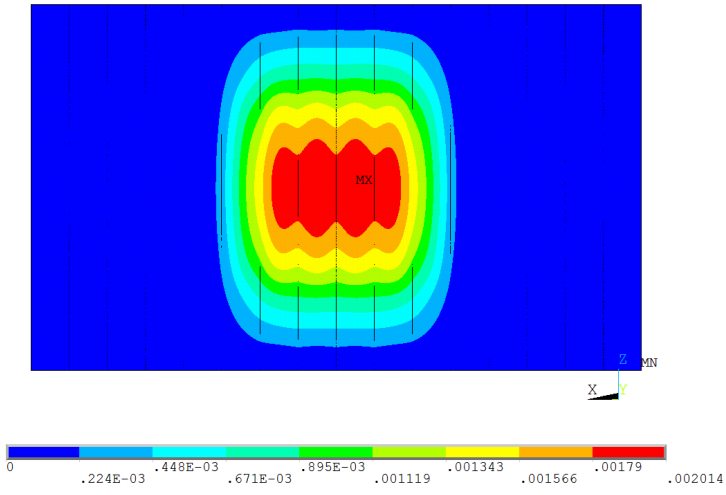


(a) Displacement vector sum in m.

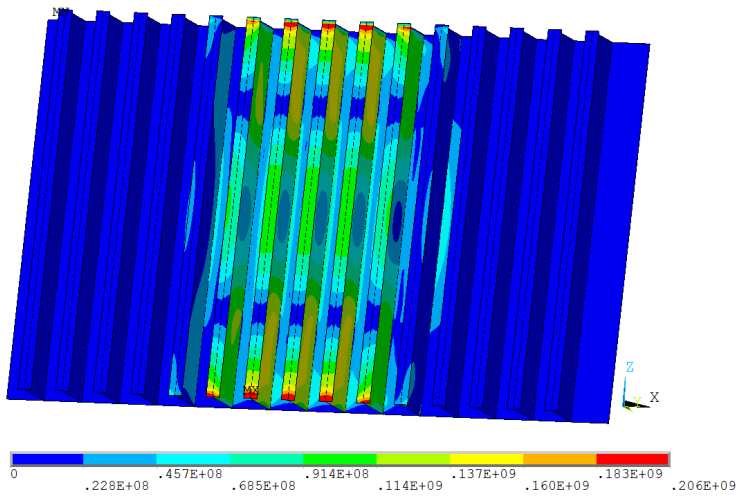


(b) Von Mises stress in Pa.

Figure 8.4: Bergy bit B14 loading applied to the second geometry with a mesh size of 15 mm.

## 8.3 Bergy Bit Loading B09

### 8.3.1 First Geometry

Convergence and more results can be found in appendix A.5.

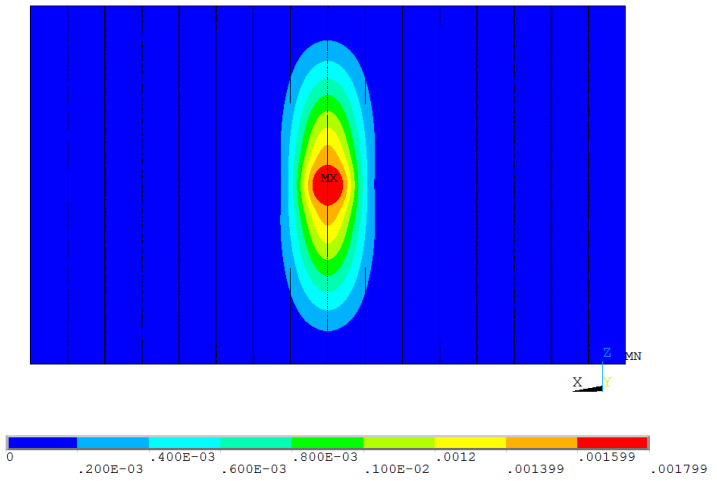


(a) Displacement vector sum in m.

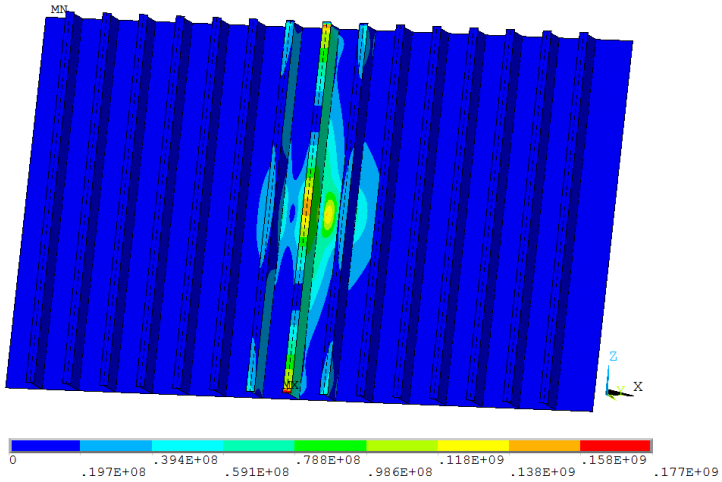


(b) Von Mises stress in Pa.

Figure 8.5: Bergy bit B09 loading applied to the first geometry with a mesh size of 15 mm.

### 8.3.2 Second Geometry

Convergence and more results can be found in appendix A.6.

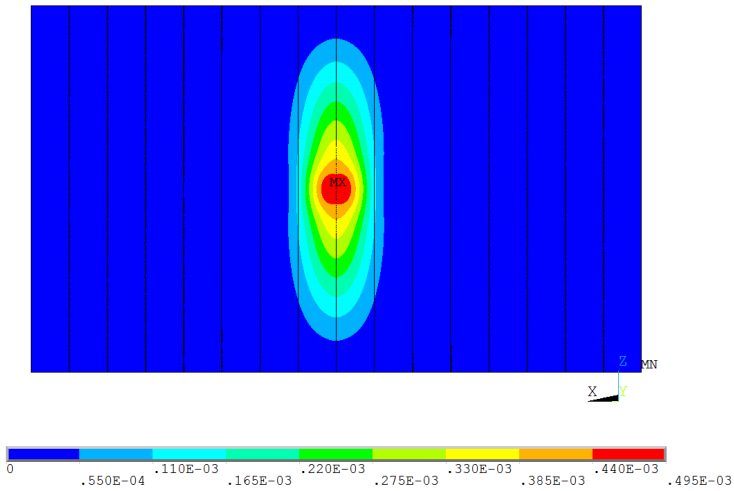


(a) Displacement vector sum in m.

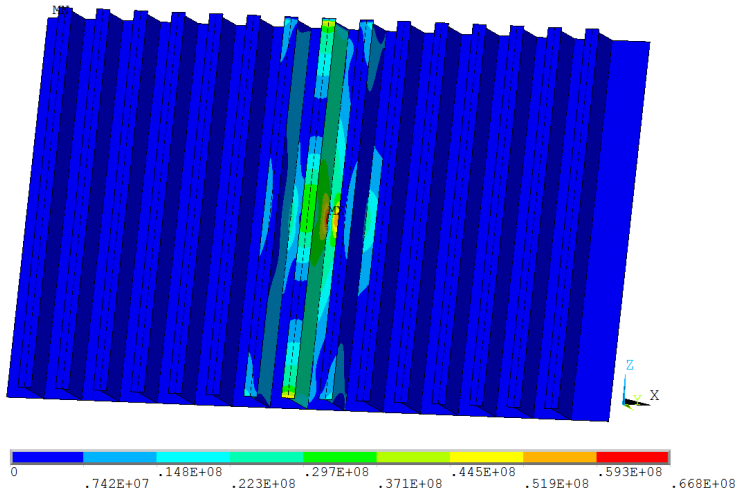


(b) Von Mises stress in Pa.

Figure 8.6: Bergy bit B09 loading applied to the second geometry with a mesh size of 15 mm.

# Chapter 9

# Results of Dynamic Loading

## 9.1 Second geometry

The time step size for the analysis was 3.9196e-6 s.

The impact simulation can be seen in Figure B.2 in the appendix. The elements of the ice feature eroded during the simulation. Eroded elements are represented by red dots in the figures. The first eroded elements appear in the results at time=0.025 s. The two elements that have eroded by this time are both at the tip of the ice feature. The erosion mainly happened at the elements closest to the plate as the ice feature approached the plate. The erosion was not uniform in the x-direction through the ice feature. The elements close to the centre eroded before the edges. This is shown by using a vertical section plane through the middle of the ice feature as shown in Figure 9.1a. The deformation at 0.1 s, which was the end time of the analysis, is shown in Figure 9.1b.

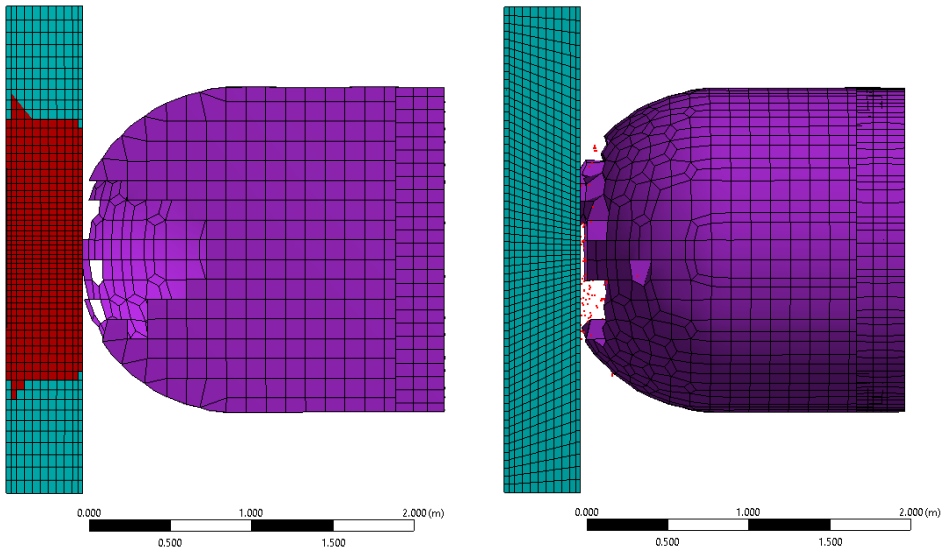


(a) Deformation at time=0.025 s. The model has been cut with a vertical section plane through the middle.

(b) Deformation at time=0.1 s.

Figure 9.1: Side view of impact analysis.

The velocity and acceleration in the y-direction for the rear face of the ice region was plotted over time in Figure 9.2. The velocity of the ice region starts at -3.00 m/s and ends at 0.15 m/s.

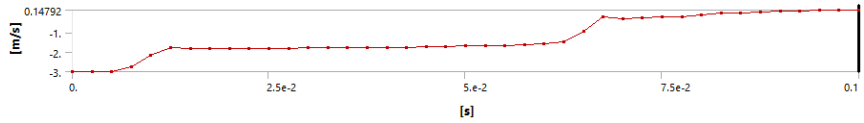


(a) Velocity in y-direction taken from the rear face of ice region.

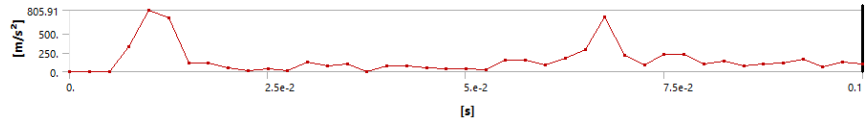


(b) Acceleration in y-direction taken from the rear face of ice region.

Figure 9.2: Velocity and acceleration of ice region taken from the rear face.

The velocity and acceleration in the y-direction for the disk was plotted over time in Figure 9.3.

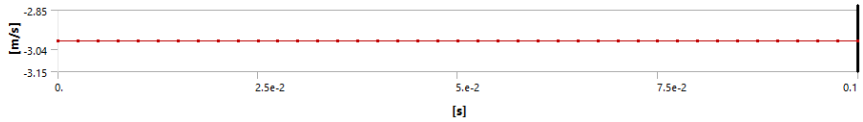


(a) Velocity in y-direction taken from the disk.

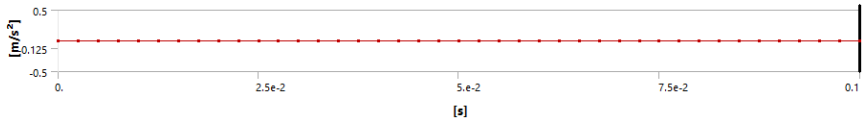


(b) Acceleration in y-direction taken from the disk.

Figure 9.3: Velocity and acceleration of disk.

The von Mises stress of the ice region over time is shown in Figure 9.4a. The peaks of high stress is followed by elements eroding and thereby reducing the stress in the intact ice material. The maximum von Mises stress appeared after 0.065 s and was 23.87 MPa. The stress in the ice at this time can be seen in Figure 9.4b.

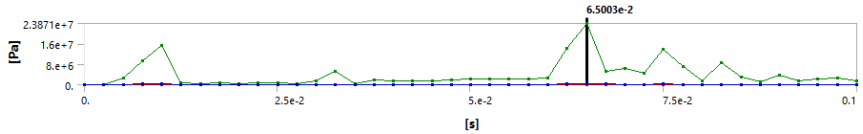


(a) Variation of von Mises stress over time. The green line represents the maximum value at the given time. The blue line shows the average value for the ice material and the red shows the minimum.

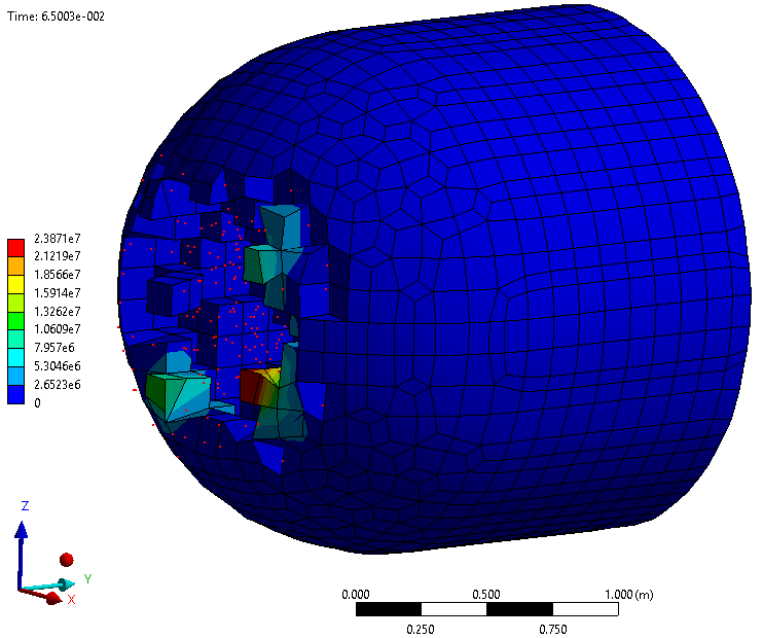


(b) Von Mises stress at time of maximum von Mises stress.

Figure 9.4: Von Mises stress for the ice feature. Stresses are shown in Pa.

The maximum principal stress over time is shown in Figure 9.5. Tension is shown as positive stresses and compression is shown as negative stresses.

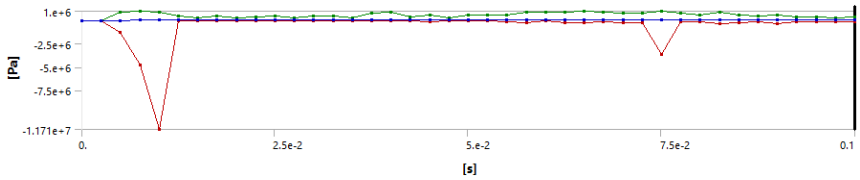


(a) Maximum principal stress in Pa over time.

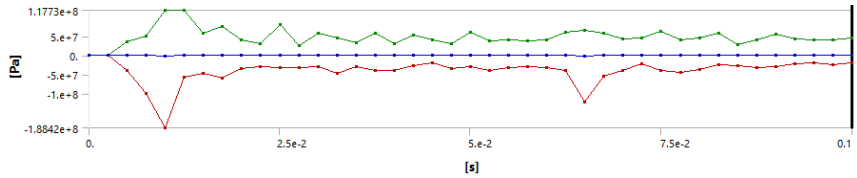


(b) Middle principal stress in Pa over time.

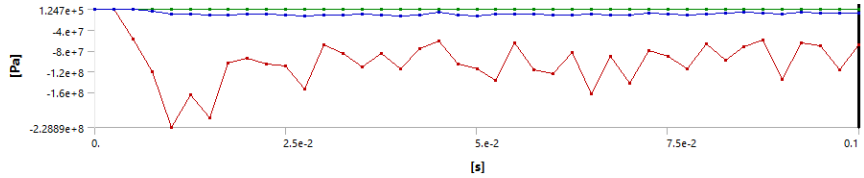


(c) Minimum principal stress in Pa over time.

Figure 9.5: Principle stresses in Pa over time for the ice region.

The maximum displacement of the plate was found after 1.0002e-2 s. The total deformation of the plate at this point in time can be seen in Figure 9.6. The largest displacement is located at the centre of the plate and is 2.8 mm.

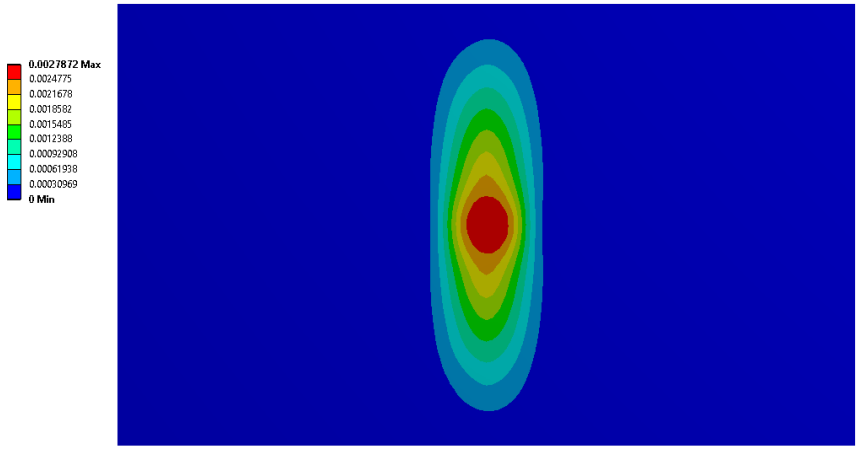


Figure 9.6: Deflection at time of max deflection for the second geometry. Time=1.0002e-2.

The deformation of the plate, excluding the stiffeners, over time is shown in Figure 9.7. The animated deformation of the plate over time showed the displacement moving away from the impact zone and bouncing like waves.

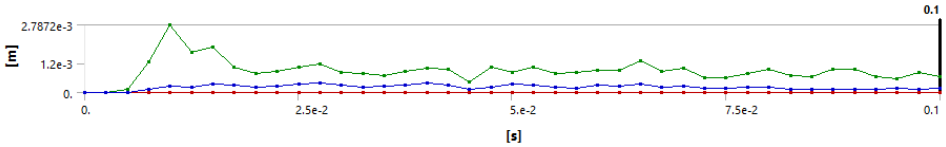


Figure 9.7: Deformation of the plate excluding stiffeners over time.

The stiffened plate has plastic strains in the centre stiffener and the plate at the end time. The plastic strain first appear at the ends of the central stiffener, in the upper part of the flange. This plastic section spreads and plastic strains close to the centre of the plate develops. The maximum plastic strain detected in the analysis was 0.0006.

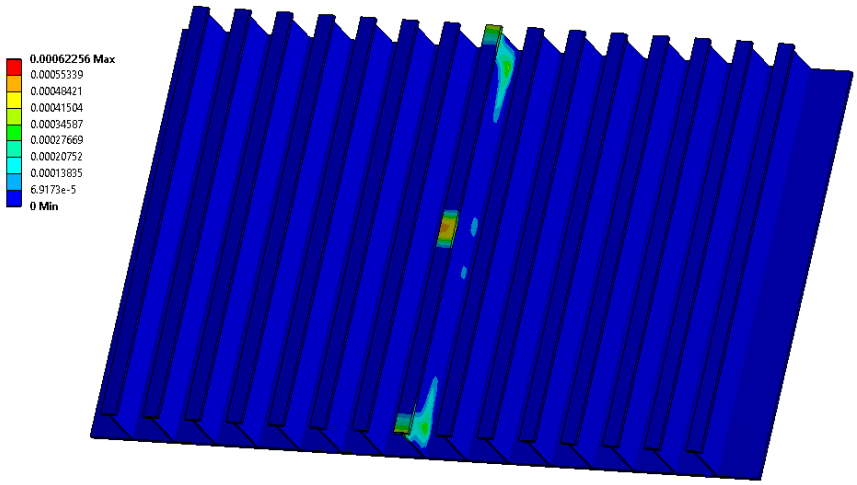


(a) View from inside of hull.

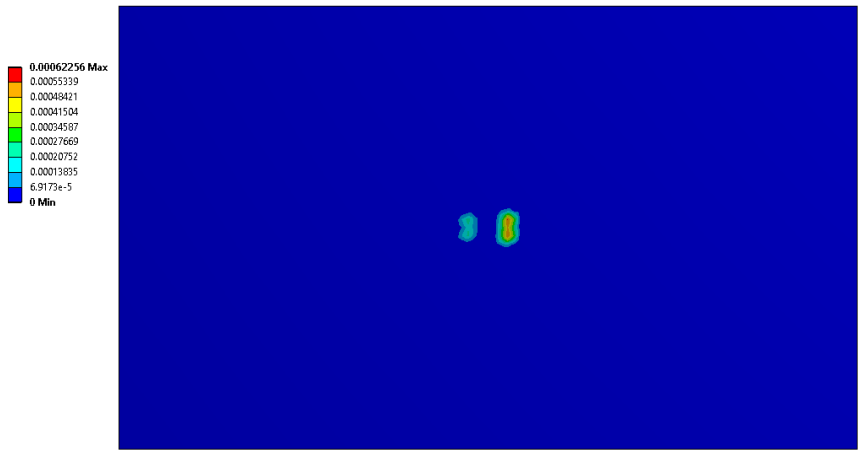


(b) View from outside of hull. The two plastic regions are located between the centre stiffener and the next stiffener on either side.

Figure 9.8: Plastic strain in the stiffened plate at end time=0.1 s.

The von Mises stress varies throughout the analysis. A time series showing this variation can be seen in Figure 9.9. The time of maximum von Mises stress was 1.0002e-2 s. The von Mises stress for this time has been plotted and the maximum von Mises stress is 207.6 MPa. The stress is the highest for the ends and middle of the centre stiffener. The stress is also large for the same regions in the plate where the plastic strain appeared. This can be seen in Figure B.3 in the appendix. The changing von Mises stress around the time of maximum stress is shown in Figure B.4 in the appendix.

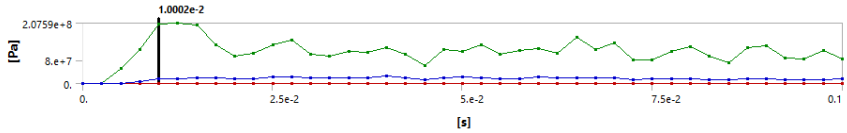


(a) Variation of von Mises stress over time. The green line represents the maximum value at the given time. The blue line shows the average value for the plate and the red shows the minimum.

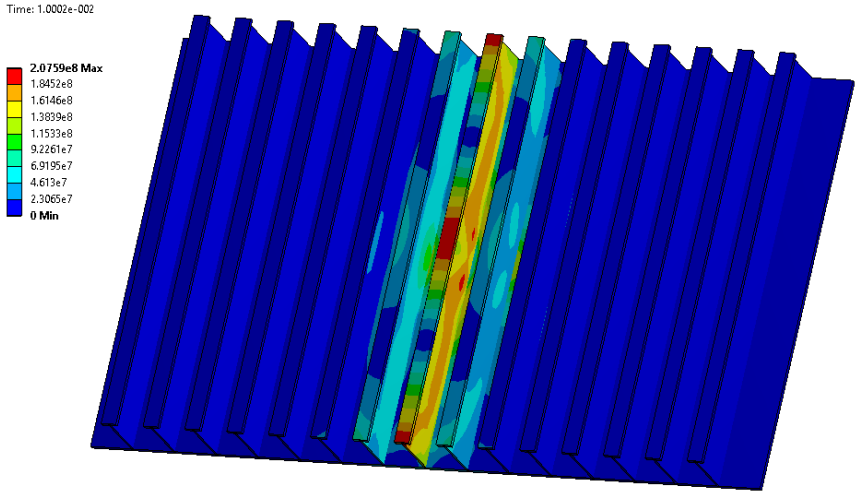


(b) Von Mises stress at time of maximum von Mises stress.

Figure 9.9: Von Mises stress for the plate. Stresses are shown in Pa.

# Chapter 10

# Discussion

## 10.1 Static Loading

The total force for the three load conditions are listed in Table 10.1. The IACS design load is 2.8 times higher than the highest load from the impact trials. If a structure is designed to resist the IACS design load then it could probably resist a growler impact as well. This assumption would also depend on hull shape, speed, impact region on the hull and more.

Table 10.1: Total load of static load conditions.

| Load condition | Force | |
|---|---|---|
| IACS design loading | 13.8 | MN |
| Bergy bit loading B14 | 5.0 | MN |
| Bergy bit loading B09 | 0.3 | MN |

### 10.1.1 IACS Design Loading

The first geometry showed excessive distortion for mesh sizes of 100 mm and lower. For global mesh sizes below 50 mm, no solution was produced for the first geometry with the IACS design load, as the solution did not converge. This could perhaps be solved by refining the mesh in some areas. Local refinement of the mesh was not attempted in this thesis. Reducing the global mesh size even further, and thus increasing the calculation time, was deemed too time consuming.

Another method that maybe could have made the solution converge was to reduce the time step size. This was attempted, but it did not solve the problem. Using the integrated ANSYS tool Stabilize was also attempted, but no reasonable

result was produced. Solving the model using the arc-length method up to 1 m of deflection, instead of the Newton-Raphson method, resulted in aborted analysis because the solution did not converge.

ANSYS applies loads gradually during the loadstep. The load increases gradually at each substep until the full load is applied at the final substep. Each substep has several iterations until the convergence criteria for that substep is fulfilled and the next substep can be calculated. Figure 8.1a shows the displacement in the y-direction for the centre of the plate. The full IACS design load is applied at time=1, when the loadstep ends. The displacement increases rapidly after time=0.4. It can be seen that the program was not able to find a converged solution after about time=0.8. This was at substep 52 and the run was terminated. Figure A.2b shows the cumulative iterations. More iterations were needed when the displacements became larger. This is a result of including nonlinear behaviour in the analysis.

The rotation about the y-axis can be seen in Figure A.3a. The large rotations are relatively local and close to the ends of the central stiffeners. The highest values are found in the web. A node close to the MIN in the figure was selected, and the rotation for this node was plotted over time. It can be seen in Figure A.3b that the rotation increases rapidly in magnitude before the termination time. This may indicate that the stiffeners buckles and cause the nonconvergence. The Newton-Raphson residuals were plotted when the solution did not converge. The plot indicates where the model is not satisfying equilibrium. Force and moment imbalances were plotted and can be seen in Figure A.4. The areas of high rotation about the y-axis were areas of high Newton-Raphson residuals. This may be because the stiffener web and/or flange buckles near the ends.

The analysis was also done using linear geometrical effects. This produced a displacement of 2 m. Nonlinear geometrical effects should be included for deformations of this size. If nonlinear geometry was accounted for, the stiffness of the system would increase as the deflection increases. The deflection would therefore be smaller, assuming no buckling occurred.

A reasonable result was not obtained for the first geometry with the IACS design load. The maximum pressure the structure can take for the given patch area is approximately 2.3 MPa. The behaviour up to this point was examined by applying fractions of the pressure to the IACS design loading patch. The results shown in Figure A.5 was obtained. The model is meshed with a mesh size of 50 mm. The plot shows that the displacement increases at a much higher rate than the pressure. The plot resembles a load-displacement curve nearing the ultimate load, when the displacement goes towards infinity if no failure criteria is given. The plot indicates that the structure is not capable of sustaining the IACS design pressure which is represented as a vertical line in the plot at 2.827 MPa. A warning of elements with excessive distortion is given for pressures 1.98 MPa and above. The solution did not converge for pressures of 2.26 MPa and above. Therefore no results can be

shown for the IACS design load applied to the first geometry with a mesh size of 50 mm.

The same fraction of pressure analysis was done with a mesh size of 15 mm. Two additional pressures were included on either side of the highest pressure that gave a converged solution in Figure A.5. This was done to better see the response near the maximum load that gave a converged solution. The results can be seen in Figure A.6. The warning of elements with excessive distortion was given for pressures 1.41 MPa and above. The last obtained solution was for a pressure of 2.12 MPa which gave a maximum displacement of 120 mm. The analysis for a pressure of 2.26 MPa was terminated as it exceeded the available disk memory. The solution did not converge for higher tested pressures. The mesh sizes of 50 mm and 15 mm gave similar displacements for the pressures. The stresses at the selected nodes seem to level out as the pressure increases. It can not be said from the results that a mesh size of 15 mm could sustain higher pressures than for 50 mm, as this additional loadstep of 2.12 MPa was not included in the analysis for 50 mm.

The second geometry handles the design pressure. The maximum displacement is 2.6 mm and the maximum von Mises stress is 213 MPa. The maximum von Mises total mechanical strain is 0.0028 and only the ends of the stiffeners near the boundary displays plastic strain as seen in Figure A.8. It is beneficial to the integrity of the ship hull if the stiffeners fail before the shell plating. This would prevent water from pouring in while the damage can be detected and repaired. Compared to the applied nonlinear material model, as seen in Figure 7.2, the stress is above the proportional limit, but below the yield point. The plastic strains displayed in Figure A.8b come from strains above the proportionality limit. If we assume that plastic behaviour starts at the yield point, the model would not have plastic deformation under this load, based on the von Mises stresses and strains. The boundary conditions are very strict and may also affect the high stresses near the boundary.

The highest normal stress is $\sigma_z$. This can be seen in Figure A.9. The pressure is applied to the outside of the plate and the load is transferred from the plate to the stiffeners, and then to the boundaries. The top of the stiffener is in tension and the bottom in compression as expected by the location of the load and the boundary conditions given.

The second geometry was dimensioned according to the IACS regulations and is therefore expected to support the IACS design load. The weaker plate did not meet the criteria for shear area and plastic section modulus according to the IACS regulations, and it was therefore expected to have larger displacements and plastic strains.

### 10.1.2 Bergy Bit Loading B14

The first geometry is capable of supporting the B14 load with plastic deformations. The maximum displacement is about 68 mm, and the maximum von Mises stress is 411 MPa as seen in Figure 8.3. This is above the yield point. The von Mises stress is highest within the vertical section with applied loading. This shows the stiffeners carry the loads to the boundaries. The stresses are largest at the stiffener next to the centre stiffener, at the flange boundary. The von Mises stress is also higher at the midspan of the stiffeners. This is in accordance with what was expected based on basic beam theory with an evenly distributed load at the midspan. It is also worth mentioning that $\sigma_z$ is quite large locally at the stiffener boundary. It has a maximum value of $\sigma_z = -464$ MPa. The fixed boundary condition is modelled as loads applied to the nodes along the edges of the model. The results in close proximity to loads may be unrealistic as stated by the St. Venant's principle. This may affect the maximum von Mises stress at the same location in Figure 8.3b.

The strains can be seen in Figure A.12. There are high values of plastic strain near the boundaries. The maximum is about 16 % and is located at the stiffener next to the centre stiffener, at the flange boundary. The plastic strains are present in other places in the model as well, such as the centre of the plate model. The load will therefore cause plastic deformations in the stiffeners at the point of impact and at the boundaries. No failure criteria was given for this model, but stains of 16 % are close to the failure strain for thin plates of normal strength steels according to IACS (2018). Softer boundary conditions could reduce the stress and strain at the ends of the stiffeners.

The normal stresses are shown in Figure A.13. $\sigma_x$ in the plate is high in the loaded area between the stiffeners. The maximum is 265 MPa while the second geometry has a maximum of 100 MPa for the same load. The second geometry has thicker shell plating and the stress will therefore be lower. The second geometry also has stronger stiffeners that transfer more of the load.

The maximum displacement of the second geometry is 2 mm. Compared to 68 mm for the first geometry, this a much lower. The maximum von Mises stress is also much lower for the second geometry. The plastic strain of the second geometry can be seen in Figure A.8b. There is only plastic deformation at the ends of the centre stiffeners for the second geometry.

The values used to represent the load from bergy bit B14 have been read from graphs which may lead to some inaccuracies. The bergy bits in the impact trial had been hit several times. The impacted ice is crushed during an impact. This will affect the impact loads for the following impacts if hit in the same area. It is not clear if or how this affected this impact load. The load pattern recorded is based on a numerical model divided into cells. The cells are assumed to have even pressure, but this is not the case in reality, only a simplification. Only cells

with a pressure measured to above 0.25 MPa was considered. This may lead to an underestimation of the load. The areas considered had to be contiguous. If the iceberg had a shape that resulted in several separate contact regions within the panel, or with the vessel outside the panel, the additional load would not be included in estimating the total load nor the total contact area. This would also make the given load an underestimation. The bergy bit impacts also took place under certain conditions. Sea state can affect relative velocity and large waves could result in an impact area not located at the design waterline of the ship. This could change the loads from the bergy bits.

### 10.1.3 Bergy Bit Loading B09

The load from bergy bit B09 did not produce von Mises stresses above the yield limit for the two plate geometries. The displacements were relatively small for both plates. The first geometry had a maximum displacement of almost 2 mm. This is not large compared to its plate thickness of 19 mm. The second geometry had a maximum displacement of 0.5 mm. None of the plates had plastic deformation under this load condition. There would therefore be no dent in the hull of the two assumed ships.

The applied load was taken from the same impact trial as for bergy bit B14 and the same uncertainties in reading the load for B14 applies to the load for B09.

### 10.1.4 Mesh size convergence

The loads were applied to the two geometries using various mesh sizes. This was done to ensure that the results were of adequate accuracy. A global parameter defined the mesh size for all elements used to mesh the two geometries. The response for some nodes of the plate, shown in Figure A.1, was collected for runs using the different mesh sizes. For all mesh sizes tested, global mesh size equal to 15 mm was seen as low enough to give adequate accuracy to the results.

The mesh size is of importance as a large mesh size may give the system too high stiffness. A large mesh size means that the elements are large and a realistic smaller deformation pattern may not be captured in the analysis. This can result in failures and singularities not being discovered. The mesh sizes tested in the analyses ranged from 300 mm to 10 mm.

This may not have been small enough, especially for the first geometry with high loads. Figure A.11b shows the von Mises stress at selected nodes for the first geometry exposed to bergy bit B14 loading. The stresses appear to even out for smaller mesh sizes, indicating that the adequate mesh size has been reached. However, the von Mises stress for Node 3 can be seen to dip from mesh size 15 mm to 10 mm. The location of node 3 is very close to the boundary of the load patch seen

in Figure 7.4. Node 3 is taken as the node closest to a defined coordinate shown in Figure A.1. The exact location of Node 3 therefore varies some for each mesh size. The dip in the graph may come as a result of this. The pressure in the patch is applied as forces to the nodes, so there may be some irregularities for the nodes at the edges of the load patch. The same dip can be seen for the second geometry as well in Figure A.15b.

## 10.2 Dynamic Loading

### 10.2.1 Second Geometry

The time plots have a relatively large distance between each plotted value. The behaviour of the stiffened plate can be difficult to read from some of the plots. There is also a chance that the maximum value of a graph is between the sampled values. This makes the maximum displacements and stresses stated in the results a minimum value of the maximum, meaning that the maximum displacements and stresses are at least as high as stated. Results are written to a result file frequently during the analysis. This file is then used to display the results in the post processor. By increasing the number of points in time written to the file, the time plots and graphs could have been improved.

#### Ice Feature

Figure 9.2 shows that the back of the ice region has a reduction in velocity over time. The ice feature was expected to slow down as kinetic energy of the ice was transformed into potential energy as deformations to the ice and plate. The plot showing the acceleration shows that there are two times during the time series where the velocity changes the most. These times are around time = 1.00e-2 s and 6.75e-2 s. The plot for acceleration has its peaks around the same time as the maximum von Mises stresses in Figure 9.4b. This is as expected because both the acceleration and loads of the ice region are dependant on the contact forces.

From Figure 9.3 it can be seen that the disk moves forward with the initial velocity throughout the simulation with no sign of acceleration in either direction. The movement of the disk over time can be seen in Figure B.2. It seems like the disk is not properly connected to the ice feature. A warning was given by the program during the analysis. It stated that the there are bonded connection(s) where the nodes didn't find a target face and that this could result in non-bonded nodes. It seems like this resulted in no connection between the ice region and the disk. This would explain why the disk seemed to move through the ice region and keep its initial velocity through the simulation.

The energy summary of the simulation can be seen in B.1. The plot includes the energy for the system as a whole. This plot was not as expected. A noticeable reduction of kinetic energy or increase in the internal energy was expected. The disk is heavy and has a high kinetic energy. The mass of the ice region is about 4700 kg and the disk is 1 906 000 kg. If kinetic energy is calculated as $1/2 \cdot m \cdot v^2$, the kinetic energy of the disk is 406 times higher than the ice region. This means that it is not possible to see the changing energy in the system due to only the ice region impacting the plate.

The ice region and the disk was meshed using the same procedure, but because of the different geometry, the meshes had some differences. It is unsure if this connection problem is due to the mesh or the settings used in defining the bonded contact.

It was concluded that the disk was not properly connected to the ice region and was not affecting the results shown, except for the energy plot. This means that the simulation showed an ice feature of 4700 kg impacting the plate. Smaller ice masses can come to a stop and bounce back as was mentioned in the theory of this thesis. The velocity at 0.1 s was positive for the back of the ice region. This may indicate that the ice region had bounced back and would have continued to move away from the plate.

The mesh of the ice was done using a Cartesian mesh. This method may not have been the best suited, but some other methods resulted in very small elements and others used elements that could not handle the crushable foam material. The Cartesian mesh method was therefore used. A study of how the element size affected the results should have been done by testing for smaller elements similar to what was done in the mesh convergence study for the static loads. This could have resulted in a more even erosion of the elements over time and a more continuous contact load.

It would have been interesting to compare the pressure from the static loads described in section 7.2 with the pressure at the contact region of the simulation. It was not possible to plot the pressure from the contact region in the program. This could have been done using ANSYS ACT where it is possible to use or write customised subprograms to visualise the contact pressure. This was deemed too complex and time consuming for this thesis.

The von Mises stress in the ice region is shown in Figure 9.4. The maximum von Mises stress was 23.87 MPa which is lower than the maximum stress allowed for the ice material. The maximum principal stress allowed was set to 50 MPa. This difference may be due to high stresses in one direction which would erode the material.

In order to simulate the damage caused by an impact with an ice feature con-

servatively, the ice load should be overestimated rather than underestimated. A stronger ice material could have resulted in higher impact loads and would have been a more conservative option when assessing the structural response and damage to the plate.

### Stiffened Plate

The deformation in the plate connected to Figure 9.7 was as expected for an impact load. The oscillating behaviour of the plate was animated and was similar to the response of impulse loads described in section 5.4.1.

The maximum displacement for the dynamic analysis was 2.8 mm. The static analysis for bergy bit B14 loading gave a maximum displacement of 2.0 mm. The dynamic loading produced a maximum deflection 1.4 times the displacement of the static loading. That these two results are in such agreement was somewhat surprising given the problems with the impact model.

The loads on the plate produced plastic strains as seen in Figure 9.8. The maximum value was 1.16 times higher than for the static bergy bit B14 load. The plastic region was also larger for this simulation and plastic strains developed in the plate and centre of the stiffener as well.

The von Mises stress showed similar fluctuations as the displacements following the peak stress and after the series in Figure B.4. This was as expected because stress waves were included in the model. The waves appeared to be reflected by the edges of the plate model. These fluctuations were difficult to follow because few points in time could be plotted from the result file. The modelled plate was supposed to be a cut-out of a larger bow section. The boundary conditions were fixed and could have resulted in unrealistic stress waves in the model. The response of the plate depends on the boundary conditions set, and softer boundary conditions could have been tested to better understand its influence on the results.

The maximum von Mises stress was only a little higher for this impact compared to the result from static bergy bit B14 loading. The effect of strain rate on the stress-strain curve was not defined for the steel material. This could have been included and would have raised the yield point for high stress rates. This could have resulted in a smaller plastic region.

# Chapter 11

# Conclusion

This thesis has presented topics related to ice loads on ship hulls with focus on accidental growler and bergy bit impacts. These ice features can be difficult to detect for a ship in transit through the Northern Sea Route. A stiffened plate with two different strengths and dimensions were exposed to ice loads using two different approaches.

Relevant theory has been presented to better understand the behaviours of stiffened plates made of steel and ice features during impacts. Material properties of steel used in this thesis was presented. The behaviour of ice during failure focused on crushing and bending failures. Crushing of the ice is the most important failure mode when assessing bergy bit impacts.

Ice is a complex material and several numerical models have been proposed but a single model has not been agreed upon. Two different numerical models were presented in this thesis, one model using a crushable foam and another using a Tsai-Wu yield surface to define plasticity.

The plate structure was assumed to be part of the bow of a ship classified as PC 7. The plate was modelled using two different scantlings, or geometries. The first geometry was a relatively weak plate not complying with the IACS polar class regulations. The second geometry was scaled up to comply with these regulations and resulted in a stronger plate.

The plates were exposed to three different pressure patches in a static analysis. The pressure patches were the design ice load for classification PC 7, and two impact loads from an impact trial with bergy bits. The first geometry showed signs that an accidental bergy bit impact could result in serious damage while the second geometry did not.

The first geometry failed under the design ice load and showed large rotation out of plane in the stiffener webs. Load from the larger bergy bit resulted in plastic strains that were relatively large and nearing the plastic strain limit of the material. Load from the smaller bergy bit resulted in small deformations and no plastic strains.

The second geometry did not have large deformations for any of the static loads applied. The design load and larger bergy bit load resulted in small plastic strains in the stiffeners near the boundary of the plate. No plastic strains were produced for the smaller bergy bit load.

A simulation of an impact between the second geometry and an ice feature similar to the larger bergy bit was attempted. Problems in modelling the ice feature as a crushable foam resulted in inconclusive results. The response of the plate was similar in magnitude to that of the larger bergy bit static load. No critical failure of the plate was detected.

# Chapter 12

# Further Work

The geometrical model could be taken from a real cargo ship with ice class equivalent to PC 7. The model could then include a larger section of the bow. The overall classification requirement is that the design ice load can be supported by the structure. Such a model would show how the regulations are actually being used for cargo ship design and a more definitive conclusion can be taken on the danger of bergy bit or growler impacts.

The effect of water could be included. It would be interesting to analyse impacts in different sea states, especially for rougher seas when both the ship the ice feature are moving.

Articles describing ice impact often use the program LS-DYNA. This may be a more suitable program for the integrated impact analysis, as some ice materials were developed using this program.

A parameter study could be done with different numerical ice models, impact angles, speeds, mass, shape and mesh size etc. The boundary conditions for the plate in this thesis are strict. Softer boundary conditions could be tested.

The pressure at the contact region in the integrated analysis could be plotted and compared with the load from the static analysis of bergy bit B14.

# Reference list


ANSYS (2019a). *ANSYS Mechanical Application 19.2. Mechanical APDL 19.2. Theory Reference.*

– (2019b) Chapter 3: Loading. *ANSYS Mechanical Application 19.2. Mechanical APDL Basic Analysis Guide.*

– (2019c) Explicit Dynamics Analysis Guide. *ANSYS Mechanical Application 19.2.*

Bridges, R. et al. (2018) A study on the specification of minimum design air temperature for ships and offshore structures. *Ocean Engineering*, 160, pp. 478–489. DOI: 10.1016/j.oceaneng.2018.04.040.

Canadian Coast Guard (2019) Chapter 5 Ship Design and Construction for Ice Operations. *Ice Navigation in Canadian Waters.*

DNV (2013) DNV-RP-C208: Determination of Structural Capacity by Non-linear FE analysis Methods.

DNV GL (2018) Chapter 6 Cold climate. *DNV GL rules for classification: Ships (RU-SHIP), Part 6 Additional class notations.*

Frederking, R. and Shkhinek, K. (2014) Ice Loads On Structures. *Cold Regions Science and Marine Technology, Encyclopedia of Life Support Systems (EOLSS).*

FSICR (2017a) Finnish ice classes equivalent to class notations of recognized classification societies and the determination of the ice classes of ships. Finnish Transport Safety Agency.

– (2017b) Ice Class Regulations and the Application Thereof. Finnish Transport Safety Agency.

Gagnon, R. (2008) Analysis of data from bergy bit impacts using a novel hull-mounted external Impact Panel. *Cold Regions Science and Technology*, 52.1, pp. 50–66. DOI: 10.1016/j.coldregions.2007.04.018.

Gagnon, R. (2007) Results of numerical simulations of growler impact tests. *Cold Regions Science and Technology*, 49.3, pp. 206–214. DOI: 10.1016/j.coldregions.2007.03.016.

– (2011) A numerical model of ice crushing using a foam analogue. *Cold Regions Science and Technology*, 65.3, pp. 335–350. DOI: 10.1016/j.coldregions.2010.11.004.

Gagnon, R. et al. (2008) Overview accompaniment for papers on the bergy bit impact trials. *Cold Regions Science and Technology*, 52.1, pp. 1–6. DOI: 10.1016/j.coldregions.2007.04.015.

Høyland, K. (n.d.) AT-334 Arctic Marine Measurements Techniques, Operations and Transport Module I Sea ice features and properties.

IACS (2016) UR I - Polar Class. International Association of Classification Societies.

– (2018) UR W - Materials and Welding. International Association of Classification Societies.

ISO (2010) Petroleum and natural gas industries - Arctic offshore structures. ISO 19906:2010. International Organization for Standardization.

Jordaan, I. J. (2001) Mechanics of ice–structure interaction. *Engineering Fracture Mechanics*, 68.17, pp. 1923–1960. DOI: 10.1016/S0013-7944(01)00032-7.

Kujala, P. and Ehlers, S. (2013) Limit State Identification for Ice-Strengthened Hull Structures Using Measured Long-Term Loads. *Proceedings of the 22nd International Conference on Port and Ocean Engineering under Arctic Conditions*. Espoo, Finland, p. 10.

Langen, I. and Sigbjörnsson, R. (1979) *Dynamisk analyse av konstruksjoner (Dynamic Analysis of Marine Structures)*. Trondheim: Tapir.

Larsen, C. M. (2014) *Marine Dynamics*. Department of Marine Technology, Norwegian University of Science and Technology.

Lee, S.-G. and Nguyen, H.-A. (2011) LNGC Collision Response Analysis with Iceberg Considering Surrounding Seawater. *Proceedings of the Twenty-first (2011) International Offshore and Polar Engineering Conference (ISOPE)*. Maui, Hawaii, USA.

Leira, B. J. (2014) *Marine Structures Basic Course*. Department of Marine Technology, Norwegian University of Science and Technology.

Liu, Z., Amdahl, J., and Løset, S. (2011) Plasticity based material modelling of ice and its application to ship–iceberg impacts. *Cold Regions Science and Technology*, 65.3, pp. 326–334. DOI: 10.1016/j.coldregions.2010.10.005.

Moan, T. (2003) *Finite Element Modelling and Analysis of Marine Structures (including chapter 12)*. Department of Marine Technology, Norwegian University of Science and Technology.

Mork, H. (2016) Ultimate Strength and Capacity Assessment of Ice Class Vessel Operating in Ice. Master Thesis. Trondheim, Norway: Norwegian University of Science and Technology. Department of Marine Technology.

NSRA (2017) *Rules of navigation in the water area of the Northern Sea Route approved by the order of the Ministry of Transport of the Russian Federation dated January 17, 2013, No. 7. Including amendments of January 9, 2017.*

Polar Code (2015) International Code for Ships Operating in Polar Waters (Polar Code), MEPC 68/21/Add.1 Annex 10. Marine Environment Protection Committee.

Ralph, F., McKenna, R., and Gagnon, R. (2008) Iceberg characterization for the bergy bit impact study. *Cold Regions Science and Technology*, 52.1, pp. 7–28. DOI: 10.1016/j.coldregions.2007.04.016.

Riska, K. and Bridges, R. (2019) Limit state design and methodologies in ice class rules for ships and standards for Arctic offshore structures. *Marine Structures*, 63, pp. 462–479. DOI: 10.1016/j.marstruc.2017.09.005.

Ritch, R. et al. (2008) Local ice pressures measured on a strain gauge panel during the CCGS Terry Fox bergy bit impact study. *Cold Regions Science and Technology*, 52.1, pp. 29–49. DOI: 10.1016/j.coldregions.2007.04.017.

Song, M., Kim, E., and Amdahl, J. (2015) FLUID-STRUCTURE-INTERACTION ANALYSIS OF AN ICE BLOCK-STRUCTURE COLLISION. *Proceedings of the 23rd International Conference on Port and Ocean Engineering under Arctic Conditions*. Trondheim, Norway, p. 12.

Storheim, M. (2016) Structural Response in Ship-Platform and Ship-Ice Collisions. Doctoral theses at NTNU, 2016:14. Trondheim, Norway: Norwegian University of Science and Technology.

Timco, G. and Weeks, W. (2010) A review of the engineering properties of sea ice. *Cold Regions Science and Technology*, 60.2, pp. 107–129. DOI: 10.1016/j.coldregions.2009.10.003.

WMO (2014) WMO Sea Ice Nomenclature, volumes I, II and III. WMO No. 259. 5th Session of JCOMM Expert Team on Sea Ice. World Meteorological Organization.

World Maritime News (2018) Venta Maersk Makes History as It Crosses Northern Sea Route. World Maritime News. URL: https://worldmaritimenews.com/archives/260865/venta-maersk-makes-history-as-it-crosses-northern-sea-route/.

# Appendix A

# Additional Results - Static Loading

The nodes used in the convergence plots are defined as follows:
Node 1: Between stiffener 7 and 8, middle of height, centre of plate thickness.
Node 2: Between stiffener 6 and 7, middle of height, centre of plate thickness.
Node 3: Between stiffener 5 and 6, middle of height, centre of plate thickness.
Node 4: Between stiffener 7 and 8, quarter of height, centre of plate thickness.
Node 5: At stiffener 8, middle of height, centre of flange thickness.
Node 6: At stiffener 8, quarter of height, centre of flange thickness.
Node 7: At stiffener 7, height equal to web height, centre of flange thickness.

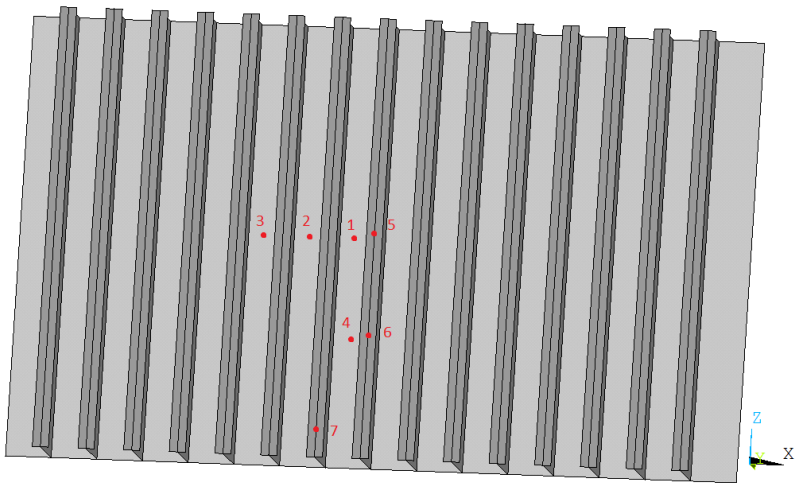


Figure A.1: Nodes used in convergence plots.

## A.1 IACS Design Loading - First Geometry

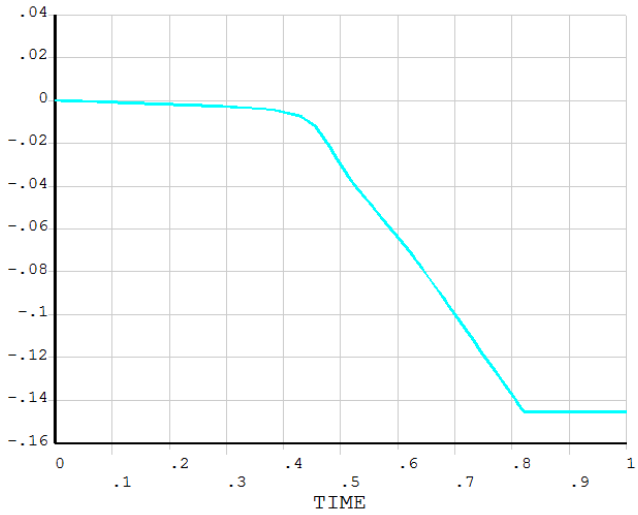


(a) Displacement in m in y-direction at centre of plate over time.

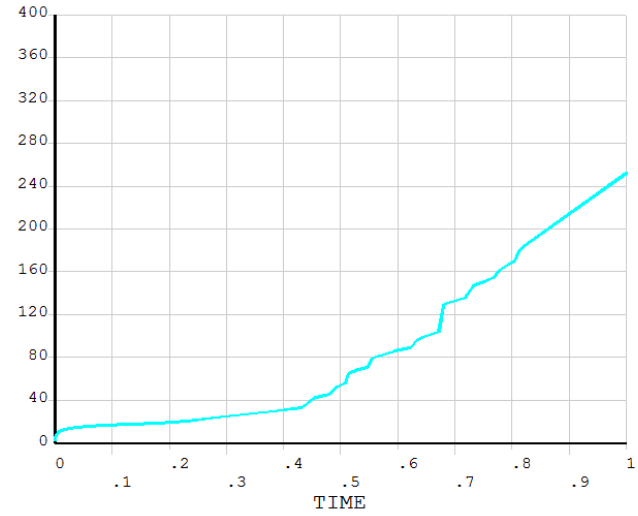


(b) Cumulative iterations.

Figure A.2: IACS Design loading applied to the first geometry with a mesh size of 15 mm.

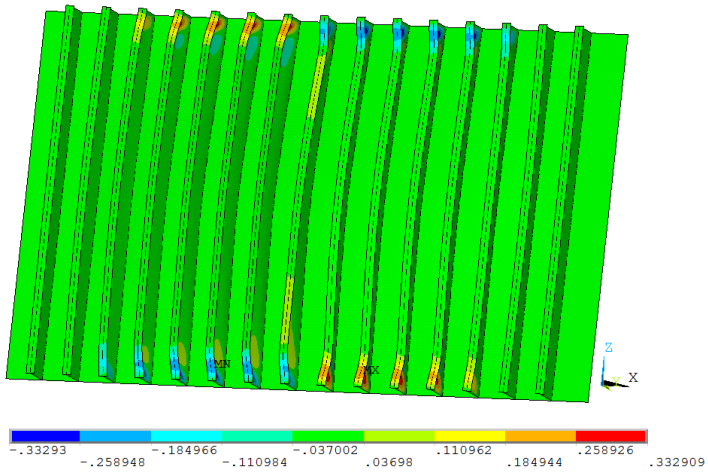


(a) Rotation about y-axis.

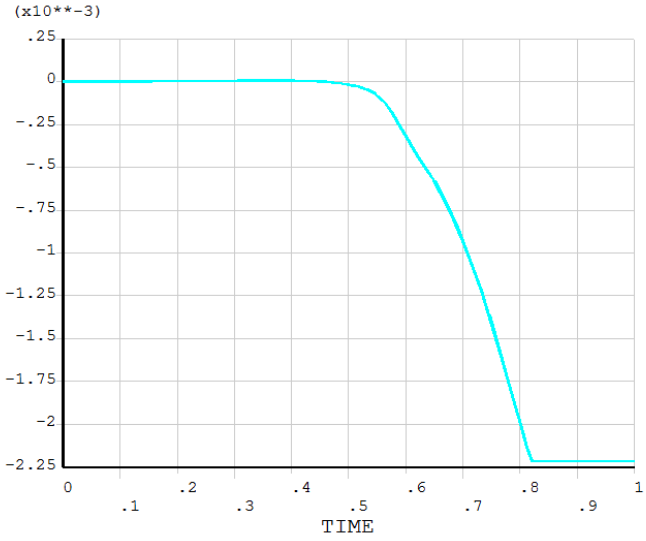


(b) Rotation about y-axis at node close to MIN in figure above.

Figure A.3: IACS design loading applied to the first geometry with a mesh size of 15 mm.

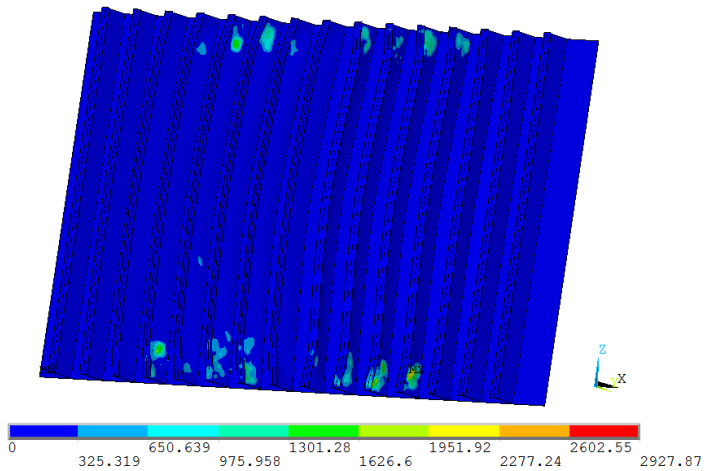


(a) Force imbalance. Computed as the square root of the sum of the squares of the residual component forces FX,FY and FZ.

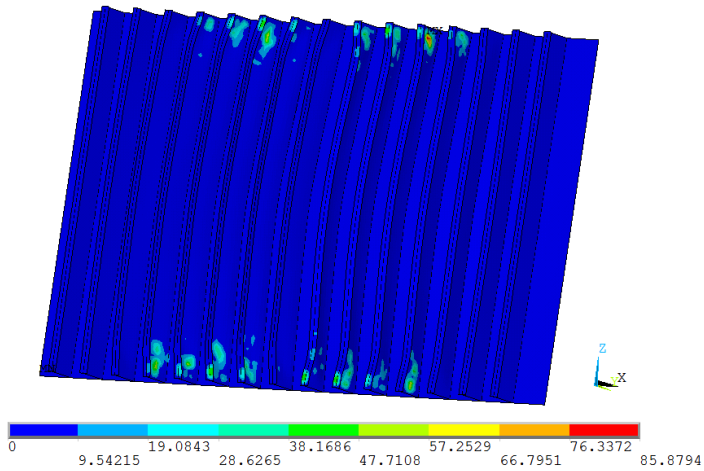


(b) Moment imbalance. Computed as the square root of the sum of the squares of the residual component moments MX,MY and MZ.

Figure A.4: Newton-Raphson residuals for substep 43, equilibrium iteration 16 (last computed). IACS design loading with mesh size of 50 mm.

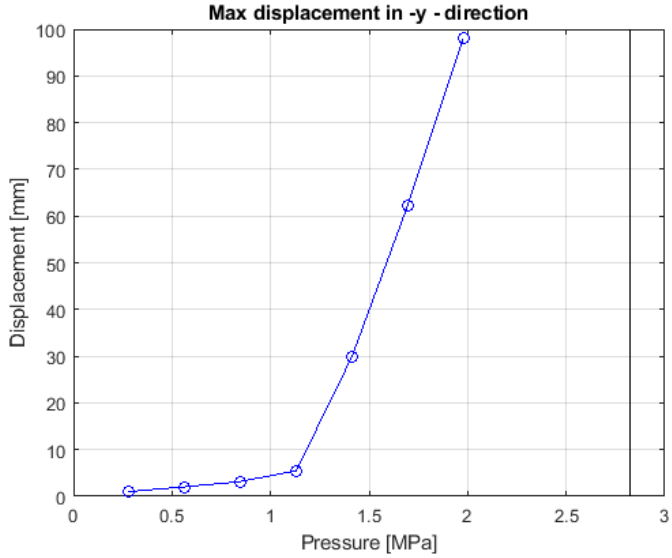


(a) Maximum displacement in y-direction for different pressures.

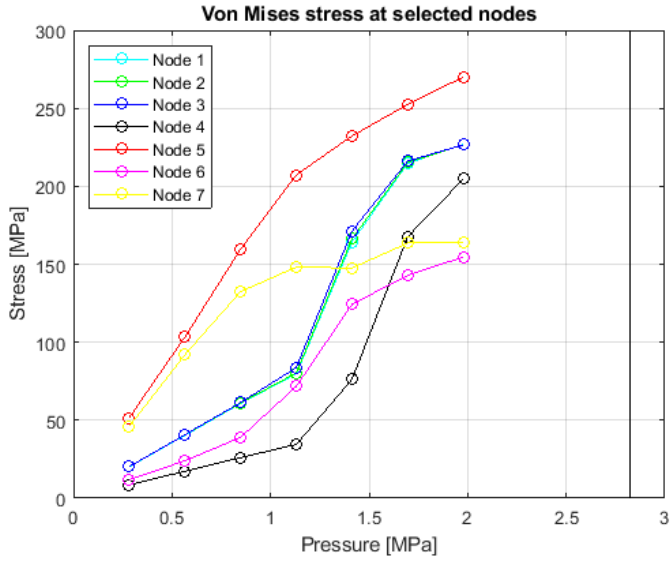


(b) Von Mises stresses at a selection of nodes for different pressures.

Figure A.5: Results for different pressures for the first geometry with a mesh size of 50 mm. The pressure is applied to the IACS design loading patch. The black line represents the magnitude of the IACS design load pressure. There were no solution for pressures above 2 MPa.

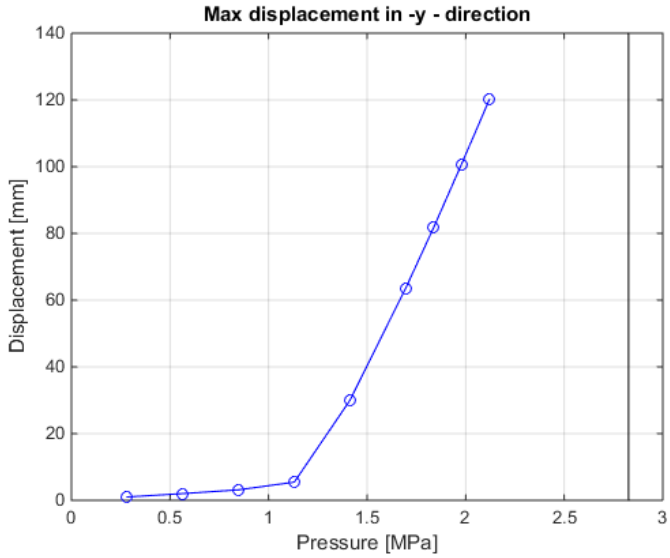


(a) Maximum displacement in y-direction for different pressures.

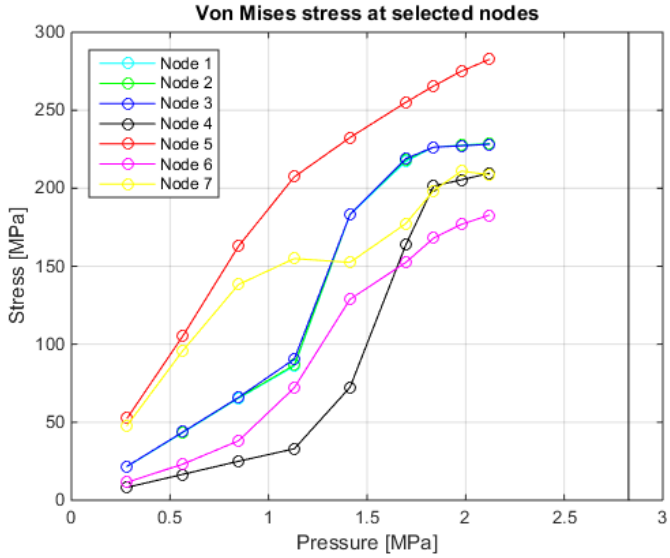


(b) Von Mises stresses at a selection of nodes for different pressures.

Figure A.6: Results for different pressures for the first geometry with a mesh size of 15 mm. The pressure is applied to the IACS design loading patch. The black line represents the magnitude of the IACS design load pressure. There were no solution for pressures above 2.1 MPa.

## A.2 IACS Design Loading - Second Geometry

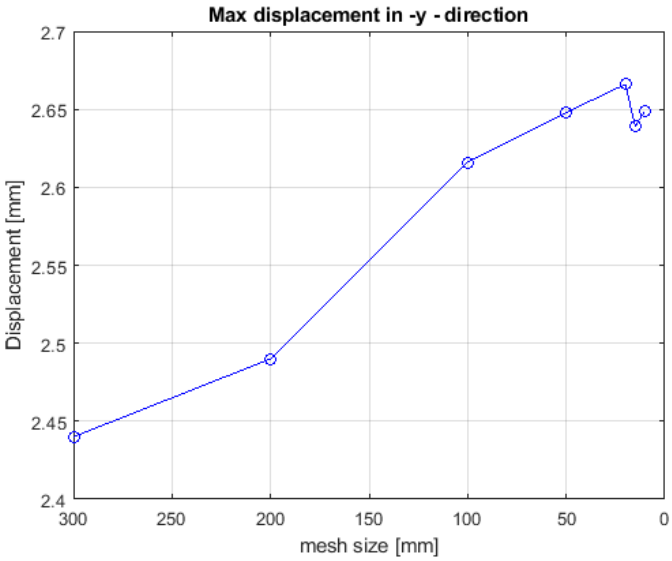


(a) Maximum displacement for different mesh sizes.

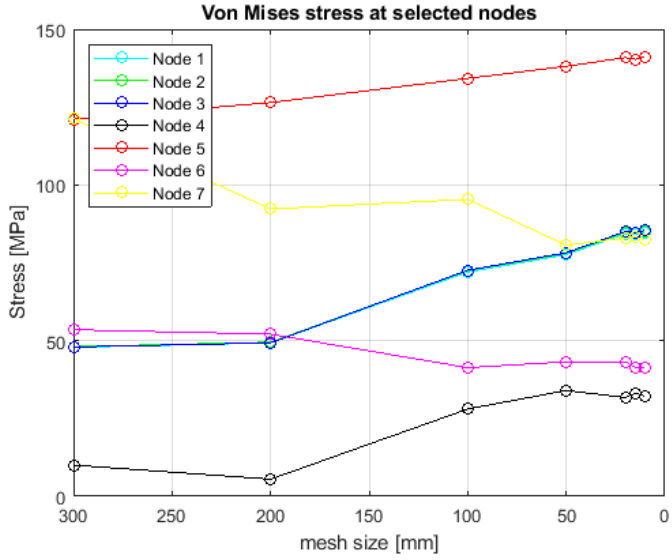


(b) Von Mises stresses at a selection of nodes for different mesh sizes.

Figure A.7: Convergence of results for the second geometry under IACS design loading.

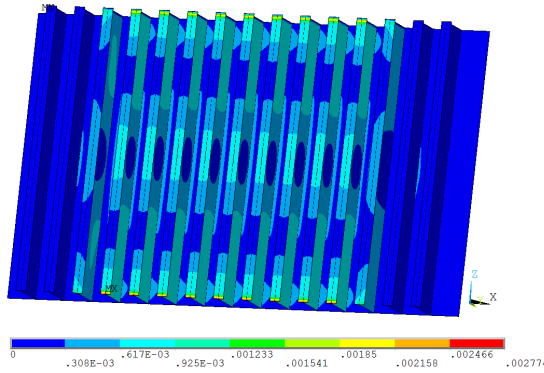


(a) Von Mises total mechanical strain.

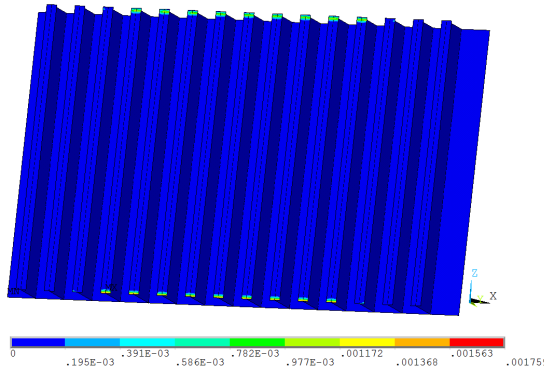


(b) Von Mises plastic strain.

Figure A.8: Von Mises strain. IACS Design loading applied to the second geometry with a mesh size of 15 mm.

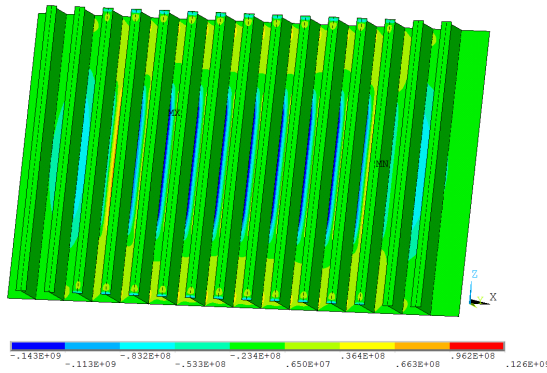


(a) Normal stress in x-direction.

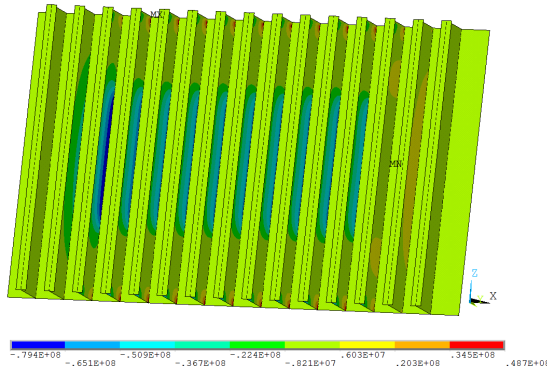


(b) Normal stress in y-direction.

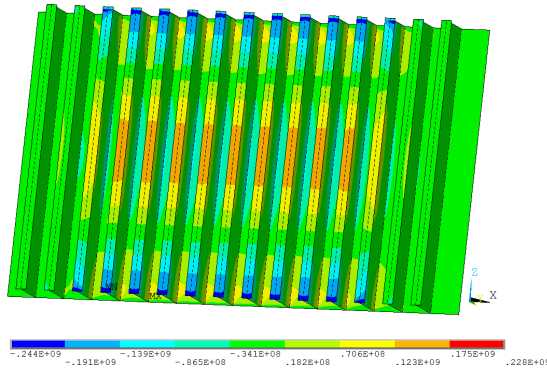


(c) Normal stress in z-direction.

Figure A.9: Normal stresses. IACS Design loading applied to the second geometry with a mesh size of 15 mm.

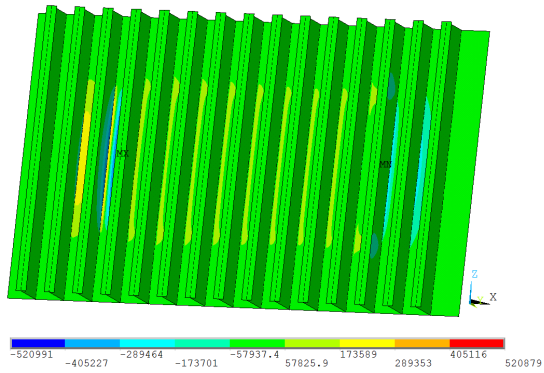


(a) Shear stress in plane normal to x-axis, y-direction. $\sigma_{XY}$.

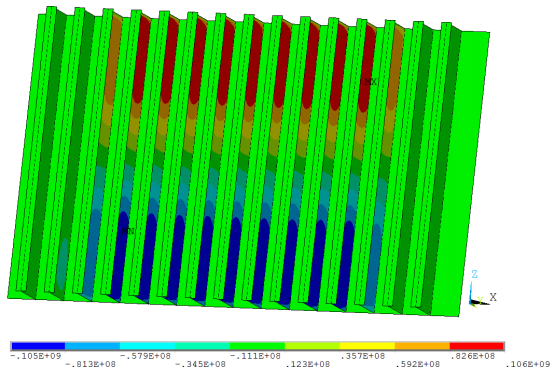


(b) Shear stress in plane normal to y-axis, z-direction. $\sigma_{YZ}$.

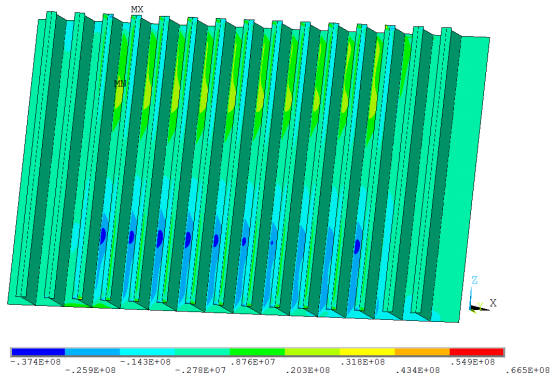


(c) Shear stress in plane normal to x-axis, z-direction. $\sigma_{XZ}$.

Figure A.10: Shear stresses. IACS Design loading applied to the second geometry with a mesh size of 15 mm.

## A.3 Bergy bit B14 Loading - First Geometry

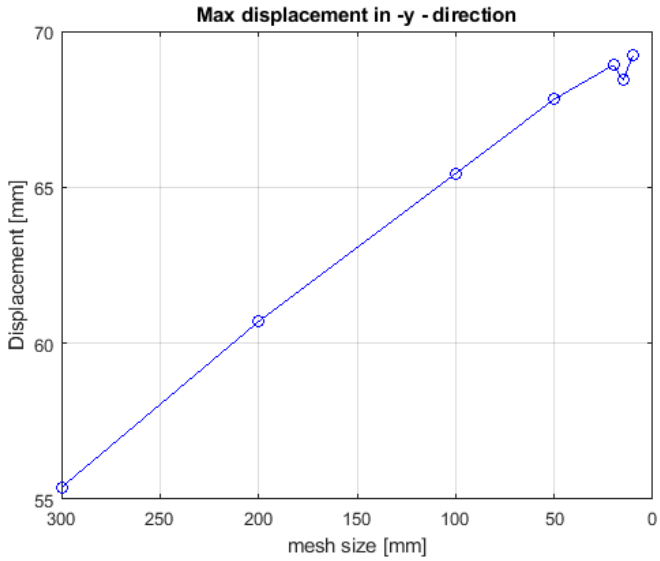


(a) Maximum displacement for different mesh sizes.

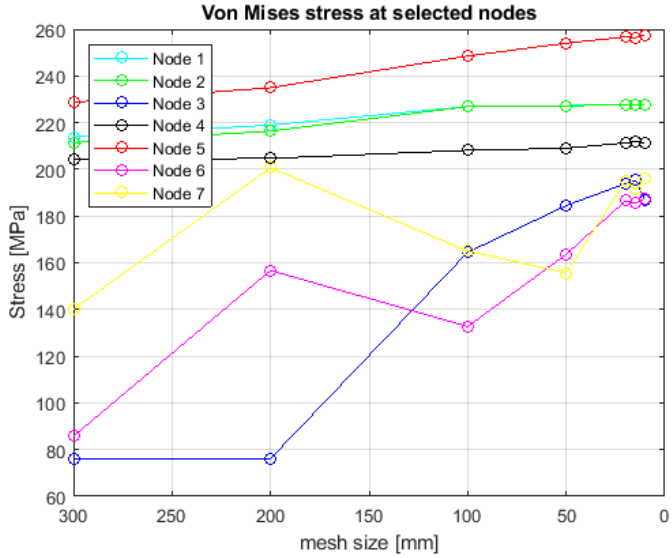


(b) Von Mises stresses at a selection of nodes for different mesh sizes.

Figure A.11: Convergence of results for the first geometry under bergy bit B14 loading.

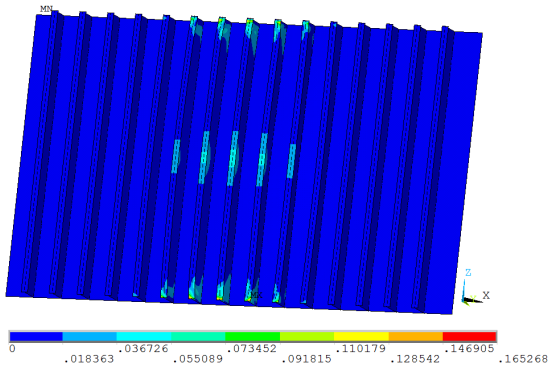


(a) Von Mises total mechanical strain.

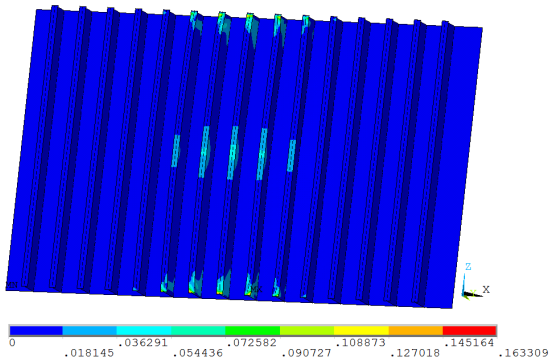


(b) Von Mises plastic strain.

Figure A.12: Von Mises strain. Bergy bit B14 loading applied to the first geometry with a mesh size of 15 mm.

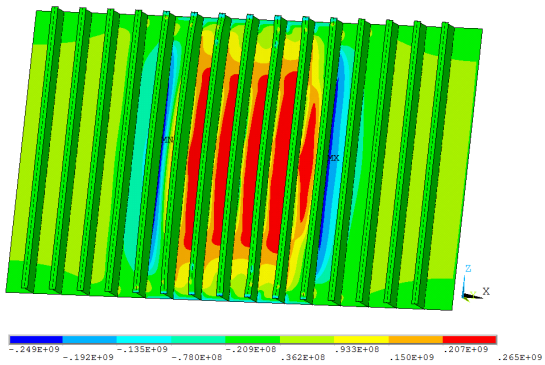


(a) Normal stress in x-direction.

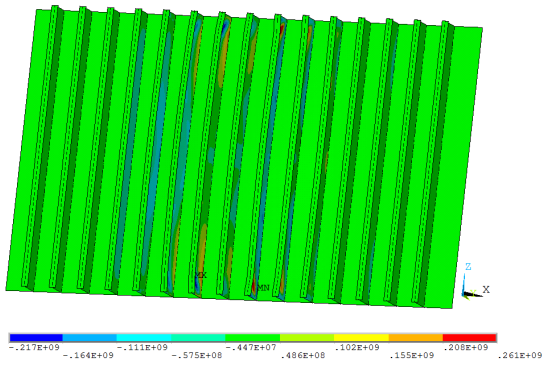


(b) Normal stress in y-direction.

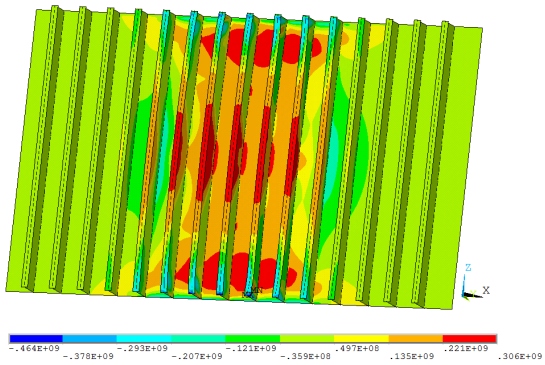


(c) Normal stress in z-direction.

Figure A.13: Normal stresses. Bergy bit B14 loading applied to the first geometry with a mesh size of 15 mm.

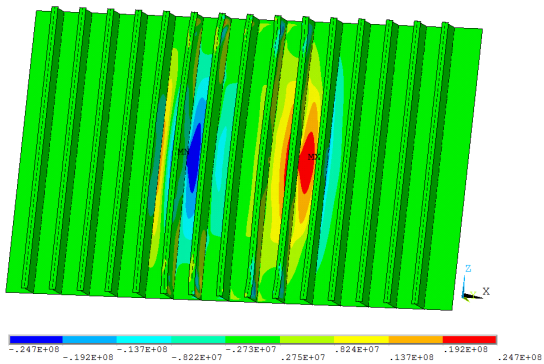


(a) Shear stress in plane normal to x-axis, y-direction. $\sigma_{XY}$.

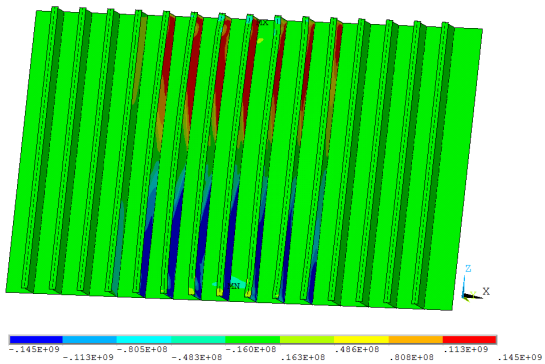


(b) Shear stress in plane normal to y-axis, z-direction. $\sigma_{YZ}$.

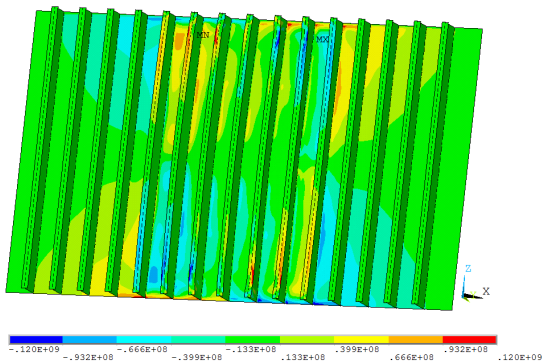


(c) Shear stress in plane normal to x-axis, z-direction. $\sigma_{XZ}$.

Figure A.14: Shear stresses. Bergy bit B14 loading applied to the first geometry with a mesh size of 15 mm.

## A.4 Bergy bit B14 Loading - Second Geometry

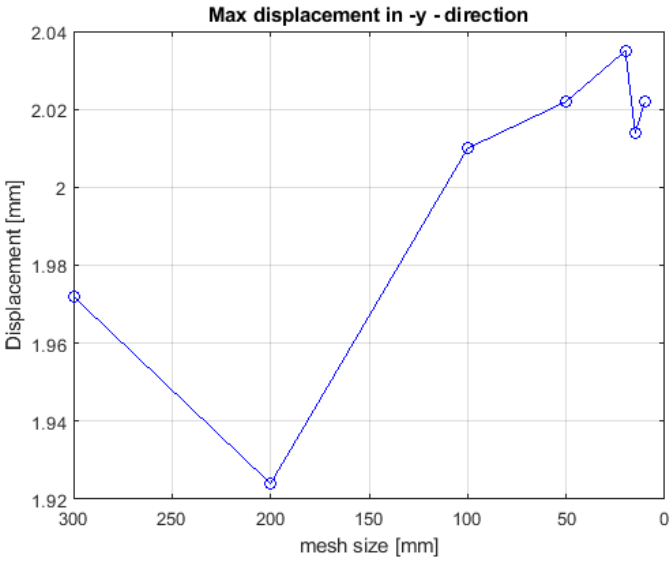


(a) Maximum displacement for different mesh sizes.

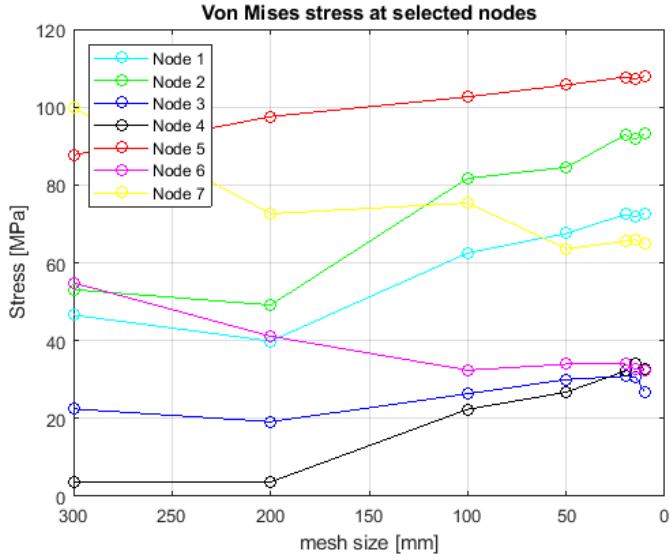


(b) Von Mises stresses at a selection of nodes for different mesh sizes.

Figure A.15: Convergence of results for the second geometry under bergy bit B14 loading.

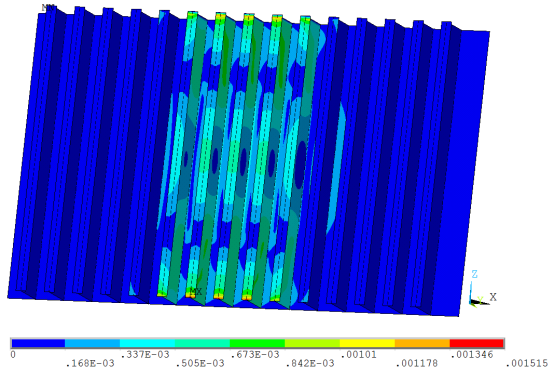


(a) Von Mises total mechanical strain.

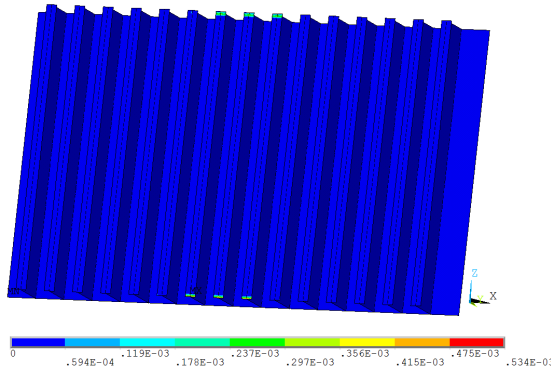


(b) Von Mises plastic strain.

Figure A.16: Von Mises strain. Bergy bit B14 loading applied to the second geometry with a mesh size of 15 mm.

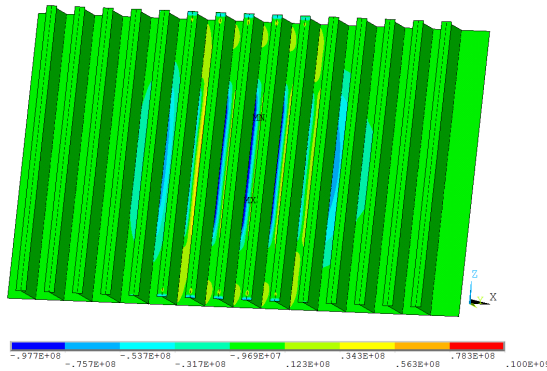


(a) Normal stress in x-direction.

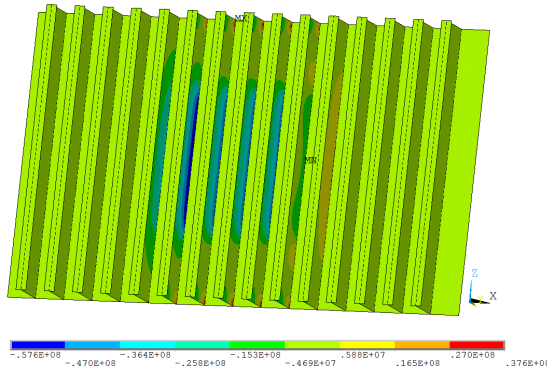


(b) Normal stress in y-direction.

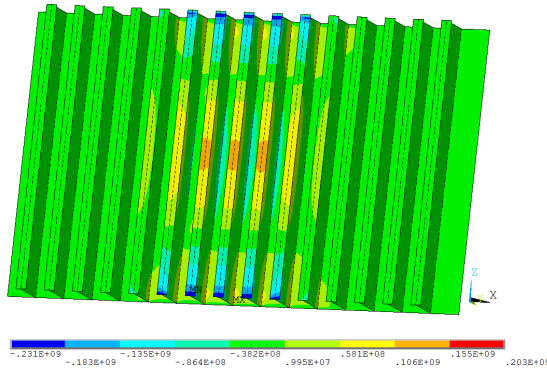


(c) Normal stress in z-direction.

Figure A.17: Normal stresses. Bergy bit B14 loading applied to the second geometry with a mesh size of 15 mm.

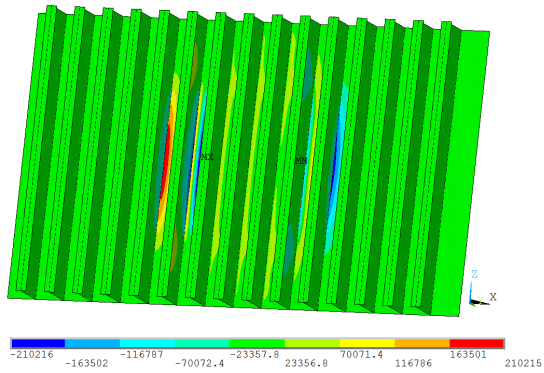


(a) Shear stress in plane normal to x-axis, y-direction. $\sigma_{XY}$.

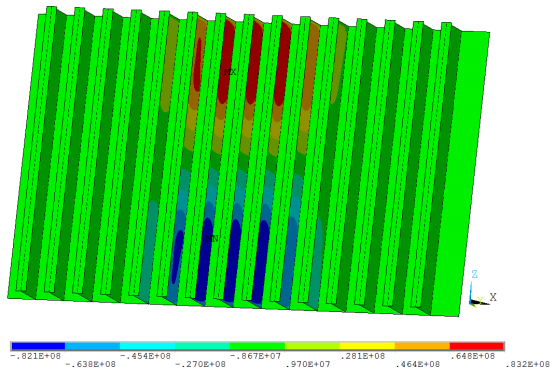


(b) Shear stress in plane normal to y-axis, z-direction. $\sigma_{YZ}$.

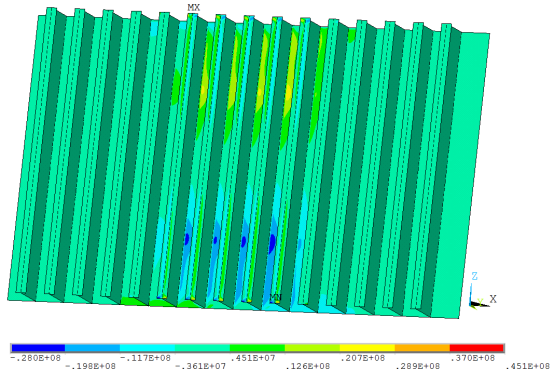


(c) Shear stress in plane normal to x-axis, z-direction. $\sigma_{XZ}$.

Figure A.18: Shear stresses. Bergy bit B14 loading applied to the second geometry with a mesh size of 15 mm.

## A.5 Bergy bit B09 Loading - First Geometry

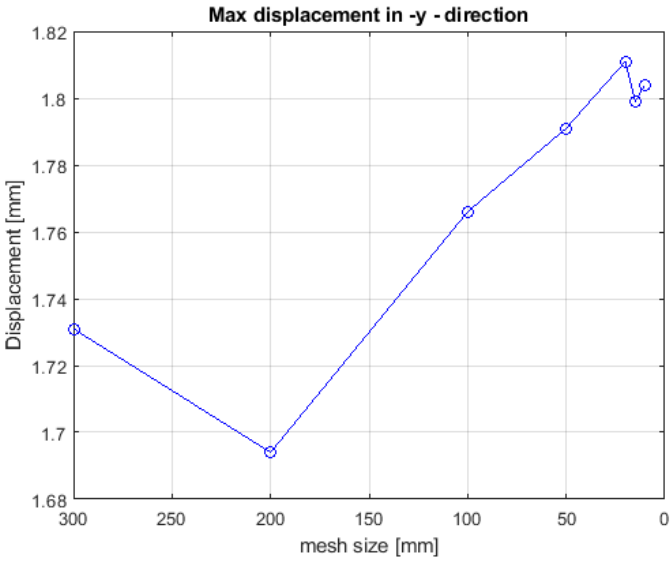


(a) Maximum displacement for different mesh sizes.

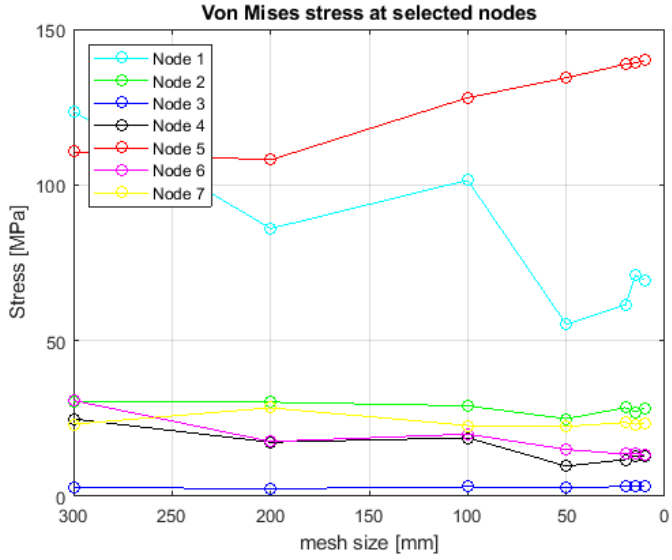


(b) Von Mises stresses at a selection of nodes for different mesh sizes.

Figure A.19: Convergence of results for the first geometry under bergy bit B09 loading.

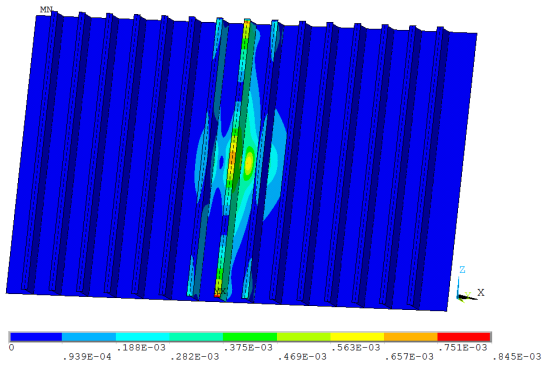


(a) Von Mises total mechanical strain.

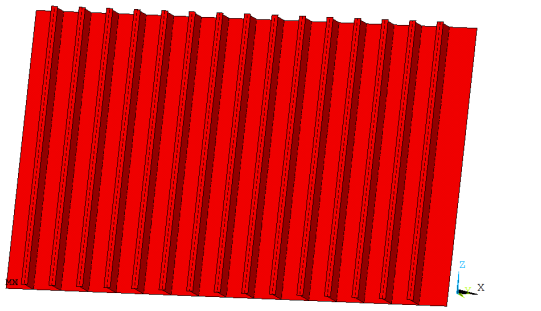


(b) Von Mises plastic strain is zero.

Figure A.20: Von Mises strain. Bergy bit B09 loading applied to the first geometry with a mesh size of 15 mm.

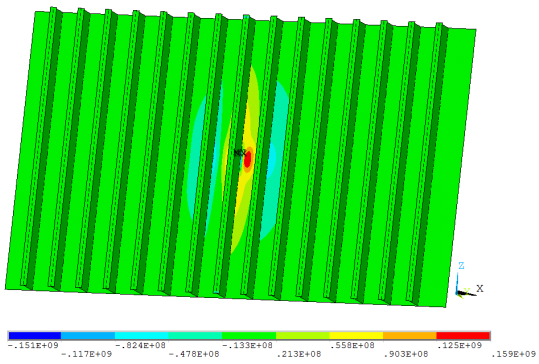


(a) Normal stress in x-direction.

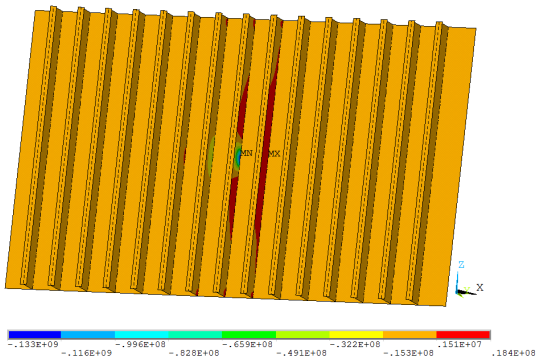


(b) Normal stress in y-direction.

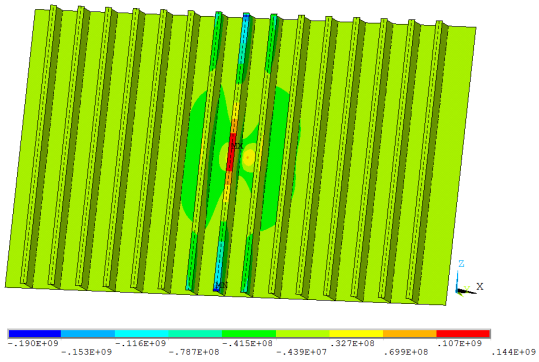


(c) Normal stress in z-direction.

Figure A.21: Normal stresses. Bergy bit B09 loading applied to the first geometry with a mesh size of 15 mm.

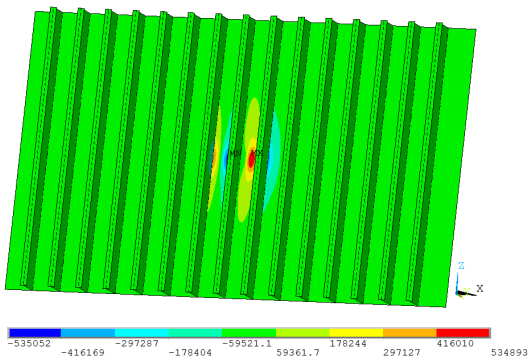


(a) Shear stress in plane normal to x-axis, y-direction. $\sigma_{XY}$.

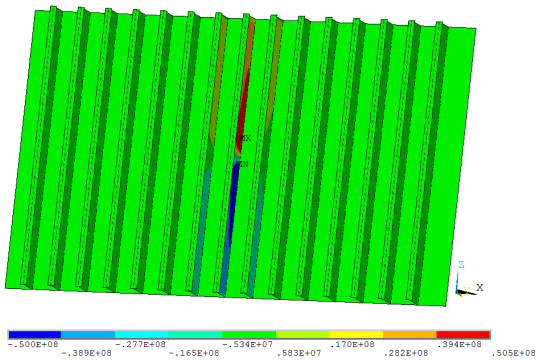


(b) Shear stress in plane normal to y-axis, z-direction. $\sigma_{YZ}$.

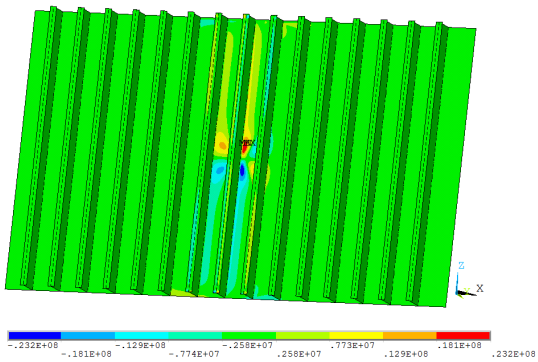


(c) Shear stress in plane normal to x-axis, z-direction. $\sigma_{XZ}$.

Figure A.22: Shear stresses. Bergy bit B09 loading applied to the first geometry with a mesh size of 15 mm.

## A.6 Bergy bit B09 Loading - Second Geometry

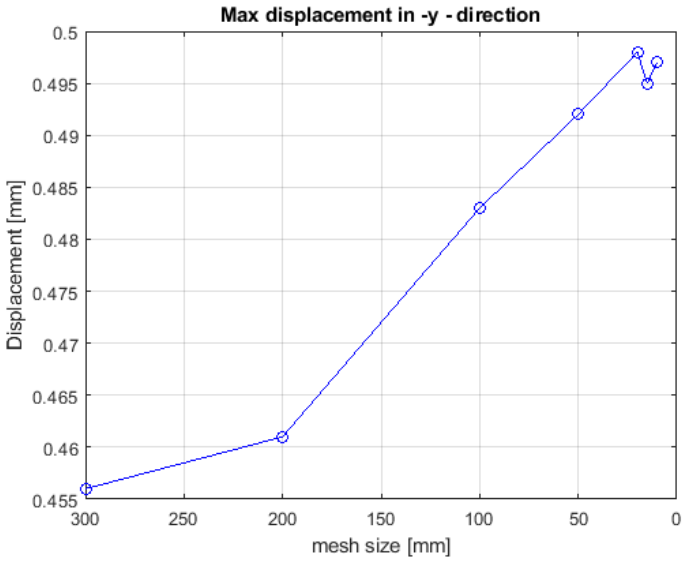


(a) Maximum displacement for different mesh sizes.

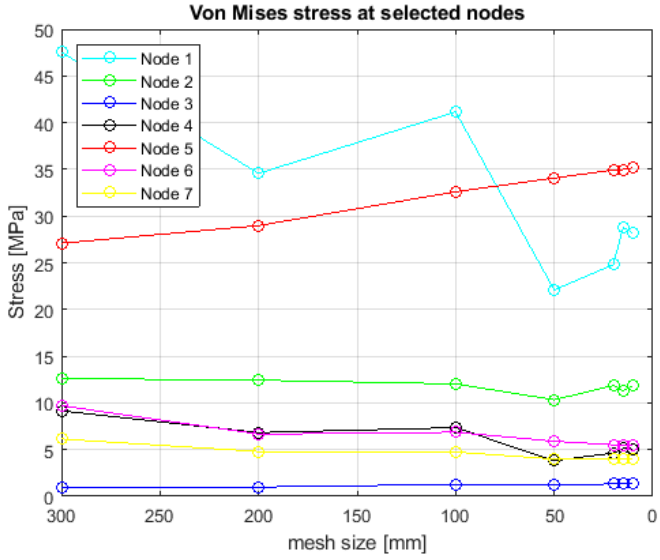


(b) Von Mises stresses at a selection of nodes for different mesh sizes.

Figure A.23: Convergence of results for the second geometry under bergy bit B09 loading.

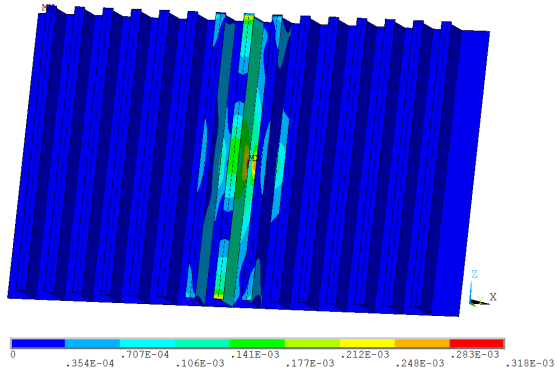


(a) Von Mises total mechanical strain.

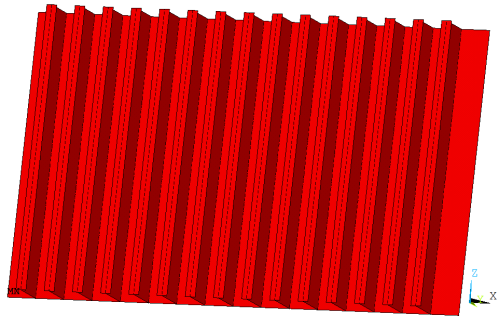


(b) Von Mises plastic strain is zero.

Figure A.24: Von Mises strain. Bergy bit B09 loading applied to the second geometry with a mesh size of 15 mm.

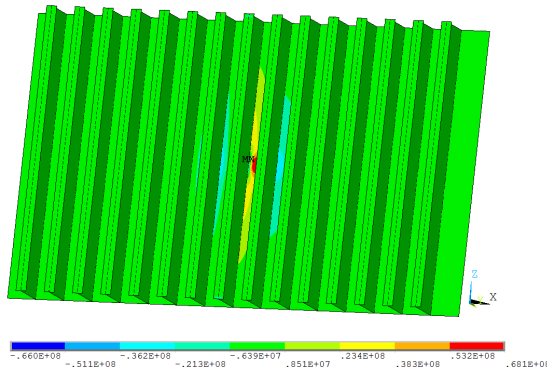


(a) Normal stress in x-direction.

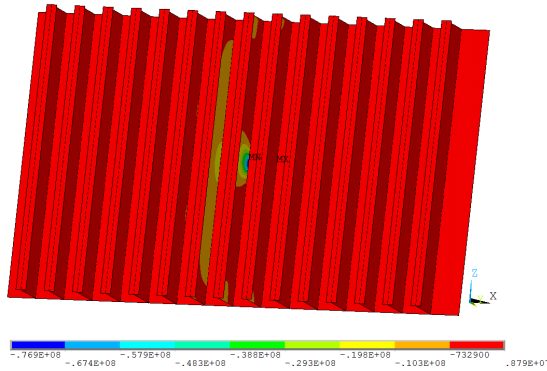


(b) Normal stress in y-direction.

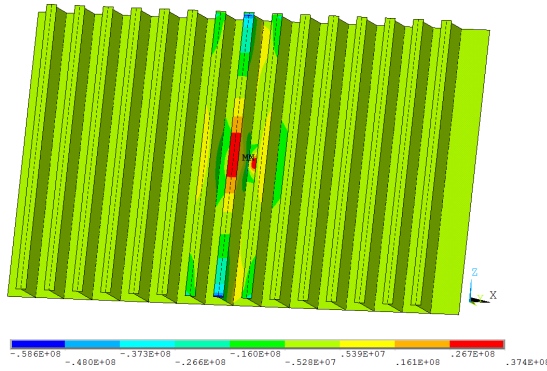


(c) Normal stress in z-direction.

Figure A.25: Normal stresses. Bergy bit B09 loading applied to the second geometry with a mesh size of 15 mm.

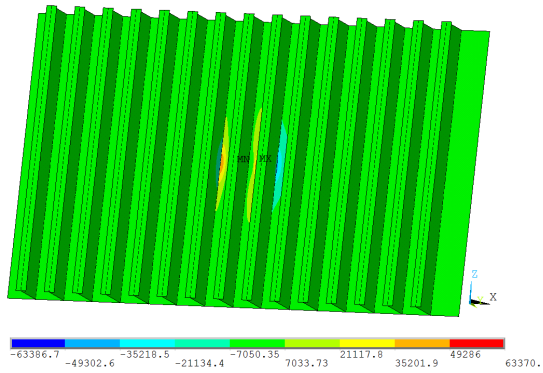


(a) Shear stress in plane normal to x-axis, y-direction. $\sigma_{XY}$.

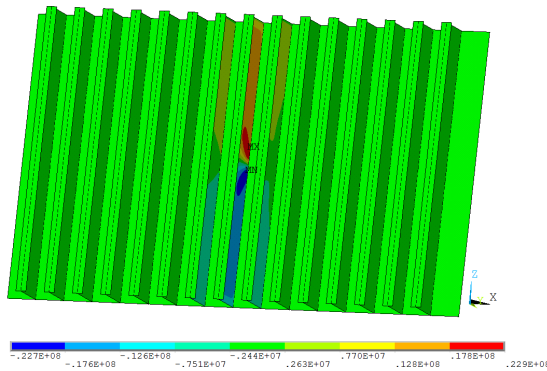


(b) Shear stress in plane normal to y-axis, z-direction. $\sigma_{YZ}$.

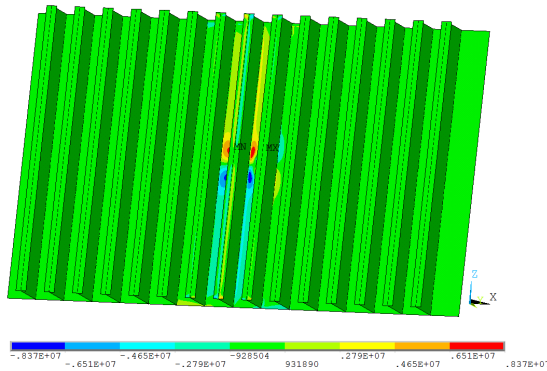


(c) Shear stress in plane normal to x-axis, z-direction. $\sigma_{XZ}$.

Figure A.26: Shear stresses. Bergy bit B09 loading applied to the second geometry with a mesh size of 15 mm.

# Appendix B

# Additional Results - Dynamic Loading

## B.1 Second Geometry

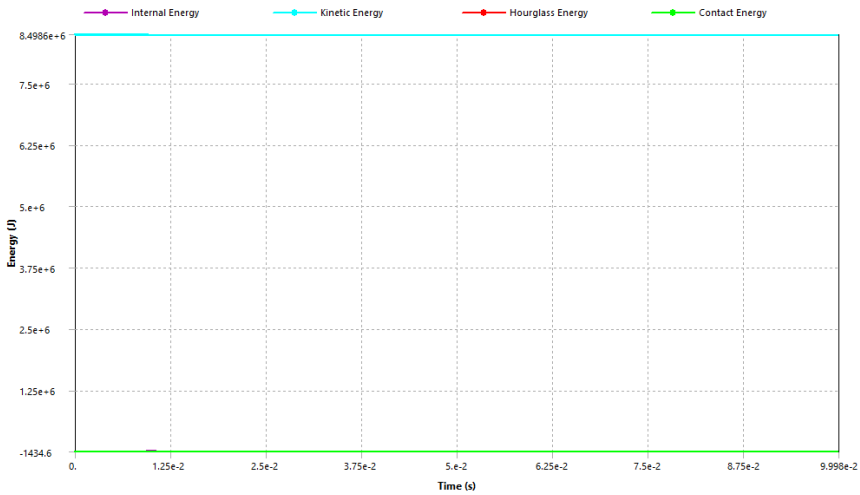


Figure B.1: Energy summary of the simulation.

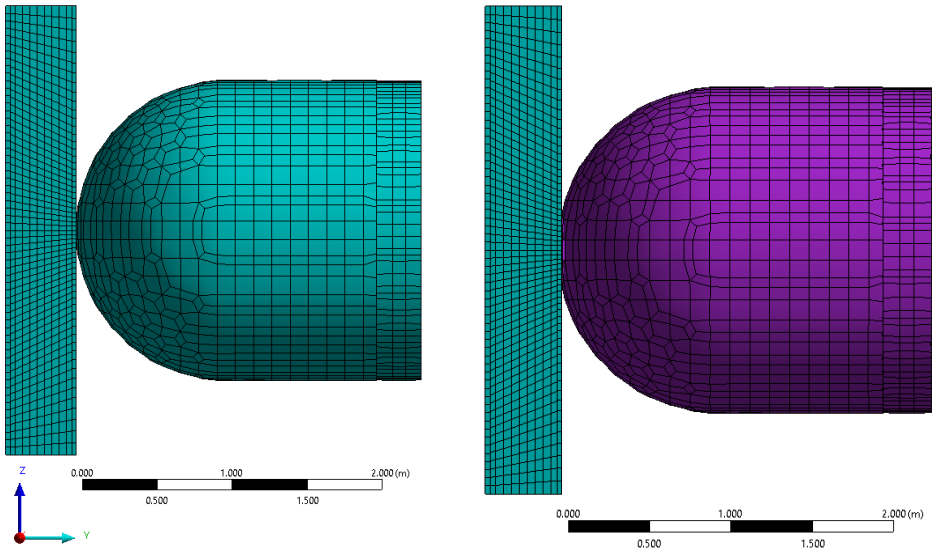


(a) Time=0 s. (b) Time=1.00e-2 s.

Figure B.2: Side view of impact analysis.

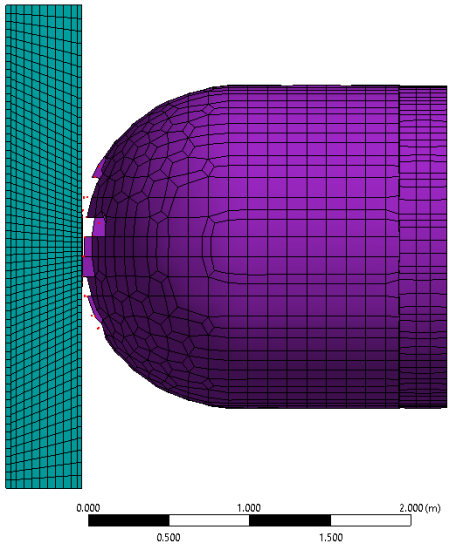


(c) Time=1.25e-2 s.

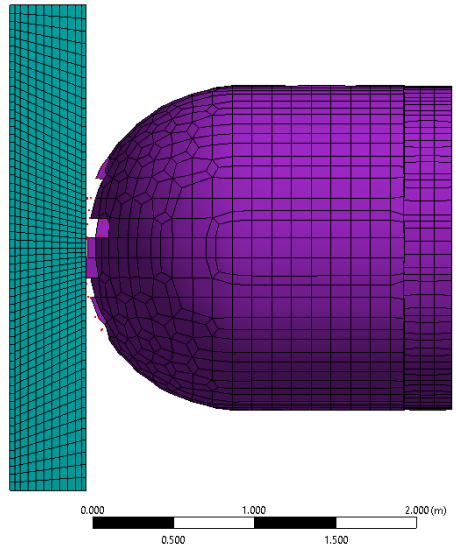


(d) Time=1.50e-2 s.

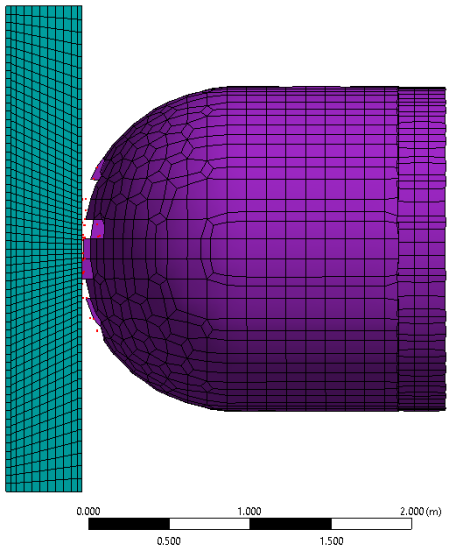


(e) Time=1.75e-2 s.

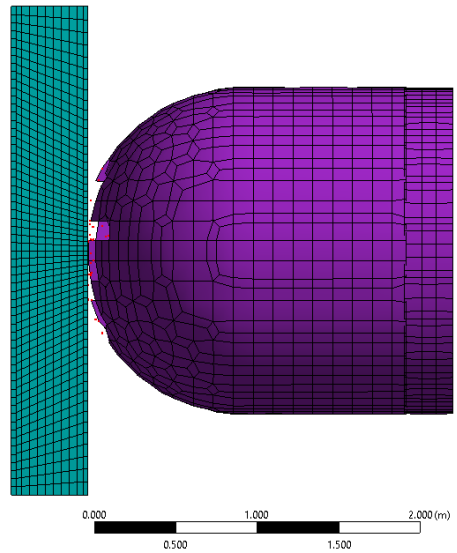


(f) Time=2.00e-2 s.

Figure B.2: Side view of impact analysis (cont.).

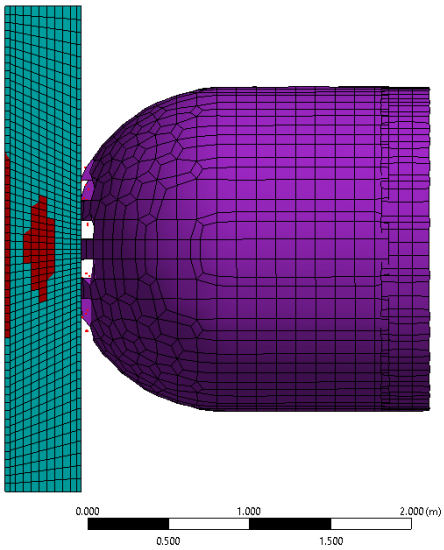


(g) Time=5.00e-2 s.

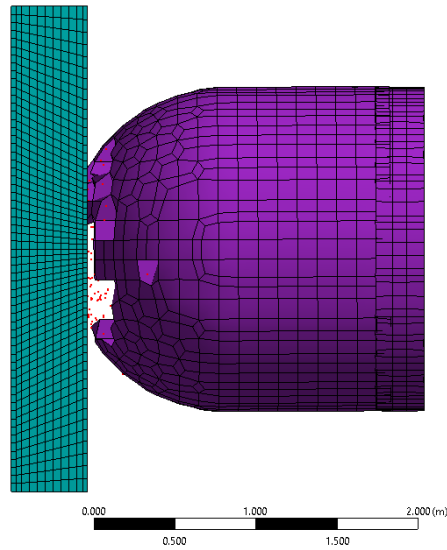


(h) Time=7.50e-2 s.

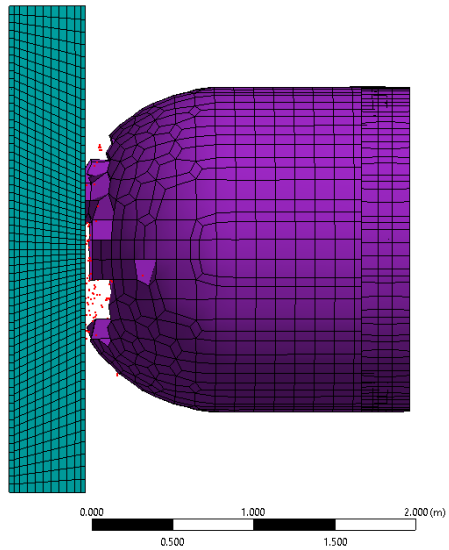


(i) Time=10.00e-2 s.

Figure B.2: Side view of impact analysis (cont.).

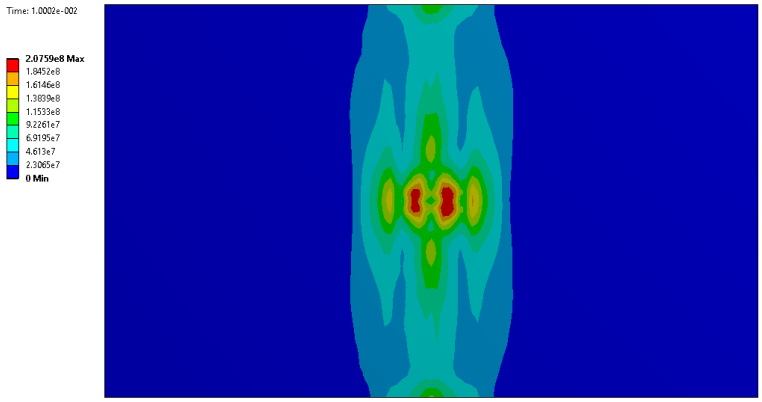


Figure B.3: Von Mises stress for plate at time of maximum value. Time=1.0002e-2 s.

The changing von Mises stress is shown below.

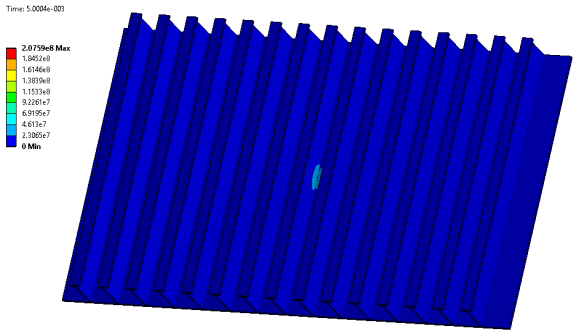


(a) Time=0.50e-2 s.

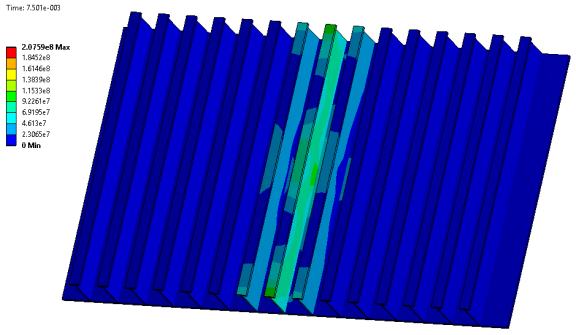


(b) Time=0.75e-2 s.

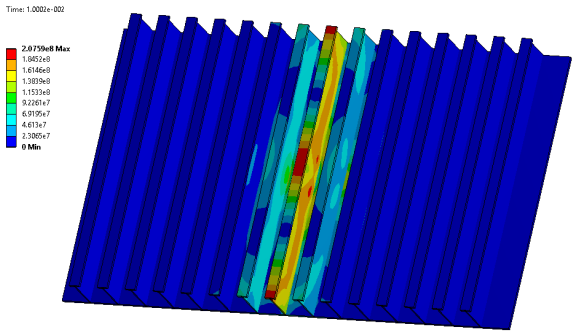


(c) Time=1.00e-2 s.

Figure B.4: Von Mises stress over time from 0.50e-2 s to 2.00e-2 s. Stress in Pa.

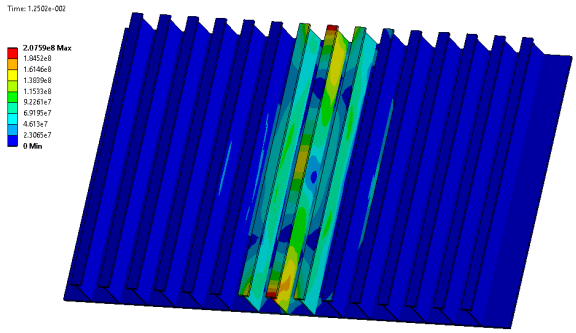


(d) Time=1.25e-2 s.

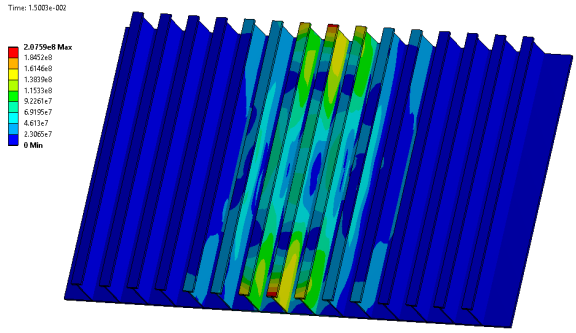


(e) Time=1.50e-2 s.

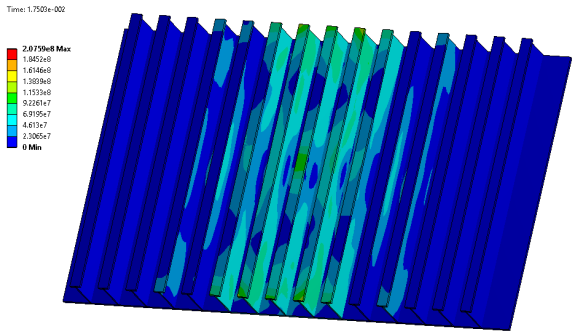


(f) Time=1.75e-2 s.

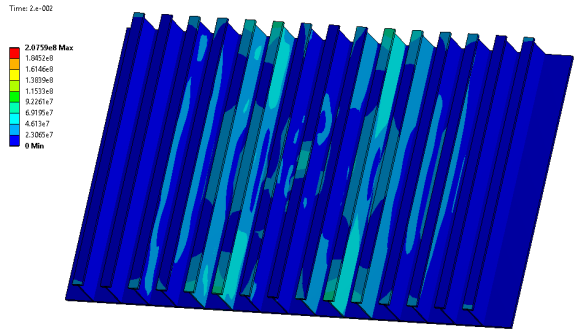


(g) Time=2.00e-2 s.



Figure B.4: Von Mises stress over time from 0.50e-2 s to 2.00e-2 s. Stress in Pa. (cont.)